Quantum metrology with trapped ions

by

Joseph D. Broz

A dissertation submitted in partial satisfaction of the

requirements for the degree of

Doctor of Philosophy

in

Physics

in the

Graduate Division

of the

University of California, Berkeley

Committee in charge:

Professor Hartmut Häffner, Chair
Professor Dan Stamper-Kurn
Professor Eli Yablonovitch

Fall 2023

Quantum metrology with trapped ions

Abstract

Quantum metrology with trapped ions

by

Joseph D. Broz

Doctor of Philosophy in Physics

University of California, Berkeley

Professor Hartmut Häffner, Chair

We present the results of an experiment that used the quantized motion of an ion trapped in a harmonic pseudopotential to test for nonlinear extensions of quantum mechanics. This test was motivated by the development of a recent, consistent theory of nonlinear quantum mechanics that, in contrast to previous frameworks, also preserves causality. This experiment represents the first test of this new theory in a fully quantum system and improved the bounds on potential nonlinear effects in quantum mechanics inferred from previous experimental results by about seven orders of magnitude.

We also present the results of an experiment that used two entangled ions to test for local violations of Lorentz invariance and which tightened the bound on such hypothetical violations by about half of an order of magnitude. In particular, this experiment used a special entangled state of the ions, residing within a decoherence free subspace, which is immune to the dominant source of noise. By comparing our results against a similar experiment, performed with two non-entangled ions, we verify the expected factor-of-two improvement in the signal-to-noise ratio predicted by theory. This improvement can be directly attributed to the use of entanglement and, thus, this work provides a case study of how entanglement can be leveraged as a resource to fundamentally enhance the performance of spectroscopic measurements.

To my mother, sisters, Lia and Chesty. Good night Chesty, wherever you are.

Acknowledgments

First, and foremost, I must acknowledge my graduate research advisor and principal investigator Hartmut Häffner. Hartmut is wise but patient, knowledgeable but humble and, without his guidance and unwavering support, this thesis would not have been possible. I must similarly acknowledge Mark Schlossman, my undergraduate research advisor at the University of Illinois Chicago. Professor Schlossman provided me with my first real research experience in experimental physics, which served to motivate and guide the direction that I would ultimately pursue in graduate school. He was also a fantastic mentor and teacher.

In terms of the skills required to actually "do" good experimental physics, I learned most of what I know through the example set by the outstanding post-doctoral researchers and senior graduate students that I had the privilege of working with over the years. In particular, Eli Megidish introduced me to the group, taught me how to lock my first laser, how to couple light into my first fiber, how to entangle my first qubits, and has just generally been a great mentor and friend. Clemens Matthiesen and Sara Mouradian were also indispensable resources whenever I had a tough question or needed a helping hand and, as a senior graduate student, Dylan Gorman set a high bar that I reflected upon often.

I owe the pleasantness of my day-to-day experience at Berkeley to the fantastic environment in Hartmut's lab – a credit to the many wonderful people whom I had the privilege of sharing lab space with including Wei-Ting, Sumanta, Bingran, Maya, Crystal, Erhan, Elia, Justin, Ryan, Nicole, Da, Neil, Boerge, Erik and many more. And the friends that I made in the larger UC Berkeley physics department including Juan Camilo, Dylan, Sam and Shawn.

Every academic opportunity that I have had was made possible by the United States Marine Corps and the financial support I received through the GI Bill and Illinois Veteran Grant. My time in the Marines was tough, but it also instilled in me the self-discipline and self-belief that was necessary to attempt and achieve everything that I have in my higher education. I cannot thank enough the many exemplary leaders and peers that I served my country alongside including Marc Harrison, Brett Maddix, Paul Zogg, Daniel Pavela, Lupe Guerrero, Eric Esparza, Steve Davis, Sean Padfield, Justin Humpich, Joshua Kalina, Matthew McCormack, Jeffrey Ahlborn, Chris Crowe and Chris Bay – to name just a few.

Finally, I would like to acknowledge the generous support I received from the National Science Foundation Graduate Research Fellowship Program (NSF-GRFP), which funded the first three years of my research in Hartmut's laboratory. And I would also like to acknowledge the bottomless support from my mother, my sisters and my faithful dog Lia who is up there somewhere on the other end of the rainbow bridge.

Contents

List of Figures

List of Tables

Chapter 1

Introduction

1.1 Motivation

Systems of ions trapped using oscillating electric fields have proven over time to be one of the most well-controlled, accessible and pristine test beds of quantum mechanics available for experiment. Using well-focused laser beams, pairs of electronic states in individual ions can be resonantly selected and precisely manipulated. Effective interactions between the electronic states of multiple ions can be mediated via the Coulomb repulsion inherently present when simultaneously trapping multiple ions in the same harmonic confining potential. This effective interaction can be leveraged to engineer complex many-body entangled states between the internal electronic states of the ions. In addition, the strongly coupled motion of the ions itself represents a controllable quantum resource, particularly when combined with laser cooling capable of lowering the temperature of even large chains of ions near to its quantum ground state.

These features have allowed trapped ion systems to develop into one of the leading technological platforms pushing the bounds of the so-called *second quantum revolution* [25]. In the first quantum revolution, the theory of quantum mechanics was laid out, convincingly verified by experiment and used to explain macroscopically observed phenomena that could otherwise not be explained by classical theory. In contrast, the second quantum revolution involves engineering well-controlled quantum systems to perform tasks in a way that is fundamentally superior to what can be achieved by classical devices. Such tasks fall under the broad moniker of quantum information processing and includes digital quantum computation, analog quantum simulation and quantum metrology.

In this thesis, we will describe two quantum metrological experiments performed with singly-ionized atoms of ^{40}Ca. In the first, we test the superposition principle of quantum mechanics itself, by building an interferometer out of the two branches of a superposition of the ground and first excited vibrational states of a single ^{40}Ca ion. According to a recent theory of nonlinear quantum mechanics [52], such a state is expected to experience a relative energy shift that depends on the population weightings of these two branches. This theory is

fully causal, in contrast to previous efforts and, ultimately for this reason, its effects turn out to be rather difficult to observe with standard atomic or nuclear spectroscopy. In the second experiment, we explicitly make use of entanglement as a resource by engineering a special entangled state of the internal electronic degrees of freedom of two ions that is first-order insensitive to the dominant noise source. We then use this state to experimentally determine, what was at the time, the most stringent bound on violations of Lorentz invariance for the dispersion relation of the electron.

1.2 Structure

This document is organized as follows. In Chapter 2 we provide a basic overview of the most important physical concepts underlying the design of the experiments performed in this thesis. This is followed, in Chapter 3 with a summary of the basic set of the procedures and techniques common to these experiments. Then in Chapter 4, we describe the actual physical apparatus within which these experiments were performed. Finally, in Chapters 5 and 5, we describe the two experiments comprising the main work of this thesis. In particular, Chapter 5 covers our search for causal nonlinear corrections to quantum mechanics and Chapter 6 covers our search for violations of Lorentz invariance.

Chapter 2

Theoretical framework

2.1 Introduction

This chapter is intended to provide a general, but basic, overview of the physical concepts that underlie the trapped ion experiments described in Chapters 5 and 6. In Section 2.2 we describe how a combination of AC and DC electric fields can be used to confine ionized atoms in a small region of space and the classical and quantum properties of the structures that a collection of ions will form when cooled to near to their ground state of motion. In Section 2.3 we describe the electronic structure of the singly-ionized ^{40}Ca atoms that we utilize in experiments. In Section 2.4 we describe how this internal structure may be experimentally tuned via the application of an external, static magnetic field. And, finally, in Section 2.6 we describe the dynamical response of an ion's internal and external degrees of freedom to a well-focused and coherent laser beam.

2.2 Trapping ions

Ponderomotive forces and the pseudopotential approximation

The most fundamental reason for ionizing the atoms in our experiments is to leverage the strong Coulomb force in order to stably pin them down in place. But this ends up being a nontrivial task due to the fact that it is not possible to confine charged particles in free space using only static electric fields. This is known as Earnshaw's theorem [40] and is a direct consequence of Gauss's law, which requires that the instantaneous electric flux (and, thus, force) through any closed surface in free space be zero (see Figure 2.1).

However, if an electric field is allowed to oscillate rapidly in time, then Earnshaw's theorem no longer applies. In this case, an effective, time-averaged force can be generated that always drives a charged particle towards regions where the *magnitude* of the (unmodulated) electric field is weaker [34]. One can then use, for example, an oscillating electric quadrupole potential to stably trap an ion, which we will discuss in the next section [77, 23].

But first, we describe the nature of this time-averaged force, known as a *ponderomotive* force. We start by considering an electric field of the form:

$$\mathbf{E}(\mathbf{r}, t) = \mathbf{E}_0(\mathbf{r})\cos(\Omega t) \tag{2.1}$$

The motion of a particle of mass m and charge q placed in this field is described by:

$$m\ddot{\mathbf{r}} = q\mathbf{E}_0(\mathbf{r})\cos(\Omega t) \tag{2.2}$$

Clearly, the field will cause the particle to oscillate at a frequency of Ω. But, if $\mathbf{E}_0(\mathbf{r})$ is nonuniform, its mean position will also drift on a slower time scale since the net force

$$\oint \mathbf{E} \cdot d\mathbf{A} \neq 0$$
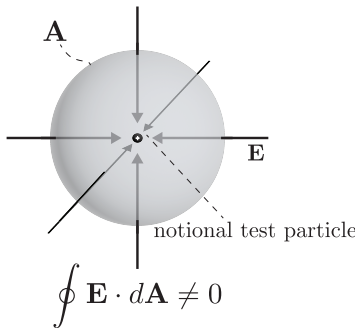
Figure 2.1: Illustration of Earnshaw's theorem. The arrows represent electric flux lines oriented in such a way as to provide a restoring force to a positively charged test particle when perturbed in any direction. But this configuration necessarily violates Gauss's law, since it implies a net electric flux into the sphere.

accumulated over each period of its oscillation will generally be nonzero (see Figure 2.2). This motivates us to explicitly separate the trajectory of the particle into two components:

$$\mathbf{r} = \mathbf{r}_M + \mathbf{r}_\mu \tag{2.3}$$

where $\mathbf{r}_\mu$ describes the fast oscillations and $\mathbf{r}_M$ describes the slower accumulated drift. We can then Taylor expand the field in Equation 2.2 about $\mathbf{r}_M$:

$$m(\ddot{\mathbf{r}}_M + \ddot{\mathbf{r}}_\mu) = q[\mathbf{E}_0(\mathbf{r}_M) + \nabla\mathbf{E}_0(\mathbf{r}_M)\mathbf{r}_\mu + \ldots]\cos(\Omega t) \tag{2.4}$$

Now, because the particle has finite inertia, it is always possible to choose a sufficiently large Ω such that the following conditions hold:

$$|\mathbf{E}_0(\mathbf{r}_M)| \gg |\nabla\mathbf{E}_0(\mathbf{r}_M)\mathbf{r}_\mu| \tag{2.5}$$

$$|\ddot{\mathbf{r}}_\mu| \gg |\ddot{\mathbf{r}}_M| \tag{2.6}$$

where both comparisons are meant to be interpreted element-wise[1] and the first condition simply implies that the particle does not have a chance, during a single period of its oscillation, to substantially probe the curvature of the field. In the following we will also assume that the drift velocity satisfies the condition $|\dot{\mathbf{r}}_M| \ll |\mathbf{r}_\mu\Omega|$ such that $\mathbf{r}_M$ does not change appreciably during a period of oscillation. However, this is not strictly necessary so long as Equation 2.6 is satisfied [23].

Under these assumptions, the expansion in Equation 2.4 can be truncated after zeroth order and a solution for $\mathbf{r}_\mu$ can be easily found[2]:

$$m\ddot{\mathbf{r}}_\mu \approx q\mathbf{E}_0(\mathbf{r}_M)\cos(\Omega t)$$

$$\implies \mathbf{r}_\mu(t) \approx -\frac{q\mathbf{E}_0(\mathbf{r}_M)}{m\Omega^2}\cos(\Omega t) \tag{2.7}$$

And by substituting this into Equation 2.4 and averaging the whole expression over a single modulation period, we can also find an approximate solution for $\mathbf{r}_M$:

$$\langle m\ddot{\mathbf{r}}_M + m\ddot{\mathbf{r}}_\mu\rangle \approx \left\langle q\mathbf{E}_0(\mathbf{r}_M)\cos(\Omega t) + q\nabla\mathbf{E}_0(\mathbf{r}_M)\mathbf{r}_\mu\cos(\Omega t)\right\rangle$$

$$\implies m\ddot{\mathbf{r}}_M \approx -\frac{q^2}{m\Omega^2}\nabla\mathbf{E}_0(\mathbf{r}_M)\mathbf{E}_0(\mathbf{r}_M)\langle\cos^2(\Omega t)\rangle$$

$$= -\frac{q^2}{2m\Omega^2}\nabla\mathbf{E}_0(\mathbf{r}_M)\mathbf{E}_0(\mathbf{r}_M) \tag{2.8}$$

---

[1] For example, Equation 2.5 should be written: $|[\mathbf{E}_0(\mathbf{r}_M)]_i| \gg |[\nabla\mathbf{E}_0(\mathbf{r}_M)\mathbf{r}_\mu]_i|$, $\forall i$

[2] When integrating to get Equation 2.7, we assume that $\mathbf{r}_\mu(0) = \dot{\mathbf{r}}_\mu(0) = 0$ since any initial non zero position or velocity is incorporated into $\mathbf{r}_M$
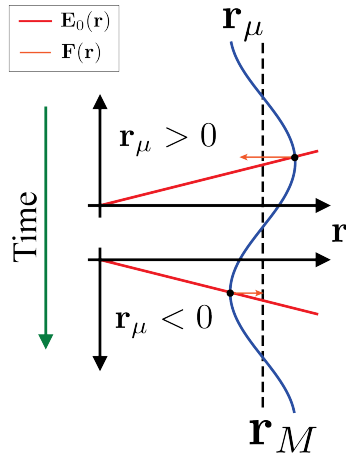
Figure 2.2: Illustration of a Ponderomotive force. The top is a snapshot of the particle's position when $\mathbf{r} > \mathbf{r}_M$. The bottom is a similar snapshot when $\mathbf{r} < \mathbf{r}_M$. In both cases the force acts in a direction so as to restore $\mathbf{r}$ to $\mathbf{r}_M$ but, because the electric field $\mathbf{E}_0(r)$ has a finite gradient, the magnitude of the force is greater in the former case than in the latter. When averaged over a full period of modulation, the net force is known as a ponderomotive force.

where crossed out terms have a time-averaged value of zero.

The last line of Equation 2.8 is the ponderomotive force that we alluded to earlier. We can rewrite it in terms of a notional potential $\psi(\mathbf{r}_M)$, known as a *psuedopotential*:

$$m\ddot{\mathbf{r}}_M = -\nabla\psi(\mathbf{r}_M), \qquad \psi(\mathbf{r}_M) = \frac{q^2 E_0^2(\mathbf{r}_M)}{4m\Omega^2} \tag{2.9}$$

which makes it obvious that the ponderomotive force always acts to drive the particle towards a region where the magnitude of the electric field is weaker[3].

In summary, if a charged particle is driven by an alternating electric field, then it will oscillate. If these oscillations are fast enough, then the particle will not have a chance to probe the curvature of the field throughout a single period of its motion. Because of the particle's inertia, its oscillations will be mostly out of phase with the driving field, such that the effect of the field on these time scales is always to return the particle to nearly the same position. But, if the field has a finite gradient, then during the half-period of oscillation when the position of the particle is greater than its approximate mean, the force it experiences will be greater than during the other half-period when its position is less than its approximate mean. The net force experienced by the particle averaged over a full period of oscillation is known as a ponderomotive force. This is illustrated in Figure 2.2.

---

[3]Independent even of the sign of q.

Paul trap
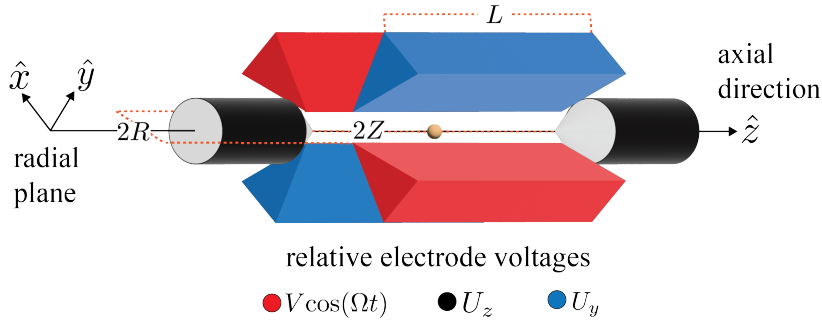
Figure 2.3: Paul trap. Ions are trapped using a combination of RF and DC potentials applied to the red/blue blade electrodes and black endcaps.

In practice, the electrode configuration used to trap ions is similar in design to the one shown in Figure 2.3. Trapping in the radial plane is achieved by driving the red, or "blade" electrodes, with an oscillating, radiofrequency (RF) potential $V_{\mathrm{RF}}\cos(\Omega t)$ and, optionally, by driving the blue electrodes with a static or DC potential U_y. Trapping in the axial direction is achieved by driving the black electrodes, or "endcaps," with a DC potential U_z. The whole assembly is known as a "Paul trap" after its inventor Wolfgang Paul [77].

We first consider trapping in the radial direction when $U_r = 0$. If the length L of the blade electrodes is large relative to their separation R, then the potential for points near the center (yellow sphere in Figure 2.3) has the form of an oscillating, two-dimensional electric quadrupole[4]:

$$\Phi_{\mathrm{RF}}(\mathbf{r}, t) = \frac{V_{\mathrm{RF}}/2}{\tilde{R}^2}(x^2 - y^2)\cos(\Omega t) \tag{2.10}$$

which generates the electric field:

$$\mathbf{E}(\mathbf{r}, t) = -\nabla\Phi_{\mathrm{RF}}(\mathbf{r}, t) = -\frac{V_{\mathrm{RF}}}{\tilde{R}^2}(x\hat{\mathbf{x}} - y\hat{\mathbf{y}})\cos(\Omega t) \tag{2.11}$$

According to Equation 2.9, the ion will then experience the pseudopotential:

$$\psi(\mathbf{r}) = \frac{1}{2}m\omega_r^2(x^2 + y^2), \qquad \omega_r = \frac{qV_{\mathrm{RF}}}{\sqrt{2}m\tilde{R}^2\Omega} \tag{2.12}$$

which has the form of a harmonic confining potential with a radial trapping frequency ω_r. This is illustrated in Figure 2.4.

---

[4]$\tilde{R} \sim R$. The tilde denotes the possibility that R be scaled by some geometric factor, which can be determined empirically [60].

From Equations 2.5-2.6 and our explicit expression for $\mathbf{E}(\mathbf{r}, t)$, we can check under what conditions the pseudopotential approximation is valid. In both cases, we find that we require:

$$\frac{\omega_r}{\Omega} = \frac{qV}{\sqrt{2}m\Omega\tilde{R}^2} \ll 1 \tag{2.13}$$

From Equation 2.7, we can also find the first-order correction to the pseudopotential approximation for the ion's trajectory:

$$r_i(t) = A_i\cos(\omega_r t + \phi_i)\left[1 + \sqrt{2}\left(\frac{\omega_r}{\Omega}\right)\cos(\Omega t)\right] \tag{2.14}$$

where $r_i \in \{x, y\}$ and A_i, ϕ_i are determined by initial conditions. In this context, the fast oscillating term in Equation 2.14 is known as *micromotion*.

All of this implies that there is a trade-off between choosing a larger Ω to improve the pseudopotential approximation (and reduce the micromotion) and choosing a smaller Ω to increase the radial trapping frequency (which requires some micromotion to generate the ponderomotive force in the first place). In our lab, we have a rule of thumb that ω_r should be at least an order of magnitude smaller than Ω. Otherwise, it is possible to have a situation where the field is still confining, but the breakdown of the approximation is enough to cause practical problems. The orders of magnitude for our typical choices of trapping parameters are given in Table 2.1.

It is possible to confine ions in all three dimensions using only RF fields [77]. But for our purposes, it is more convenient to achieve confinement along the z-direction with DC fields. Ideally, this is done by applying an equal voltage U_z to both endcaps. Keeping only terms up to second order, the resulting potential[5] is given approximately by:

$$\Phi_{\text{endcaps}}(\mathbf{r}) = \frac{U_z}{\tilde{Z}^2}[z^2 - \frac{1}{2}(x^2 + y^2)] \tag{2.15}$$

Summing this with ψ, the full potential is then:

$$\Phi(\mathbf{r}) = \frac{1}{2}m[\omega_r'^2(x^2 + y^2) + \omega_z^2 z^2] \tag{2.16}$$

$$\omega_r'^2 = \omega_r^2 - \frac{1}{2}\omega_z^2, \qquad \omega_z^2 = \frac{2U_z}{m\tilde{Z}^2} \tag{2.17}$$

So that stable confinement is possible as long as $\omega_r^2 > \omega_z^2/2$.

Typically, a nonzero voltage U_y is also applied to break the degeneracy of the trapping frequencies in the radial plane and allow for full control over the anisotropy of the harmonic confining potential. The most general form of the Paul trap potential is then:

$$\Phi(\mathbf{r}) = \frac{1}{2}m(\omega_x^2 x^2 + \omega_y^2 y^2 + \omega_z^2 z^2) \tag{2.18}$$

---

[5]Again $\tilde{Z} \sim Z$. See footnote 3.
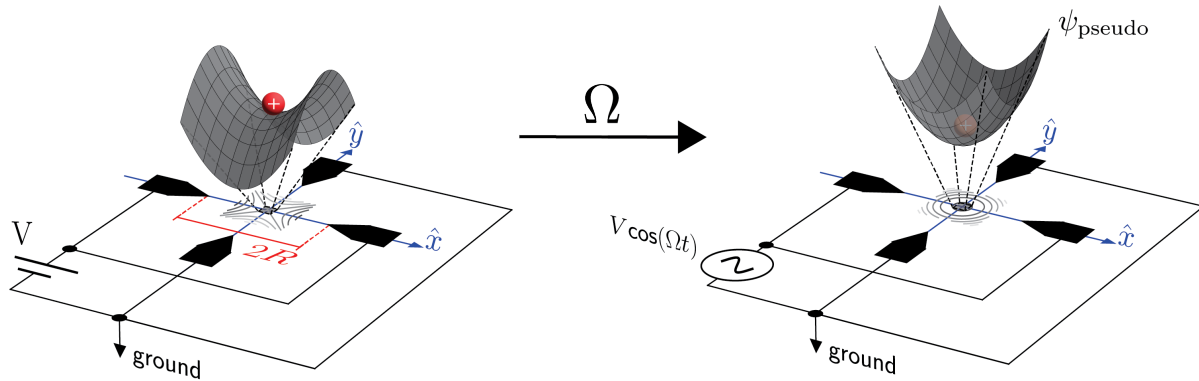
Figure 2.4: The two-dimensional pseudopotential used to confine ions in the radial plane. On the left is pictured the unmodulated potential, which has the form of a quadrupole. On the right is pictured the time-averaged effect of the same potential but now modulated at an RF frequency of Ω. In both cases, what is shown is a slice through the radial plane of the full three-dimensional potential which extends a relatively large distance $L/2$ in both directions of the (orthogonal) z-axis. Figure adapted from [81].

where:

$$\omega_x = \sqrt{\frac{q^2 V_{\mathrm{RF}^2}}{2m^2 \tilde{R}^4 \Omega^2} - \frac{U_z}{m\tilde{Z}^2} - \frac{U_y}{m\tilde{R}^2}} \tag{2.19}$$

$$\omega_y = \sqrt{\frac{q^2 V_{\mathrm{RF}^2}}{2m^2 \tilde{R}^4 \Omega^2} + \frac{2U_y}{m\tilde{Z}^2} - \frac{U_z}{m\tilde{Z}^2}} \tag{2.20}$$

$$\omega_z = \sqrt{\frac{2U_z}{m\tilde{Z}^2} - \frac{U_y}{m\tilde{R}^2}} \tag{2.21}$$

Physical Parameter	Typical Value (order of magnitude)
ω_r	$2\pi\times$ 3 MHz
ω_z	$2\pi\times$ 1 MHz
Ω	$2\pi\times$ 30 MHz
V	1 kV
R	1 mm
Z	3 mm
M	10^{-22} g
trap depth [17]	1 eV, corresponding to a temperature of $\sim 10^4$ K

Table 2.1: Typical ion trapping parameters. V, R and Z can vary depending on the specific design of the trapping electrodes.

Excess micromotion

Usually, it is safe to interpret the pseudopotential in Equation 2.18 quite literally, and for the remainder of this thesis unless otherwise specified we will. However, micromotion can cause several deleterious effects, and there are certain cases where it cannot be ignored. These effects are amplified if, in addition to the intrinsic micromotion required for the ponderomotive force, an extraneous or *excess* micromotion is present in the system. There can be multiple reasons for this:

- geometric trap imperfections (e.g. misalignment of the radial and axial potential null points),

- a small phase difference between the RF electrodes,

- spurious RF pickup[6] (e.g. on the axial electrodes),

- stray electric fields.

As described in [7], these effects can be incorporated by modifying the description of the ion's trajectory in Equation 2.14:

$$r_i(t) \approx (r_i' + A_i\cos)(\omega_i t + \phi_i)[1 - \sqrt{2}(\omega_r/\Omega)\cos(\Omega t)] + \beta\sin(\Omega t) \tag{2.22}$$

where r_i' describes a displacement of the ion's equilibrium position due to a stray electric field E_i:

$$r_i' \approx \frac{QE_i}{m\omega_i^2} \tag{2.23}$$

---

[6]Present when, for example, there is a phase difference between the RF electrodes.
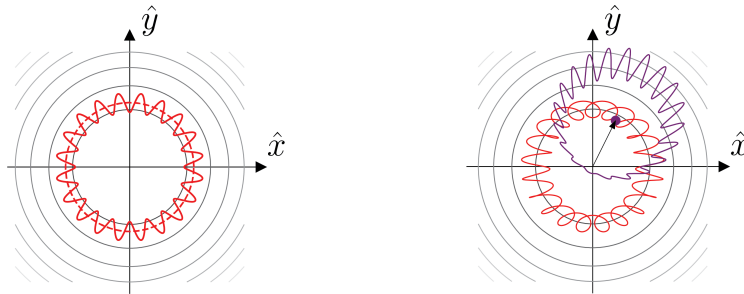
Figure 2.5: Micromotion. **Left**: The dashed line represents the trajectory of the ion under the pseudopotential approximation. In reality, some finite micromotion is necessary to generate the ponderomotive force. The solid line represents the ion's trajectory when including this intrinsic micromotion to first-order. **Right**: The purple curve illustrates the effect of a mean displacement of the ion's position from the null point of the pseudopotential due to a stray electric field. The red curve illustrates the effect of a phase imbalance between a pair of RF electrodes. In both cases, the magnitude of the micromotion is increased. This is termed "excess" micromotion.

and β is proportional to the phase difference between electrodes. An illustration of these effects is shown in Figure 2.22.

For the experimental apparatus used in this thesis, stray electric fields were the dominant source of excess micromotion. Such fields can be caused by laser-induced charging of dielectrics near the trap (for example, the mounting structure for the trap electrodes or even thin oxide layers formed on the electrodes themselves) and may change over time. Our actual trapping apparatus includes in-situ *compensation* electrodes for balancing out the effect of any stray electric fields (see Chapter 4) such that the trapping point (at least for a single ion) is at the true null of the quadrupole potentials (radial and axial). The procedure for doing this is described in detail in [82, 39].

Trapping multiple ions

When there are multiple ions present in a trap, we must also take into account their mutual Coulomb interaction. If the kinetic energy of the ions is large, then the resulting dynamics will generally be complicated and chaotic [73]. But with laser cooling, the kinetic energy can be reduced to within a fraction of its quantum zero-point value. In this case, the ions will *crystallize* close to an equilibrium configuration where each ion positions itself such that the harmonic confining force it experiences is exactly balanced by the inter-ionic Coulomb repulsion. Since stable trapping requires that the confining strength be set weaker in the axial direction than in the radial directions, the structure of this crystal will be that

of a linear chain oriented along the axial direction[7]. Residual motion is then well-described by small excursions away from this equilibrium where, to good approximation, the Coulomb repulsion can be linearized.

In Appendix A, we describe how to find the equilibrium positions and motional structure for chains containing an arbitrary number of ions (including cases where the mass and charge of the ions are nonuniform). However, we rarely worked with chains of more than two ions for the experiments covered in this thesis, so here we will provide a simpler, intuitive analysis considering only this case.

The equilibrium separation between two ions along the axial direction can be found by setting the inter-ion Coulomb repulsion equal to the confining force generated by the Paul trap:

$$m\omega_z^2 \frac{Z}{2} = \frac{e^2}{kZ^2} \implies Z = \left(\frac{2e^2}{km\omega_z^2} \right)^{1/3} \sim 10 \ \mu\text{m for } \omega_z \sim 2\pi \times \ 1 \text{ MHz} \qquad (2.24)$$

where $k = 4\pi\varepsilon_0$. Now, we consider small, axial excursions away from equilibrium, characterized by the quantities δz_1 and δz_2 where we assume $\delta z_1, \delta z_2 \ll Z$ (see Figure 2.6). We are looking for the first-order, linear response to these perturbations, so we Taylor expand the Coulomb repulsion:
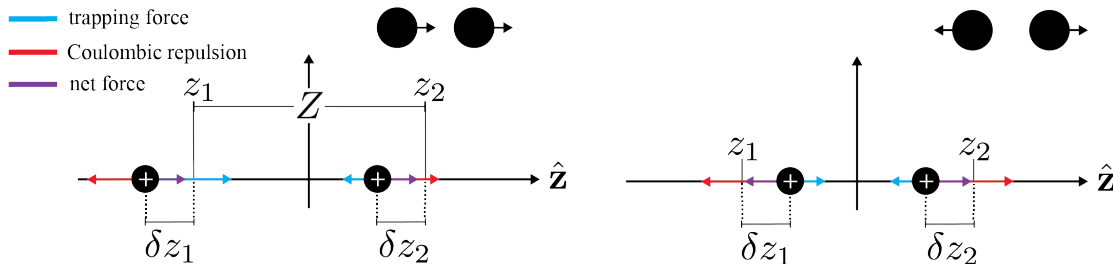
Figure 2.6: Axial normal modes. **Left**: Correlated, center of mass motion. **Right**: Anti-correlated, stretch motion. z_1, z_2 are the equilibrium positions of the ions and Z is their equilibrium separation. δz_1, δz_2 are small displacements away from equilibrium along the axial ($\hat{\mathbf{z}}$) direction.

---

[7]Even inside the parameter space of three-dimensional confinement, there still exists a finite ratio $\omega_{\text{radial}}/\omega_{\text{axial}} \approx 0.77N/\sqrt{\log N}$ below which the linearity of the ions will break and the chain will begin to develop *kinks* [28].

$$F_{C,\hat{z}}^{(2)} = \frac{e^2}{k[Z + (\delta z_2 - \delta z_1)]^2} \approx \frac{e^2}{kZ^2}\left[1 - 2\frac{\delta z_2 - \delta z_1}{Z}\right]$$

$$= m\omega_z^2\frac{Z}{2} - m\omega_z^2(\delta z_2 - \delta z_1) \tag{2.25}$$

where $F_{C,\hat{z}}^{(2)}$ denotes the Coulomb force, in the z-direction, felt by the second ion due to the first ion and $F_{C,\hat{z}}^{(1)} = -F_{C,\hat{z}}^{(2)}$. Including the trapping force, the full equations of motion are then:

$$m\ddot{\delta z_1} = m\omega_z^2\frac{Z}{2} - m\omega_z^2\delta z_1 - m\omega_z^2\frac{Z}{2} + m\omega_z^2(\delta z_2 - \delta z_1) \tag{2.26}$$

$$m\ddot{\delta z_2} = -m\omega_z^2\frac{Z}{2} + m\omega_z^2\delta z_2 + m\omega_z^2\frac{Z}{2} - m\omega_z^2(\delta z_2 - \delta z_1) \tag{2.27}$$

If we define the two new coordinates $\delta z_{\text{com}} = \delta z_2 + \delta z_1$ and $\delta z_{\text{stretch}} = \delta z_2 - \delta z_1$, we can add/substract Equations 2.26, 2.27 to find:

$$m\ddot{\delta z}_{\text{com}} = -m\omega_z^2\delta z_{\text{com}} \tag{2.28}$$

$$m\ddot{\delta z}_{\text{stretch}} = -m3\omega_z^2\delta z_{\text{stretch}} \tag{2.29}$$

The center of mass coordinate δz_{com} describes the correlated vibrational motion of the ions and the stretch coordinate $\delta z_{\text{stretch}}$ describes the anti-correlated vibrational motion. Any allowed state of motion can be written as some superposition of these coordinates. The center of mass vibrational frequency, $\omega_{z,\text{com}} = \omega_z$, is the same as the single-ion vibrational frequency. On the other hand, the frequency of the stretch mode is larger: $\omega_{z,\text{stretch}} = \sqrt{3}\omega_z$.

The same procedure can be repeated for displacements in the radial directions. To be specific, we will consider the x-direction, but the following holds for the y-direction as well. First, we linearize the Coulomb repulsion:

$$|\mathbf{F}_C| = \frac{e^2}{k[Z^2 + (\delta x_2 - \delta x_1)^2]} \approx \frac{e^2}{kZ^2}\left[1 - \left(\frac{\delta x_2 - \delta x_1}{Z}\right)^2\right] \approx m\omega_z^2\frac{Z}{2} \tag{2.30}$$

In this case, the force in the z-direction is also affected (see Figure 2.7) but, to first-order in δx_1, δx_2, the change is negligible:

$$F_{C,\hat{z}}^{(2)} = |\mathbf{F}_C|\cos(\theta) = |\mathbf{F}_C|\frac{Z}{\sqrt{Z^2 + (\delta x_2 - \delta x_1)^2}} \approx |\mathbf{F}_C| \tag{2.31}$$

$$F_{C,\hat{x}}^{(2)} = |\mathbf{F}_C|\sin(\theta) = |\mathbf{F}_C|\frac{\delta x_2 - \delta x_1}{\sqrt{Z^2 + (\delta x_2 - \delta x_1)^2}} \approx |\mathbf{F}_C|\frac{\delta x_2 - \delta x_1}{Z} \tag{2.32}$$
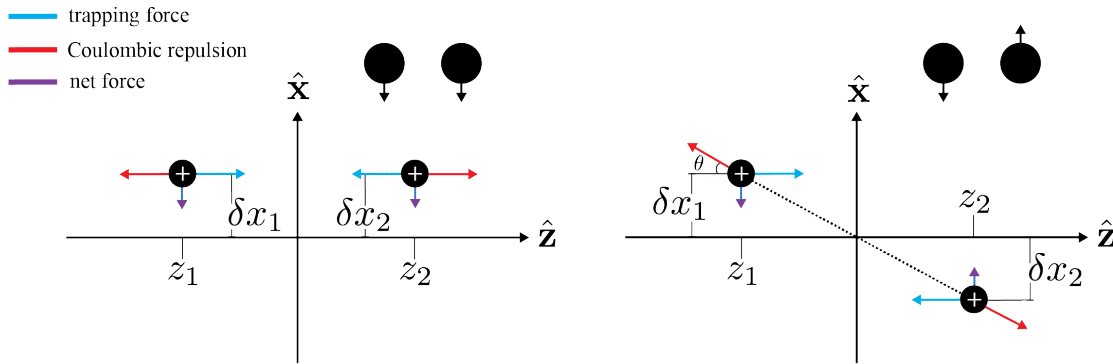
Figure 2.7: Radial normal modes. **Left**: Correlated, center of mass motion. **Right**: Anti-correlated, rocking motion. The rocking motion also affects the force in the z-direction but, to first-order in δx_1, δx_2, this is negligible.

where $F_{C,\hat{x}}^{(1)} = -F_{C,\hat{x}}^{(2)}$. Including the trapping force, the equations of motion are:

$$m\ddot{\delta x}_1 = -m\omega_x^2 \delta x_1 + \frac{1}{2}m\omega_z^2(\delta x_2 - \delta x_1) \tag{2.33}$$

$$m\ddot{\delta x}_2 = -m\omega_x^2 \delta x_2 - \frac{1}{2}m\omega_z^2(\delta x_2 - \delta x_1) \tag{2.34}$$

And we can define the new coordinates $\delta x_{\text{com}} = \delta x_2 + \delta x_1$, $\delta x_{\text{rocking}} = \delta x_2 - \delta x_1$ such that:

$$m\ddot{\delta x}_{\text{com}} = -m\omega_x^2 \delta x_{\text{com}} \tag{2.35}$$

$$m\ddot{\delta x}_{\text{rocking}} = -m(\omega_x^2 - \omega_z^2)\delta z_{\text{rocking}} \tag{2.36}$$

Once again, the radial center of mass vibrational frequency is equal to the single-ion vibrational frequency. $\omega_{x,\text{com}} = \omega_z$. However, as opposed to the axial stretch mode, the vibrational frequency of the radial rocking mode is smaller than for the center of mass mode: $\omega_{x,\text{rocking}} = \sqrt{\omega_x^2 - \omega_z^2}$.

Several observations can be generalized to larger ion chains:

- For homogeneous chains, there will always be a unique center of mass mode.

We can construct a center of mass mode equation for an N-ion chain the same way as we did for two, by summing the equivalent of Equations 2.26-2.27 and 2.33-2.34. By symmetry, the Coulomb repulsion terms on the right-hand side will cancel out and on the left-hand side we will have $\sum_i^N m\ddot{\delta\alpha}_i = m\ddot{\delta\alpha}_{\text{com}}$ where $\alpha \in \{x, y, z\}$. However, this only works if all of the masses are equal otherwise there will not generally be a unique center of mass mode.

- The center of mass mode is the lowest frequency made in the axial direction, but the largest frequency mode in the axial direction.

The reason for this is that any anti-correlated motion in the axial direction requires the ions to come closer to each other than their equilibrium separation and this requires more energy. On the other hand, anti-correlated motion in the radial directions only results in the ions being further apart from each other.

- The splitting of the mode frequencies in the radial directions is much smaller than in the axial direction.

This can be understood by noting that a slight change to the position of one ion in the axial directions causes a change in the separation distance of:

$$\frac{Z + \delta z}{Z} = 1 + \frac{\delta z}{Z}$$

whereas the same perturbation in the radial direction only changes the separation distance by:

$$\frac{\sqrt{Z^2 + \delta x^2}}{Z} \sim 1 + \frac{1}{2}\left(\frac{\delta x}{Z}\right)^2 \tag{2.37}$$

which is much smaller.

- The lowest-order correction to Equation 2.31 results in a coupling between the radial rocking mode and the axial stretch mode.

This can be resonantly enhanced if the two modes are similar in frequency [84] and we have measured this effect experimentally.

Quantum treatment of trapped ion motion

So far our description of ion trapping has been entirely classical. But with laser cooling, we often work in a regime where the thermal energy of the ions is comparable to their quantum ground state energy. This means that a full, quantum description of the motion is necessary. On the other hand, it turns out that treating the confining potential as classical remains completely sufficient. So we can carry forward all of our previous results and quantize the ionic motion in an ad hoc manner by constructing the appropriate classical Hamiltonian and applying the canonical quantization to the motional degrees of freedom. Then one will find that the Hamiltonian for a linear chain of ions is described by a collection of quantum harmonic oscillators [51, 47]:,

$$\hat{H} = \sum_{\alpha \in (x,y,z)} \sum_{l=1}^{N} \hbar \nu_{\alpha,l}(\hat{a}_{\alpha,l}^\dagger \hat{a}_{\alpha,l} + 1/2) \tag{2.38}$$

where each l is associated with a normal mode solution to Equation A.14 and $\hat{a}^\dagger_{\alpha,l}$, $\hat{a}_{\alpha,l}$ are annihilation and creation operators satisfying the normal commutation relation:

$$[\hat{a}_{\alpha,l}, \hat{a}^\dagger_{\alpha,k},] = \delta_{lk} \qquad (2.39)$$

In this basis, the motion of the ith ion relative to its equilibrium position along the α spatial axis is described by the quantum position and momentum operators:

$$\hat{x}_{\alpha,i} = \sum_{l=1}^{N} \beta^{(\alpha)}_{i,l} \sqrt{\frac{\hbar}{2m_i\nu_{\alpha,l}}}(\hat{a}^\dagger_{\alpha,l} + \hat{a}_{\alpha,l}) \qquad (2.40)$$

$$\hat{p}_{\alpha,i} = i\sum_{l=1}^{N} \beta^{(\alpha)}_{i,l} \sqrt{\frac{\hbar m_i\nu_{\alpha,l}}{2}}(\hat{a}^\dagger_{\alpha,l} - \hat{a}_{\alpha,l}) \qquad (2.41)$$

such that $[\hat{x}_{\alpha,i}, \hat{p}_{\alpha,j}] = i\hbar\delta_{ij}$. Here $\boldsymbol{\beta}^{(\alpha)}_l$ is a normalized vector describing the participation of the ions in the lth mode (see Appendix A). In general, scales with the number of ions as $\beta^{(\alpha)}_{i,l} \sim 1/\sqrt{N}$, where this relationship holds exactly for the center of mass modes. The characteristic spread of the position-space wavefunction for the ion in the lth mode is:

$$\sqrt{\langle n|\hat{x}^2_{\alpha,i}|n\rangle} = |\beta^{(\alpha)}_{i,l}|\sqrt{2n+1}\sqrt{\frac{\hbar}{2m_i\nu_{\alpha,l}}} \qquad (2.42)$$

where $|n\rangle$ refers to the nth Fock state. For a single ion of calcium, this amounts to about 10 nm in the ground state. This justifies our linearization of the Coulomb force in the preceding section for typical experimental conditions, where the mean Fock state occupancy $\langle n\rangle$ is rarely more than 10 (and usually much smaller).

Note: these results assume that the pseudopotential approximation in Equation 2.18 holds exactly. It is possible to perform a similar quantization of the motion while explicitly taking into account the time modulation [58] of the trapping potentials. The main takeaway is that the pseudopotential still remains a good approximation even in the quantum case. The dominant correction manifests when an ion is addressed by laser light. In this case, in the ion's frame of reference, it appears as though the light is modulated at the frequency of its micromotion.

2.3   Electronic structure of $^{40}\text{Ca}^+$
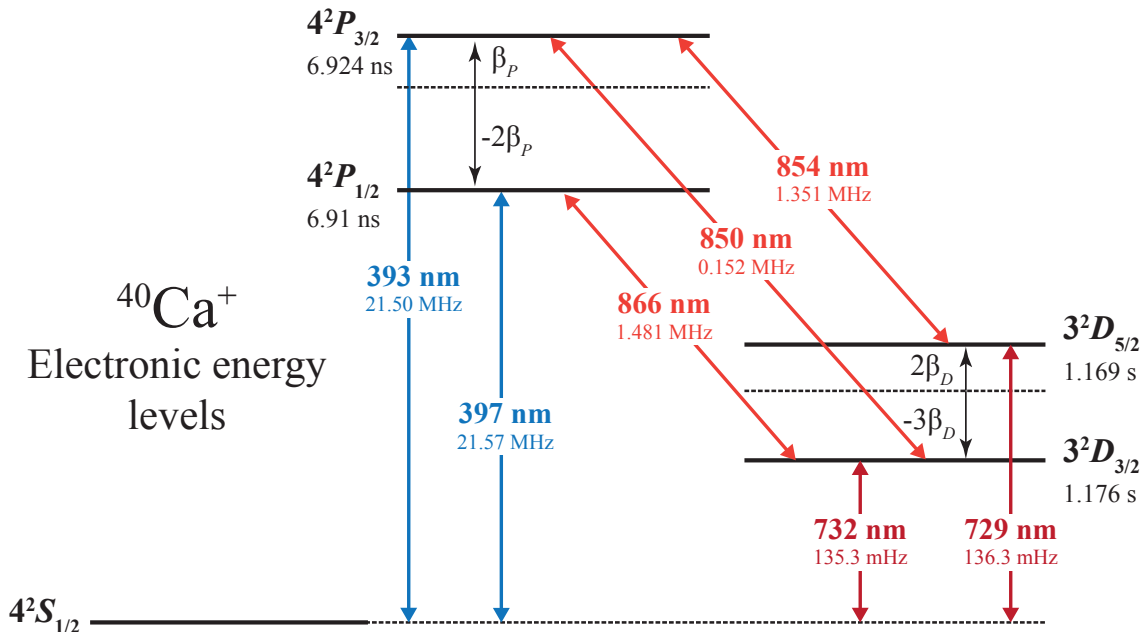
Figure 2.8: Low lying excited state structure of $^{40}\text{Ca}^+$. Lengths denote transition wavelengths and frequencies denote the corresponding linewidths. Times characterize the typical duration that an excited state will be occupied before it spontaneously decays to a lower-energy state via the emission of a photon. The βs denote the spin-orbit splitting of the E_{nl} energy levels into fine structure doublets characterized by a particular value of j. These are labelled according to the standard spectroscopic notation (Equation 2.52) Each fine structure level has a $2j + 1$ degeneracy corresponding to the eigenstates of $\hat{J}_z$.

Central field approximation

The experiments in this thesis were performed using singly-ionized atoms of $^{40}\text{Ca}^+$, which has a ground state configuration of $[\text{Ar}]4s^1$. Ions (or atoms) with configurations such as this, containing only a single electron in the valence shell, are said to be *hydrogen-like* since they can be pictured as a single, weakly-bound valence electron orbiting a much more strongly bound, positively-charged and spherically-symmetric[8], inner argon core. The low-lying excited state structure is almost entirely dictated by the coordinates of the valence

---

[8]Since the total orbital angular momentum of any closed electronic subshell in an isolated atom must be zero, the charge distribution of the argon core must be spherically symmetric.

electron, while the wavefunction for the core electrons remains essentially constant. Thus, we can provide a reasonable description of the excited state structure with the following *central, single-particle* Hamiltonian, which only tracks the coordinates of the valence electron [53]:

$$\hat{H}_{\mathrm{CF}} = \frac{\hat{p}^2}{2m_e} + U_{\mathrm{CF}}(\hat{r}) \tag{2.43}$$

Here, m_e is the valence electron's mass[9], $\hat{p}$ is its momentum, $\hat{r}$ is its separation from the nucleus and U_{CF} is its potential energy, which results from the combination of its interaction with the nuclear charge and with the mean field of the inner core.

Coarse structure

Just as with hydrogen, the spherical symmetry of $\hat{H}_{\mathrm{CF}}$ implies that states with well-defined energy also have a well-defined angular momentum $\hat{\mathbf{L}} = \hat{\mathbf{r}} \times m_e \hat{\mathbf{v}}$. That is:

$$\hat{H}_{\mathrm{CF}}\psi_{nlm_l}(\hat{\mathbf{r}}) = E_{nl}\psi_{nlm_l}(\hat{\mathbf{r}}) \tag{2.44}$$

$$\hat{L}^2\psi_{nlm_l}(\hat{\mathbf{r}}) = \hbar^2 l(l+1)\psi_{nlm_l}(\hat{\mathbf{r}}) \tag{2.45}$$

$$\hat{L}_z\psi_{nlm_l}(\hat{\mathbf{r}}) = \hbar m_l\psi_{nlm_l}(\hat{\mathbf{r}}) \tag{2.46}$$

where the wavefunction can be separated into radial and angular components:

$$\psi_{nlm_l}(\hat{\mathbf{r}}) = R_{nl}(\hat{r})Y_{lm_l}(\hat{\theta}, \hat{\phi}) \tag{2.47}$$

with Y_{lm_l} the normal angular momentum eigenstates (spherical harmonics).

The radial wavefunction R_{nl} determines the separation between the valence electron and the nucleus and groups its stationary states into distinct shells, characterized by the quantum number n, and consisting of states with different angular momenta but a similar mean nuclear separation. The precise value of the mean nuclear separation depends on l due to a centrifugal term in $\hat{H}_{\mathrm{CF}}$ [41]. Intuitively, states with higher orbital angular momentum are less likely to be found nearer to the nucleus.

The same is true for hydrogen. However, $\hat{H}_{\mathrm{CF}}$ does not have the "accidental" degeneracy present in the (nonrelativistic) hydrogen Hamiltonian, where $E_{nl} = E_n$ [31]. The presence of the inner electrons acts to shield the valence electron from experiencing the full nuclear charge but states with smaller l, that spend more time closer to the nucleus, experience less shielding and, thus, a stronger attraction to the nucleus. This effect is enough to shift the energy of the $|n = 4, l = 0, m_l\rangle$ states of $^{40}\mathrm{Ca}^+$ below the energy of the $|n = 3, l = 2, m_l\rangle$ states and largely defines the ion's coarse electronic structure. The splitting between the lowest excited states is on the order of tens of electronvolts (as shown in Figure 2.8), leading to transition energies in the visible spectrum, which is typical for singly-ionized alkaline earth metals.

---

[9]Or, better, the reduced mass of the valence electron and nucleus.

In order to fully describe a stationary state of the ion, we must also specify the orientation of the valence electron's intrinsic spin. This is defined relative to its observed magnetic dipole moment $\hat{\boldsymbol{\mu}}_S$:

$$\hat{\boldsymbol{\mu}}_S = -g_s\mu_B\frac{\hat{\mathbf{S}}}{\hbar} \tag{2.48}$$

where $g_e \approx 2$ is the electron g-factor and $\mu_B = e\hbar/2m_e$ is the Bohr magneton. $\hat{\mathbf{S}}$ obeys an analogous set of relationships to $\hat{\mathbf{L}}$:

$$\hat{S}^2\psi_{nlm_l}(\hat{\mathbf{r}})|s,m_s\rangle = \hbar^2 s(s+1)\psi_{nlm_l}(\hat{\mathbf{r}})|s,m_s\rangle \tag{2.49}$$

$$\hat{S}_z\psi_{nlm_l}(\hat{\mathbf{r}})|s,m_s\rangle = \hbar m_s\psi_{nlm_l}(\hat{\mathbf{r}})|s,m_s\rangle \tag{2.50}$$

except in this case we always have $s = 1/2$, which restricts $m_s = \pm 1/2$.

The set of operators $\{\hat{H}_{\mathrm{CF}}, \hat{L}^2, \hat{L}_z, \hat{S}^2, \hat{S}_z\}$ constitute a complete set of commuting observables (CSCO) [22] and the corresponding quantum numbers are sufficient to fully specify an arbitrary stationary state of $^{40}\mathrm{Ca}^+$ as:

$$|n,l,m_l,s,m_s\rangle = \int d^3\mathbf{r}\,\psi_{nlm_l}(\mathbf{r})|\mathbf{r}\rangle|s,m_s\rangle \tag{2.51}$$

But note that there is a high degree of degeneracy since states which share the same n and l but different m_l and m_s have the same energy under $\hat{H}_{\mathrm{CF}}$. According to the rules of angular momentum in quantum mechanics, for a given value of l, m_l is allowed to be any of $\{-l, -l+1, ..., l-1, l\}$ leading to a degeneracy of $(2l+1)$. And since, for each of these values, m_s can be either $\pm 1/2$, the total degeneracy of states with energy E_{nl} is twice this $2(2l+1)$.

It is standard to label ionic energy levels using the *spectroscopic notation*:

$$n^{2s+1}l \tag{2.52}$$

where we write, for historical reasons, $L = 0, 1, 2, 3$ as S, P, D, F (and rarely have to consider higher L). For example, the energy level containing the states $|n = 3, l = 2, s = 1/2, m_l, m_s\rangle$ is referred to as 3^2D.

Fine structure

The description in the previous section was implicitly nonrelativistic. However, our experiments are sensitive to the *fine structure* resulting from leading-order relativistic corrections to the Schrödinger equation. The scale of these effects is on the order of several tenths of an electron volt (two orders of magnitude smaller than the shielding effect from the inner electrons for low angular momentum states).

Of several effects at this scale, the so-called *spin-orbit* correction is the most qualitatively important since it further breaks the degeneracy of the electronic structure. The underlying

relativistic concept is the effective magnetic field experienced by a charged particle, in its own frame of reference, when moving relative to a stationary electric field. This principle applies to the valence electron because of its orbital motion through the central field. Thus, it experiences an effective magnetic field, which has the specific form [31]:

$$\mathbf{B}_{\text{eff}} = \frac{1}{mc^2}\left(\frac{1}{e\hat{r}}\frac{\partial U_{\text{CF}}}{\partial r}\right)\hat{\mathbf{L}} \tag{2.53}$$

$\mathbf{B}_{\text{eff}}$ then back couples to the electron through its magnetic dipole moment, giving rise to the spin-orbit interaction:

$$\hat{H}_{S-O} = -\hat{\boldsymbol{\mu}}_S \cdot \mathbf{B}_{\text{eff}} = f(\hat{r})\hat{\mathbf{L}} \cdot \hat{\mathbf{S}} \tag{2.54}$$

$\hat{H}_{S-O}$ can be treated perturbatively, but $\hat{L}_z$ and $\hat{S}_z$ do not commute[10] with it meaning that (l, m_l, s, m_s) are no longer *good* quantum numbers[11] in the sense of degenerate perturbation theory [22]. Instead, we construct the total angular momentum operator:

$$\hat{\mathbf{J}} = \hat{\mathbf{L}} + \hat{\mathbf{S}} \tag{2.55}$$

which we expect should be conserved in the absence of any external fields (and, therefore, any external torque). Then:

$$\hat{\mathbf{L}} \cdot \hat{\mathbf{S}} = \frac{1}{2}(\hat{J}^2 - \hat{L}^2 - \hat{S}^2) \tag{2.56}$$

and the associated operators $\hat{J}^2$ and $\hat{J}_z$ *do* commute with $\hat{H}_{S-O}$, as can be easily checked. So (l, s, j, m_j) *are* good quantum numbers and the first-order perturbative shift of the energies due to the spin-orbit interaction can be easily calculated since it is diagonal in the good basis:

$$\Delta E_{S-O}^{(nlsj)} = \langle n, l, s, j, m_j | \hat{H}_{S-O} | n, l, s, j, m_j \rangle$$
$$= \beta\{j(j+1) - l(l+1) - s(s+1)\} \tag{2.57}$$
$$\beta_{nl} = \frac{\hbar^2}{4m_e^2 c^2}\left\langle \frac{1}{\hat{r}}\frac{\partial U_{\text{CF}}}{\partial r} \right\rangle \tag{2.58}$$

The spin-orbit interaction couples the orbital angular momentum to the spin such that, for stationary states, their relative orientation, as characterized by j, is always well defined. Moreover, j-states with the same l but different s are no longer degenerate, as is clear from Equation 2.57. Instead, the energy levels $n^{2s+1}l$ are broken into fine structure doublets specified by an additional subscript denoting the value of j:

---

[10]Recall, that for any angular momentum operator $\hat{\mathbf{A}}$, it follows that $[\hat{A}_i, \hat{A}_j] = i\hbar\epsilon_{ijk}\hat{A}_k$.

[11]Or, equivalently, $\{\hat{H}, \hat{L}^2, \hat{L}_z, \hat{S}^2, \hat{S}_z\}$ no longer form a CSCO.

$$n^{2s+1}l_j \equiv |n, l, s, j, m_j\rangle \tag{2.59}$$

The degeneracy of these fine structure levels is reduced to $2j + 1$.

As a final note, we mention that ^{40}Ca does not have hyperfine structure[12]. This turns out to be a general feature of any atom whose nucleus has both an even number of protons and an even number of neutrons[13] [66].

Spontaneous emission

When the ion is in an excited state, it will decay down to the ground state (or some lower-energy excited state) via emission of a photon with some finite probability that grows exponentially with time. This is known as spontaneous emission and can only be fully understood with a fully quantum treatment of the electromagnetic force [99]. For our purposes, this can be treated as a phenomenological fact.

The exponential decay constant is a property of a particular transition and is related to the corresponding matrix element of the vacuum field operator. Thus, transitions with larger decay constants also couple more strongly to externally applied fields. The decay constant is typically referred to as the Einstein A coefficient and is defined such that for two electronic states $|g\rangle$ and $|e\rangle$ ($|e\rangle$ the higher energy of the two):

$$\frac{dp_e}{dt} = -A_{eg}p_e \tag{2.60}$$

where $p_e(t)$ is the probability of measuring the ion to be in the state $|e\rangle$.

When there are multiple lower energy levels, the full decay rate out of the excited level is equal to:

$$A_e = \sum_i A_{ei} \tag{2.61}$$

where the sum is over all unoccupied, lower energy levels $\{|i\rangle\}$. The inverse of this quantity is known as the lifetime of the excited state. In Figure 2.8, we give the experimentally measured lifetimes for the relevant excited states in ^{40}Ca$^+$. We also list the rates associated with each transition $A_{ei}/2\pi$.

---

[12]Which results from interactions between the valence electron and higher multipole moments of the nucleus when present

[13]Only five stable nuclei have both an odd number of protons and an odd number of neutrons, so for practical purposes, one can usually assume that an atom with an even mass number has no hyperfine structure.

2.4 Zeeman substructure

The remaining $2j+1$ degeneracy present in the fine structure levels of ^{40}Ca$^+$ can be broken by applying a static magnetic field $\mathbf{B}_{\text{ext}}$ through what is referred to as the *Zeeman effect.* If the field is homogeneous, then it couples to the ion solely through its magnetic dipole moment $\hat{\boldsymbol{\mu}}$:

$$\hat{H}_{\text{Zeeman}} = -\hat{\boldsymbol{\mu}} \cdot \mathbf{B}_{\text{ext}} \tag{2.62}$$

where $\hat{\boldsymbol{\mu}}$ has contributions from both the spin of the valence electron and its orbital motion. The former is given by Equation 2.48. To find the latter we begin by defining the vector potential:

$$\mathbf{A} = \frac{B}{2}(-y\hat{\mathbf{x}} + x\hat{\mathbf{y}}) \tag{2.63}$$

such that :

$$\mathbf{B}_{\text{ext}} = \nabla \times \mathbf{A} = B\hat{\mathbf{z}} \tag{2.64}$$

where we have taken the magnetic field to point in the $\hat{\mathbf{z}}$-direction without any further loss of generality since, in the absence of the external magnetic field, the ion does not have a well-defined absolute orientation in space[14]. The specific choice of the z-axis is arbitrary but consistent with our choice of the $\hat{L}_z$ and $\hat{S}_z$ operators in the previous section.

Now we can treat the field-ion interaction semi-classically by modifying the canonical momentum in the central-field Hamiltonian in Equation 2.43 $\hat{\mathbf{p}} \to \hat{\mathbf{p}} + e\mathbf{A}(\hat{\mathbf{r}})$, such that:

$$\hat{H}_{\text{CF}} \underset{\mathbf{A}}{\to} \frac{[\hat{\mathbf{p}} + e\mathbf{A}(\hat{\mathbf{r}})]^2}{2m_e} + U_{\text{CF}}(\hat{r}) \tag{2.65}$$

$$= \frac{\hat{p}^2}{2m_e} + U_{\text{CF}} + \frac{e^2 A^2}{2m_e} + \frac{e}{2m_e}(\hat{\mathbf{p}} \cdot \mathbf{A} + \mathbf{A} \cdot \hat{\mathbf{p}}) \tag{2.66}$$

$$= \frac{\hat{p}^2}{2m_e} + U_{\text{CF}} + \frac{e^2 A^2}{2m_e} + \frac{e}{2m_e}\hat{\mathbf{L}} \cdot \mathbf{B} \tag{2.67}$$

The first two terms in Equation 2.67 are just the original central-field Hamiltonian $\hat{H}_{\text{CF}}$. The third, so-called *diamagnetic term*, term involves a two-photon process where the first photon induces a magnetic dipole moment that the second photon interacts with. This term can always be neglected for the field strengths achievable in our laboratory[15]. The last term can be interpreted as the interaction of the magnetic field with the magnetic dipole moment

---

[14]For this reason, applying a magnetic field is sometimes referred to as "setting the quantization axis of the ion."

[15]We can ask when $\frac{e^2 A^2}{2m} \sim \frac{eBa_0^2}{2m} \ll \mu_B B$, which occurs when $B \ll \frac{\hbar}{ea_0^2} \sim 10^5$ T.

due to any anisotropic orbital motion of the valence electron (producing a current-loop in the classical picture):

$$\hat{\boldsymbol{\mu}}_L = -\frac{e}{2m}\hat{\mathbf{L}} = -g_l\mu_B\frac{\hat{\mathbf{L}}}{\hbar} \tag{2.68}$$

Thus:

$$\hat{\boldsymbol{\mu}} = -\frac{\mu_B}{\hbar}(g_l\hat{\mathbf{L}} + g_s\hat{\mathbf{S}}) \approx -\frac{\mu_B}{\hbar}(\hat{\mathbf{L}} + 2\hat{\mathbf{S}}) = -\frac{\mu_B}{\hbar}(\hat{\mathbf{J}} + \hat{\mathbf{S}}) \tag{2.69}$$

where in the second approximate equality we have taken[16] $g_l \approx 1$ and $g_s \approx 2$.

With the addition of $\hat{H}_{\text{Zeeman}}$, the full Hamiltonian describing the ion's internal structure is now:

$$\hat{H} = \hat{H}_{\text{CF}} + \hat{H}_{\text{FS}} + \hat{H}_{\text{Zeeman}} \tag{2.70}$$

where $\hat{H}_{\text{FS}}$ describes the leading order fine structure effects including $\hat{H}_{S-O}$ and all of similar orders of magnitude. In practice, we typically apply a magnetic field of about 4 Gauss, which leads to Zeeman shifts on the order of $|\hat{H}_{\text{Zeeman}}/h| \sim \frac{\mu_B}{h}B \sim 1$ MHz. In comparison, the spin-orbit term $\hat{H}_{S-O}$ creates a frequency splitting on the order of THz (see Figure 2.8). Therefore, we can safely treat $\hat{H}_{\text{Zeeman}}$ as a perturbation on top of the fine structure.

The first-order Zeeman shift of the energy levels is then given by:

$$\Delta E_{\text{Zeeman}}^{(n,l,s,j,m_j)} = -\langle n,l,s,j,m_j|\hat{H}_{\text{Zeeman}}|n,l,s,j,m_j\rangle \tag{2.71}$$

$$= \frac{\mu_B}{\hbar}\langle n,l,s,j,m_j|\hat{\mathbf{J}} + \hat{\mathbf{S}}|n,l,s,j,m_j\rangle \cdot \mathbf{B} \tag{2.72}$$

The states $|n,l,s,j,m_j\rangle$ are not eigenstates of $\hat{\mathbf{S}}$, but we can compute the expectation value $\langle n,l,s,j,m_j|\hat{\mathbf{S}}|n,l,s,j,m_j\rangle$ using the projection theorem [22]:

$$\langle\hat{\mathbf{S}}\rangle = \frac{\langle\hat{\mathbf{S}}\cdot\hat{\mathbf{J}}\rangle}{\hbar^2 j(j+1)}\langle\hat{\mathbf{J}}\rangle \tag{2.73}$$

Such that the magnetic substates of the fine structure levels are each shifted by an amount[17]:

$$\Delta E_{\text{Zeeman}}^{(n,l,s,j,m_j)} = g_J\mu_B B m_j \tag{2.74}$$

that is linear in the magnetic field strength. Here the quantity g_J is known as the Landè g-factor and is given by:

$$g_J = 1 + \frac{j(j+1) - l(l+1) + s(s+1)}{2j(j+1)} \tag{2.75}$$

---

[16]g_l is not exactly one for several reasons including the fact that m_e should be replaced by the reduced mass.

[17]A good quantity to remember here is the $\mu_B/h \sim 1.4$ MHz/Gauss.
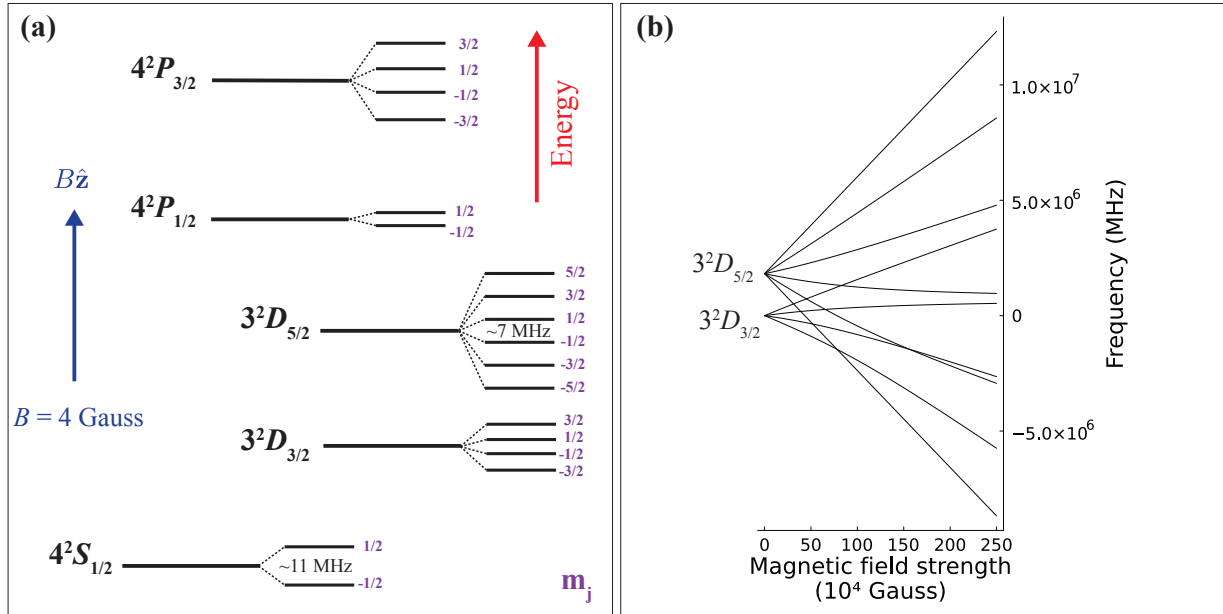
Figure 2.9: $^{40}\text{Ca}^+$ Zeeman substructure. **(a)**. For typical operating fields of magnitude $|\mathbf{B}| \sim 4$ Gauss, the Zeeman shift of the $^{40}\text{Ca}^+$ fine structure magnetic sublevels is approximately linear with field strength and proportional to $\hat{J}_z$. At 4 Gauss, nonlinear corrections are on the order of several Hz or 1 part per million relative to the linear response. **(b)**. Substantial mixing between, for example, the $3^2D_{5/2}$ and $3^2D_{3/2}$ does not occur until the external field reaches a value of around 3 Tesla (where it begins to become comparable to the effective, internal magnetic field due to the motion of the valence electron around the nucleus (Equation 2.53).

The first-order shift in Equation 2.74 might as welll have been generated by the notional interaction $-\hat{\boldsymbol{\mu}}_J \cdot \mathbf{B}$ with $\hat{\boldsymbol{\mu}}_J = g_J \mu_B \hat{\mathbf{J}}$, even though the actual dipole moment is proportional to $(\hat{\mathbf{J}} + \hat{\mathbf{S}})$.

An illustration of the Zeeman effect is given in Figure 2.9. The first-order approximation of the Zeeman effect is sufficient for all the work performed in this thesis. However, in Chapter 6 we do need to consider higher-order corrections more quantitatively. It is possible to treat $\hat{H}_{\text{Zeeman}}$ on an equal footing with $\hat{H}_{\text{FS}}$ by rewriting $\hat{H}_{\text{Zeeman}}$ in the coupled basis $|n, l, s, j, m_j\rangle$, summing it with $\hat{H}_{S-O}$ and then diagonalizing the result. An algorithm for performing this is given in Appendix B and the result of this more rigorous treatment is plotted in Figure 2.9(b) for a wide range of magnetic field strengths. At 4 Gauss, the leading correction to Equation 2.74 (nonlinear in B) is on the order of several Hz.

2.5 Effect of external electric fields on ion structure

In this section, we ask what effect a static external electric field $\mathbf{E}(\mathbf{r})$ generated by the potential $\phi(\mathbf{r})$ has on the internal structure of an ion. Of course, there is an interaction with the net charge of the ion and, since we assume the ion is trapped, the field at the center of mass position of the ion $\mathbf{r}_0$ must be zero $\mathbf{E}(\mathbf{r}_0) = 0$. However, this is only ever true in the time-averaged sense due to the ion's micromotion, vibrational motion and ubiquitous, fluctuating ambient field noise. Moreover, a field can have spatial variations over the length scale of an ion such that $\mathbf{E}(\mathbf{r}_0) = 0$ but $\mathbf{E}(\mathbf{r}) \neq 0$ where $\mathbf{r}$ is the position of the valence electron.

For these reasons, we will assume a *quasi*-static electric field such that the time dependence is slow relative to the response time of the ion's internal degrees of freedom[18]. And we will expand the electric potential about the center of mass position of the ion, leading to an interaction Hamiltonian described in terms of the ion's multipole moments:

$$\hat{H}_E = e\Phi(\mathbf{r}_0) - \hat{\mathbf{d}} \cdot \mathbf{E}(\mathbf{r}_0) - \frac{1}{6}\hat{\mathbf{Q}}\nabla\mathbf{E}(\mathbf{r}_0) + \dots \tag{2.76}$$

where:

$$\hat{d}_i = -e\hat{r}_i \tag{2.77}$$

$$\hat{Q}_{ij} = -e(3\hat{r}_i\hat{r}_j - |\hat{\mathbf{r}}|^2\delta_{ij}) \tag{2.78}$$

are the electric dipole and quadrupole operators. This is a semi-classical treatment, and Equation 2.76 is exactly analogous to the classical multipole expansion [35] of a charged particle interacting with an externally sourced potential after performing the canonical quantization. The quasi-static assumption is reflected in the fact that we do not explicitly reference time in Φ and its derivatives, since we assume that these are essentially constant over the interaction time scales which we will consider.

Electric monopole and dipole interactions

The first term on the right-hand side of in Equation 2.76 describes the interaction of the field with the ion's net charge, which does not affect its external structure since we assume the field strengths are small enough such that this quantity is conserved (no further ionization). The second term is the electric counterpart to $\hat{H}_{\text{Zeeman}}$ in Equation 2.62. However, in contrast to its magnetic dipole moment, the electric dipole moment for stationary states of $^{40}\text{Ca}^+$ is generally zero. This is most easily argued by making use of the parity operator $\hat{\pi}$ whose action is an inversion of spatial coordinates. Fine structure eigenstates have a well-defined parity [22]:

---

[18]In other words, we assume that the time scale over which the electric field changes is slow enough to be considered adiabatic – no instantaneous jumps between eigenstates of the internal Hamiltonian.

$$\hat{\pi}|n, l, s, j, m_j\rangle = (-1)^l |n, l, s, j, m_j\rangle \tag{2.79}$$

and the dipole operator is odd under parity:

$$\hat{\pi}\hat{\mathbf{d}}\hat{\pi}^\dagger = -e\hat{\pi}\hat{\mathbf{r}}_e\hat{\pi}^\dagger = e\hat{\mathbf{r}}_e = -\hat{\mathbf{d}} \tag{2.80}$$

Therefore, taking α to subsume all quantum numbers other than l:

$$\langle\alpha, l|\hat{\mathbf{d}}|\alpha, l\rangle = \langle\alpha, l|\hat{\pi}^\dagger\hat{\pi}\hat{\mathbf{d}}\hat{\pi}^\dagger\hat{\pi}|\alpha, l\rangle = (-1)^{2l}\langle\alpha, l|\hat{\pi}\hat{\mathbf{d}}\hat{\pi}^\dagger|\alpha, l\rangle = -\langle\alpha, l|\hat{\mathbf{d}}|\alpha, l\rangle \tag{2.81}$$

which implies $\langle\hat{\mathbf{d}}\rangle = 0$.

Similar to our interpretation of the diamagnetic term in the previous section, the electric field can induce a dipole moment in the ion by mixing fine structure states, which it will then interact with. The resulting energy shift can be found with second-order perturbation theory:

$$\Delta E^{(n,l,s,j,m_j)} = \sum_{(n',l',s',j',m'_j)} \frac{|\langle n', l', s', j', m'_j|\hat{\mathbf{d}}\cdot\mathbf{E}|n, l, s, j, m_j\rangle|^2}{E_{nl} - E_{n'l'}} \tag{2.82}$$

But for the low-lying excited states of $^{40}Ca^+$, $|E_{nl} - E_{n'l'}|/h \sim 10^2$ THz. And the numerator in Equation 2.82, which is related to the spontaneous emission rate from the higher to the lower of $\{|n, l, j, m_j\rangle|, |n', l', j', m'_j\rangle\}$ is typically no more than $\sim 10^2$ MHz. Therefore, the quadratic Stark shift should be on the order of[19] 10^{-6} Hz / $(V/m)^2$. For typical field strengths and parameters of our experiments, this effect is negligible.

Electric quadrupole interaction

In contrast to the dipole operator, the quadrupole operator $\hat{\mathbf{Q}}$:

$$\hat{Q}_{ij} = -e(3\hat{r}_i\hat{r}_j - |\hat{\mathbf{r}}|^2\delta_{ij}) \tag{2.83}$$

is even under parity, allowing for the possibility of fine structure states with a permanent quadrupole moment. A finite electric field gradient at the position of the ion will then cause an energy shift:

$$\Delta E_{quadrupole} = -\frac{1}{6}\langle\hat{\mathbf{Q}}\rangle\nabla\mathbf{E}(\mathbf{r}_0) \tag{2.84}$$

It turns out that $3^2D_{5/2}$ level of $^{40}Ca^+$ does have a permanent quadrupole moment. That is to say, in general:

$$\langle 3^2D_{5/2}, m_j|\hat{\mathbf{Q}}|3^2D_{5/2}, m_j\rangle \neq 0 \tag{2.85}$$

---

[19]Which agrees with measured values [100]

Moreover, because of the static trapping potential in the axial direction (Equation 2.15), there will always be a finite electric field gradient at the position of the ion:

$$\mathbf{E}_{\text{endcaps}}(\mathbf{r}) = \frac{U_z}{\tilde{Z}^2}[x\hat{\mathbf{x}} + y\hat{\mathbf{y}} - 2z\hat{\mathbf{z}}] = \frac{m\omega_z^2}{2}[x\hat{\mathbf{x}} + y\hat{\mathbf{y}} - 2z\hat{\mathbf{z}}] \tag{2.86}$$

$$\nabla\mathbf{E}_{\text{endcaps}} = \frac{m\omega_z^2}{2}\begin{bmatrix} 1 & & \\ & 1 & \\ & & -2 \end{bmatrix} \tag{2.87}$$

and, thus, a corresponding shift of the $3^2D_{5/2}$ energies. If we assume that the electric field gradient is entirely due to the trapping potential and that there are no DC potentials applied to the radial electrodes, then the magnitude of this shift is given by [81, 85, 50]:

$$\Delta_{quadrupole}^{D_{5/2}} = \frac{m\omega_z^2}{e}|Q_{3^2D_{5/2}}|A \times \begin{cases} -1 \text{ if } m_j = \pm 5/2 \\ 1/5 \text{ if } m_j = \pm 3/2 \\ 4/5 \text{ if } m_j = \pm 1/2 \end{cases} \tag{2.88}$$

where $|Q_{3^2D_{5/2}}|$ characterizes the magnitude of the $3^2D_{5/2}$ quadrupole moment and is given by the reduced matrix element:

$$|Q_{3^2D_{5/2}}| = -e\langle 3^2D_{5/2}||\hat{r}^2C_0^{(2)}||3^2D_{5/2}\rangle \tag{2.89}$$

where $C_l^{(m)}$ is a Racah normalized spherical harmonic $\sqrt{\frac{4\pi}{2l+1}}Y_l^m(\theta, \phi)$ and $0 \leq 1$ is a geometrical factor that takes into account the orientation of the electric field with the quantization axis of the ion. This is a small but measurable effect (typically on the order of 1-10 Hz), as will be discussed in Chapter 6. A detailed derivation of Equation 2.88 is given in [50].

2.6 Light-ion interactions

Basic interaction

Electromagnetic fields oscillating with frequencies near the frequency splittings of the bare atomic states are capable of resonantly driving population[20] between these states. In our experiments, we use focused laser beams for this purpose, which are most simply modeled as traveling, monochromatic plane waves described by a vector potential $\mathbf{A}$ in the radiation gauge $\nabla \cdot \mathbf{A} = 0$ of the following form:

$$\mathbf{A}(\mathbf{r}, t) = \frac{A_0}{2}\hat{\boldsymbol{\epsilon}}e^{i(\mathbf{k}\cdot\mathbf{r}-\omega_L t)} + \text{c.c.} \tag{2.90}$$

where $\mathbf{k} = (2\pi/\lambda)\hat{\mathbf{k}}$ is the laser beam's wave vector in terms of its wavelength λ and its direction of travel $\hat{\mathbf{k}}$ and ω_L is its corresponding frequency related by the vacuum dispersion relation $\omega_L/|\mathbf{k}| = c$ (with c the speed of light in vacuum). The corresponding electric and magnetic fields are then given by:

$$\mathbf{E}(\mathbf{r}, t) = -\frac{\partial \mathbf{A}}{\partial t} = \frac{1}{2}(i\omega_L A_0)\hat{\boldsymbol{\epsilon}}e^{i(\mathbf{k}\cdot\mathbf{r}-\omega_L t)} + \text{c.c.} \tag{2.91}$$

$$\mathbf{B}(\mathbf{r}, t) = \nabla \times \mathbf{A} = \frac{1}{2}iA_0(\mathbf{k} \times \hat{\boldsymbol{\epsilon}})e^{i(\mathbf{k}\cdot\mathbf{r}-\omega_L t)} + \text{c.c.} \tag{2.92}$$

The effect of the vector potential $\mathbf{A}$ can be incorporated into the atomic Hamiltonian the same way as in Equation 2.65. Just as we did there, if we drop the diamagnetic term and use the fact that $[\mathbf{A}(\hat{\mathbf{r}}), \hat{\mathbf{p}}] = 0$ in the radiation gauge, then the total semiclassical Hamiltonian can be broken down into two components $\hat{H}_0$ and $\hat{H}_{\text{int}}$ such that [22]:

$$\hat{H} = \hat{H}_0 + \hat{H}_{\text{int}} \tag{2.93}$$

where $\hat{H}_0$ represents the "bare" atomic Hamiltonian due to the central field, fine structure and, perhaps, a static magnetic field as in Section 2.4:

$$\hat{H}_0 = \sum_i E_i|E_i\rangle\langle E_i|, \quad |E_i\rangle \sim |n_i, l_i, j_i, (m_j)_i\rangle \tag{2.94}$$

And $\hat{H}_{\text{int}}$ captures the interaction with the light field:

$$\hat{H}_{\text{int}} = \frac{e}{m}\mathbf{A}(\hat{\mathbf{r}}) \cdot \hat{\mathbf{p}} = \frac{1}{2}\frac{eA_0}{m}e^{-i\omega_L t}e^{i\mathbf{k}\cdot\hat{\mathbf{r}}}\hat{\boldsymbol{\epsilon}} \cdot \hat{\mathbf{p}} + \text{h.c.} \tag{2.95}$$

$$= \frac{1}{2}\sum_{ij}e^{-i\omega_L t}\langle E_i|\frac{eA_0}{m}e^{i\mathbf{k}\cdot\hat{\mathbf{r}}}\hat{\boldsymbol{\epsilon}} \cdot \hat{\mathbf{p}} + \text{h.c.}|E_j\rangle|E_i\rangle\langle E_j| \tag{2.96}$$

---

[20]By which we mean the probability of finding the atom in a particular state when measured.

Interaction picture

It is usually convenient to perform calculations using the time-dependent basis defined by the transformation $|\tilde{E}_i\rangle = \hat{U}|E_i\rangle$, where:

$$\hat{U} = \exp(i\hat{H}_0 t/\hbar) \tag{2.97}$$

This is referred to as moving to the *interaction picture* with respect to the bare Hamiltonian $\hat{H}_0$. An arbitrary operator $\hat{A}$ in this reference frame is transformed according to:

$$\hat{A} \to \hat{\tilde{A}} = \hat{U}\hat{A}\hat{U}^\dagger \tag{2.98}$$

and the Hamiltonian is redefined as:

$$\hat{H} \to \hat{\tilde{H}} = \hat{U}\hat{H}\hat{U}^\dagger + i\hbar(\partial_t\hat{U})\hat{U}^\dagger \tag{2.99}$$

$$= \hat{U}\hat{H}_{\text{int}}\hat{U}^\dagger \tag{2.100}$$

such that the interaction picture Schrödinger equation retains the familiar form:

$$i\hbar\partial_t|\tilde{\psi}\rangle = \hat{\tilde{H}}|\tilde{\psi}\rangle \tag{2.101}$$

$\hat{\tilde{H}}$ is given explicitly by:

$$\hat{\tilde{H}} = \frac{1}{2}\sum_{ij}|E_i\rangle\langle E_j|\left[e^{-i\Delta_{ij}^{(-)}t}\langle E_i|\frac{eA_0}{m}e^{i\mathbf{k}\cdot\hat{\mathbf{r}}}\hat{\boldsymbol{\epsilon}}\cdot\hat{\mathbf{p}}|E_j\rangle + e^{-i\Delta_{ij}^{(+)}t}\langle E_i|\frac{eA_0}{m}e^{-i\mathbf{k}\cdot\hat{\mathbf{r}}}\hat{\boldsymbol{\epsilon}}\cdot\hat{\mathbf{p}}|E_j\rangle\right] \tag{2.102}$$

where $\Delta_{ij}^{(\pm)} = \omega_L \pm \frac{E_i-E_j}{\hbar}$ when $i > j$ and $\Delta_{ji}^{(\pm)} = -\Delta_{ij}^{(\pm)}$. Note that expectation values in the interaction picture are consistent with the lab frame:

$$\langle\tilde{\psi}|\hat{\tilde{A}}|\tilde{\psi}\rangle = \langle\psi|\hat{U}^\dagger\hat{U}\hat{A}\hat{U}^\dagger\hat{U}|\psi\rangle = \langle\psi|\hat{A}\psi\rangle \tag{2.103}$$

Rotating wave approximation

It can be argued (for example in [32]) that the faster-oscillating terms in Equation 2.102 play a less significant role in the time evolution described by Equation 2.101. In this case, we can make a *rotating wave approximation* (RWA) by discarding terms that oscillate faster than some threshold value[21]. If we assume that the center frequency of the light field is tuned near a particular transition $|E_\alpha\rangle \to |E_\beta\rangle$, such that $\omega_L \sim \Delta_{\alpha\beta}^{(-)}$, then it is often a good approximation to set the RWA threshold low enough so that only terms including $|E_\alpha\rangle\langle E_\beta|$

---

[21]In practice, the validity of this approximation can typically be confirmed through direct simulation.

in $\hat{\tilde{H}}$ are retained. This is sometimes referred to as the two-level approximation. In this case, the counter-rotating terms that oscillate at $\Delta_{\alpha\beta}^{(+)}$ are also neglected, so we have:

$$\hat{\tilde{H}}_{\text{RWA}} = \hbar \frac{\Omega_{\alpha\beta}}{2} e^{-i\Delta_{\alpha\beta}^{(-)}t} \hat{\sigma}_{\alpha\beta} + \text{h.c.} \tag{2.104}$$

where:

$$\Omega_{\alpha\beta} = \langle E_\alpha | \frac{eA_0}{m} e^{i\mathbf{k}\cdot\hat{\mathbf{r}}} \hat{\boldsymbol{\epsilon}} \cdot \hat{\mathbf{p}} | E_\beta \rangle \tag{2.105}$$

and $\hat{\sigma}_{\alpha\beta} = |E_\alpha\rangle\langle E_\beta|$.

Multipole decomposition

Just as in Section 2.5, it is standard to expand the plane wave term in Equation 2.105 about the center of mass position of the ion $\hat{\mathbf{r}}_0$. If we label the position of the valence electron as $\hat{\mathbf{r}}_e = \hat{\mathbf{r}} - \hat{\mathbf{r}}_0$, then we have:

$$\langle E_\alpha | \frac{eA_0}{m} e^{i\mathbf{k}\cdot\hat{\mathbf{r}}} \hat{\boldsymbol{\epsilon}} \cdot \hat{\mathbf{p}} | E_\beta \rangle = e^{i\mathbf{k}\cdot\hat{\mathbf{r}}_0} \langle E_\alpha | \frac{eA_0}{m} [1 + i\mathbf{k}\cdot\hat{\mathbf{r}}_e + \ldots] \hat{\boldsymbol{\epsilon}} \cdot \hat{\mathbf{p}} | E_\beta \rangle \tag{2.106}$$

It can be shown that the first term in the expansion reduces to an electric dipole interaction of the form discussed in section 2.5, the second term reduces to the sum of an electric quadrupole transition of the form discussed in section 2.5 and a magnetic dipole interaction of the form discussed in section 2.4. The third term leads to an electric octupole interaction and a magnetic quadrupole interaction and so forth.

The scaling of these terms, from one multipole to the next higher order, goes as ka_0, which is on the order of 10^{-4} for optical transitions. The ratio of a 2^K electric multipole transition over a 2^K magnetic multipole transition goes as $\approx 10^{-2}$. Moreover, electric and magnetic multipole moments of the same order have opposite parity, so generally do not contribute to the same transition (based on a similar argument as in Section 2.5). For these reasons, it is usually only necessary to consider the leading order term in Equation 2.106 and it is customary to denote the transition by the multipole interaction corresponding to this term. For example, electric and magnetic dipole transitions are referred to as E1 and M1 transitions, respectively. Electric and magnetic quadrupole transitions are referred to as E2 and M2 transitions, respectively. And so forth. A diagram illustrating the relevant multipole transitions for $^{40}\text{Ca}^+$ is given in Figure 2.10.

In this thesis, we only work with electric multipole transitions[22]. The coupling strength of an arbitrary electric 2^K-pole transition between the states $|E_\alpha\rangle = |n', l', j', m_j'\rangle$ and $|E_\beta\rangle = |n, l, j, m_j\rangle$ can be written as [95]:

---

[22]Though, in principle, M1 transitions are available. See Figure 2.10 and [44].
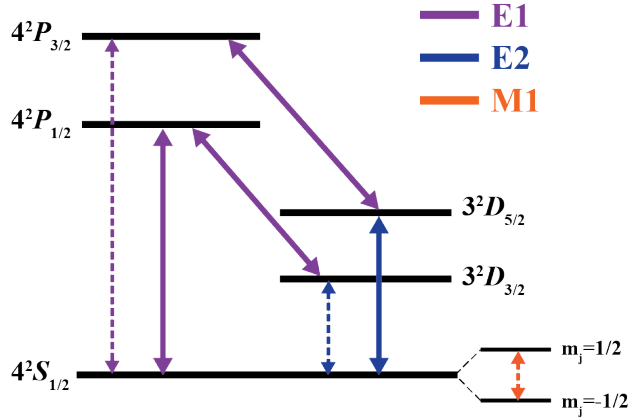
Figure 2.10: Dominant multipole transitions for ^{40}Ca$^+$. Solid lines represent transitions utilized in this thesis. Not shown are the various M1 transitions between magnetic sublevels of other hyperfine levels other than $S_{1/2}$.

$$\hbar\Omega_{\alpha\beta}^K = \sum_{q=-K}^{K} g_{Kq}(\theta,\rho)\langle E_\alpha|\hat{H}_q^{EK}|E_\beta\rangle \tag{2.107}$$

where $g_Kq(\theta,\phi)$ takes into account the geometry of the laser light and its polarization relative to the quantization axis of the ion[23] (see Figure 2.11(a)). This corresponds to the quantity $\mathbf{Y}_{Kq}(\hat{\mathbf{k}})\cdot\hat{\boldsymbol{\epsilon}}$ in Appendix C, where it is fully defined. For reference, we plot $g_{Kq}(\theta,\rho)$ for $K=1$ and $K=2$ in Figure 2.11. We also plot this function for circularly polarized light (relative to the direction of propagation $\hat{\mathbf{k}}$) in Figure 2.12, though, in this case, it only depends on the angle θ between $\hat{\mathbf{k}}$ and the quantization axis of the ion.

The matrix element in Equation 2.107 is given explicitly by:

$$\langle E_\alpha|\hat{H}_q^{EK}|E_\beta\rangle = 8\pi e E_0 (ik)^{K-1} b_K (-1)^{j'-m'_j} \begin{pmatrix} j' & K & j \\ -m'_j & q & m' \end{pmatrix} \langle E_\alpha||\hat{Q}_K||E_\beta\rangle \tag{2.108}$$

$$b_K = \sqrt{\pi\frac{(2K+1)(K+1)}{K}}\frac{4}{(2K+1)!!} \tag{2.109}$$

where $E_0 = i\omega_L A_0$, the term in big parentheses represents a Wigner 3-j symbol and $\langle E_\alpha||\hat{Q}_K||E_\beta\rangle$ is the reduced matrix element of the K-th order electric multipole operator in the spherical basis:

---

[23]Note: to be consistent with e.g. [85], the geometric factor must include the factor b_K as defined in Equation 2.109.
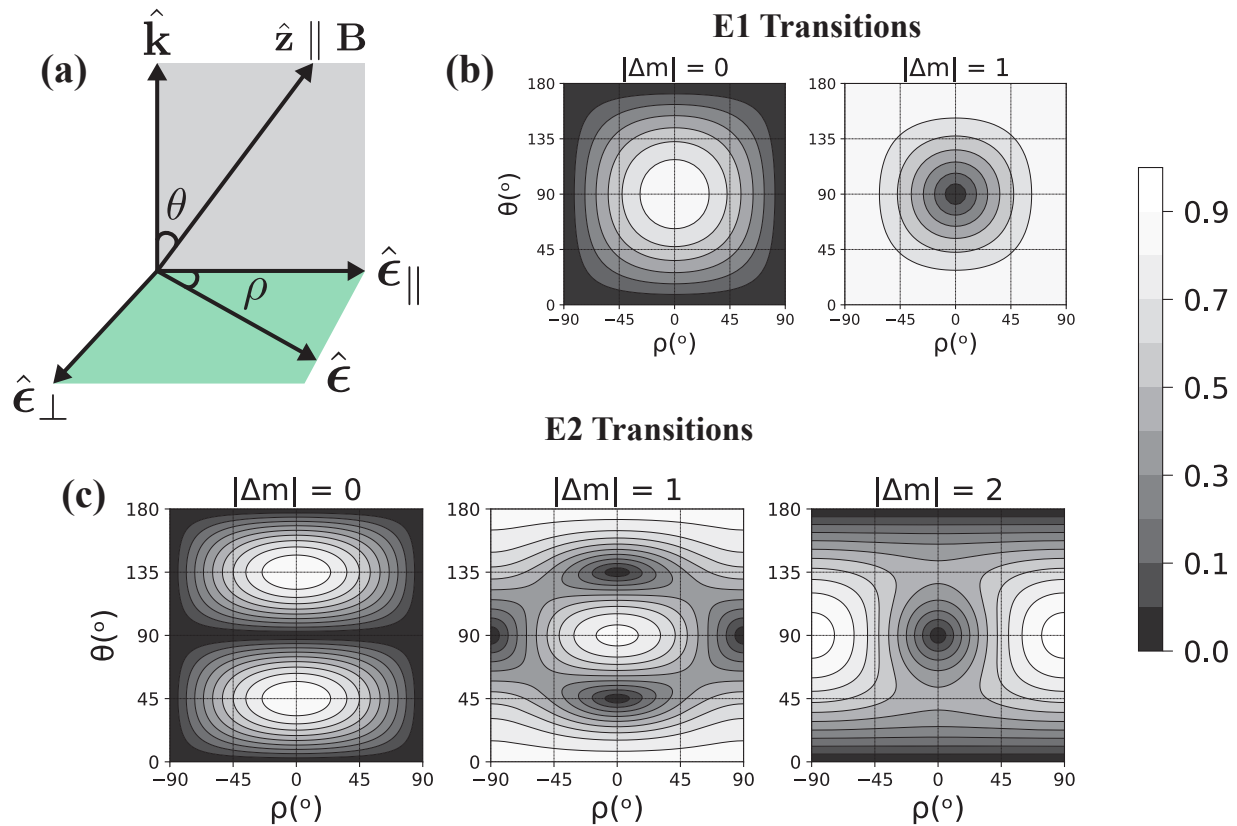
Figure 2.11: Geometrical dependence of the coupling strength for linearly polarized light. The plots in **(b)** and **(c)** give the relative coupling strengths (normalized to one) for E1 and E2 transitions as a function of the geometry between linearly polarized laser light and the ion as defined in **(a)** where $\hat{\boldsymbol{\epsilon}}_{\parallel}$ is defined as the component of the electric polarization vector in the plane formed by $\hat{\mathbf{k}}$ and $\mathbf{B}$ and $\hat{\boldsymbol{\epsilon}}_{\perp}$ is the component normal to this plane. Code for generating these plots for an arbitrary electric 2^K-pole interaction is provided in Appendix C.
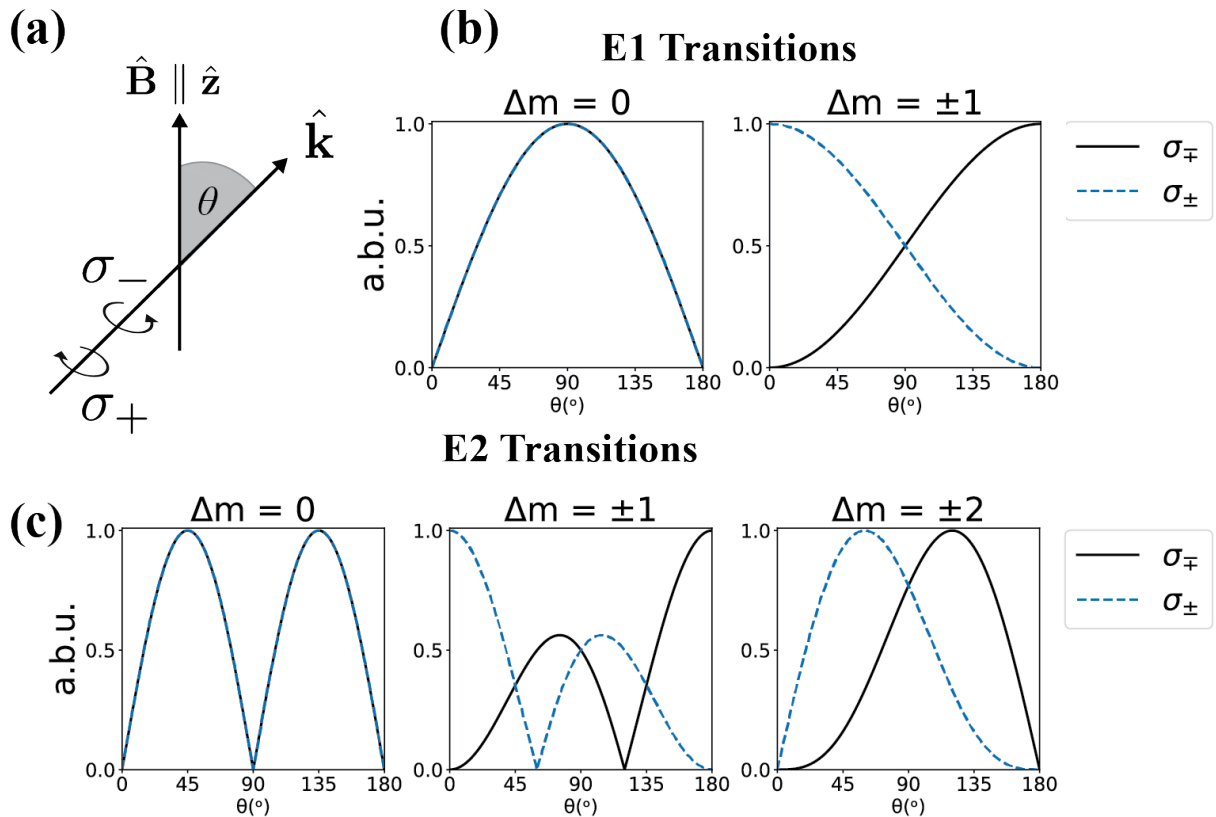
Figure 2.12: Geometrical dependence of the coupling strength for circularly polarized light. The plots in **(b)** and **(c)** give the relative coupling strengths (normalized to one) for E1 and E2 transitions as a function of the geometry between circularly polarized laser light and the ion as defined in **(a)**. $\sigma_\pm$ polarized light is defined by $\hat{\boldsymbol{\sigma}}_\pm = \mp(\hat{\boldsymbol{\epsilon}}_1 \pm i\hat{\boldsymbol{\epsilon}}_2)/\sqrt{2}$ where $\hat{\boldsymbol{\epsilon}}_1 = \hat{\mathbf{y}}$ and $\hat{\boldsymbol{\epsilon}}_2 = \sin(\theta)\hat{\mathbf{z}} - \cos(\theta)\hat{\mathbf{x}}$. Code for generating these plots for an arbitrary electric 2^K-pole interaction is provided in Appendix C.

α	β	K	λ	E_0	$\Omega_{\alpha\beta}^K/2\pi$
$S_{1/2},\ m_j = -1/2$	$P_{1/2},\ m_j = -1/2$	1	397 nm	7.3×10^4 V/m	2.3 GHz
$S_{1/2},\ m_j = -1/2$	$P_{1/2},\ m_j = -1/2$	1	397 nm	7.3×10^5 V/m	23 GHz
$S_{1/2},\ m_j = -1/2$	$D_{5/2},\ m_j = -1/2$	2	729 nm	7.3×10^4 V/m	0.65 MHz
$S_{1/2},\ m_j = -1/2$	$D_{5/2},\ m_j = -1/2$	2	729 nm	7.3×10^5 V/m	6.5 MHz

Table 2.2: Light-ion coupling strengths for typical experimental parameter configurations. $E_0 \approx 7.3 \times 10^4$ corresponds to 10 mW laser light in a Gaussian beam focused down to a spot with a waist of 30 μm to and $E_0 \approx 7.3 \times 10^5$ corresponds to the same but with a 3 μm waist.

$$\hat{Q}_{qK} = \hat{r}^K \sqrt{\frac{4\pi}{2K+1}} Y_k^q \tag{2.110}$$

with Y_k^q a spherical harmonic labeled in the standard way. The Wigner 3-j symbol enforces the selection rules $|j' - j| \leq K \leq j' + j$ and $q = m_j' - m_j$. And the reduced matrix element can be related to the Einstein A coefficient for the transition according to:

$$A_K = \frac{c\alpha(2K+2)(2K+1)k^{2K+1}}{K[(2K+1)!!]^2} \frac{|\langle E_\alpha||\hat{Q}_K||E_\beta\rangle|^2}{2j'+1} \tag{2.111}$$

where α is the fine structure constant, c is the speed of light in vacuum and it is important that the primed state $|E_\alpha\rangle$ is the higher energy state (such that the j' quantum number in the factor $2j' + 1$ corresponds to the higher energy state). Using Equations 2.107, 2.108 and 2.111 we can compute the quantity coupling strength $\Omega_{\alpha\beta}^K$ for an arbitrary electric multipole transition. Approximate coupling strengths for several common experimental parameter configurations are given in Table 2.2. See Appendix C for more details on the derivations in this section, and code for generating the plots in Figures 2.11, 2.12 and the data in Table 2.2.

Incorporating center of mass motion

Starting with the rotating wave approximation Hamiltonian in Equation 2.104, and dropping the subscripts and tildes we have the Hamiltonian for a simple, two-level system:

$$\hat{H} = \hbar \frac{\Omega}{2} e^{-i\Delta t} \hat{\sigma}_{eg} + \text{h.c.} \tag{2.112}$$

where we now label the states of the two-level system as $|e\rangle$ and $|g\rangle$ for excited and ground, respectively.

Now we would also like to consider the effect of the center of mass motion of the ion so we explicitly factor out the center of mass coordinate dependence in Ω in Equation 2.105 by

redefining $\Omega \to \tilde{\Omega}\exp(i\mathbf{k} \cdot \hat{\mathbf{r}}_0)$ and we also include the quantum description of the vibrational degrees of freedom as described in Equation 2.38:

$$\hat{H} = \hbar\frac{\Omega}{2}e^{ik\hat{z}_0\cos(\theta)}e^{-i\Delta t}\hat{\sigma} + \hbar\frac{\nu}{2}\hat{a}^\dagger\hat{a} + \text{h.c.} \tag{2.113}$$

$$= \hbar\frac{\Omega}{2}e^{ik\cos(\theta)(\hat{a}+\hat{a}^\dagger)}e^{-i\Delta t}\hat{\sigma} + \hbar\frac{\nu}{2}\hat{a}^\dagger\hat{a} + \text{h.c.} \tag{2.114}$$

where, for simplicity, we assume a single trapped ion and only consider vibration along the z-axis. θ is still the angle between $\hat{\mathbf{k}}$ and $\hat{\mathbf{z}}$. Just as we moved to the interaction picture in Equation 2.100 with respect to the ion's internal degrees of freedom, it is also convenient to do this for the ion's vibrational motion by defining another unitary operator $\hat{U}_\nu = \exp[i\nu\hat{a}^\dagger\hat{a}t]$. Then:

$$\hat{H} \underset{\hat{U}_\nu}{\to} \hbar\frac{\Omega}{2}e^{-i\Delta t}e^{i\eta(\hat{a}e^{i\nu t}+\hat{a}^\dagger e^{-i\nu t})}\hat{\sigma} + \text{h.c.} \tag{2.115}$$

where η is the so-called *Lamb-Dicke* parameter:

$$\eta = \mathbf{k} \cdot \hat{\mathbf{z}}_0 = k\cos(\theta)\sqrt{\frac{\hbar}{2m\nu}} \tag{2.116}$$

The exponential term in Equation 2.115 has the form of a displacement operator $\hat{D}(\alpha) = \exp(\alpha\hat{a}^\dagger - \alpha^*\hat{a})$ with $\alpha = i\eta e^{i\nu t}$ [36]. Using Equation 3.30 from reference [15], we can then resolve the components of the Hamiltonian in the Fock state basis:

$$\Omega_{mn} = \frac{2}{\hbar}\langle e, m|\hat{H}|g, n\rangle = \frac{2}{\hbar}\langle e, n|\hat{H}|g, m\rangle^* \tag{2.117}$$

$$= \Omega\langle m|\hat{D}(\alpha)|n\rangle = \Omega\left(\frac{n!}{m!}\right)^{1/2}\alpha^{m-n}e^{-|\alpha|^2/2}L_n^{(m-n)}(|\alpha|^2) \tag{2.118}$$

where $L_q^p(x)$ is an associated Laguerre polynomial.

However, it is more insightful to expand $\hat{H}$ from Equation 2.115 in η, which is a reasonable thing to do when $\eta\sqrt{n+1} \ll 1$ (the so-called *Lamb-Dicke regime*). In this case:

$$\hat{H} = \hbar\frac{\Omega}{2}e^{-i\Delta t}\hat{\sigma}\left[1 + i\eta\left(\hat{a}e^{i\nu t} + \hat{a}^\dagger e^{-i\nu t}\right) - \frac{\eta^2}{2}\left(2\hat{a}^\dagger\hat{a} + 1 + (\hat{a})^2 e^{2i\nu t} + (\hat{a}^\dagger)^2 e^{-2i\nu t}\right) + \dots\right] + \text{h.c.} \tag{2.119}$$

As illustrated in Figure 2.13, the Hamiltonian in Equation 2.119 describes several types of interactions that can be resonantly selected by tuning the value of Δ:

- **Carrier transitions**. When $\Delta = 0$:

$$\hat{H} \approx \hat{H}_{\text{carr}} = \hbar\frac{\Omega}{2}(1 - \eta^2\hat{a}^\dagger\hat{a})\hat{\sigma} + \text{h.c.} \tag{2.120}$$

- **Blue sideband transitions**. When $\Delta = \nu$:

$$\hat{H} \approx \hat{H}_{\text{bsb}} = \hbar\frac{i\eta\Omega}{2}\hat{a}^\dagger\hat{\sigma} + \text{h.c.} \tag{2.121}$$

- **Red sideband transitions**. When $\Delta = -\nu$:

$$\hat{H} \approx \hat{H}_{\text{rsb}} = \hbar\frac{i\eta\Omega}{2}\hat{a}\hat{\sigma} + \text{h.c.} \tag{2.122}$$

- **Higher order sideband transitions**. When $\Delta = q\nu$, $q \in \mathbb{Z}$:

Transitions to higher order red/blue sidebands can be driven with a coupling strength given by $\Omega_{n,n+1}$.
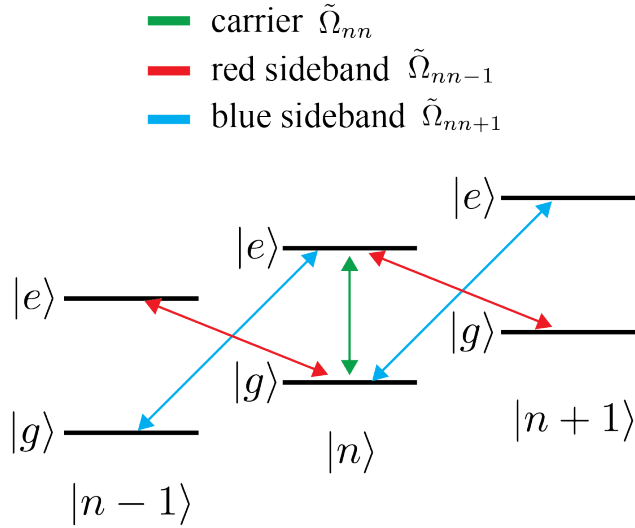
Figure 2.13: Lamb-Dicke regime. When the Lamb-Dicke parameter η (Equation 2.116) is small, the dynamics of a resonantly-selected electronic transition can be described by carrier transitions, which leave the motional state of the ion unchanged, blue sideband transitions, which drive $|g, n\rangle \leftrightarrow |e, n + 1\rangle$, and red sideband transitions, which drive $|g, n\rangle \leftrightarrow |e, n - 1\rangle$.

Generalizations

If we consider L laser beams interacting with N ions with M relevant vibrational modes then the Hamiltonian in the interaction picture is given by:

$$\hat{H} = \hbar \sum_{n=1}^{N} \sum_{l=1}^{L} \sum_{\substack{i_n=1 \\ j_n > i_n}}^{T_n} \frac{\Omega_{i_n j_n}}{2} \hat{\sigma}_{i_n j_n} e^{-i\Delta_{i_n j_n l} t} e^{i \sum_{m=1}^{M} \eta_{nlm}(\hat{a}_m e^{i\nu_m t} + \hat{a}_m^{\dagger} e^{-i\nu_m t})} + \text{h.c.} \tag{2.123}$$

where i_n refers to one of the T_n stationary states $|E_i\rangle_n$ of the nth ion that satisfy $\Delta_{i_n j_n l} < \Delta^*$ for some threshold value $\Delta^* \ll \omega_L$.

Spontaneous emission, as discussed in Section 2.3, generally must also be taken into account when considering the ion's dynamical evolution. But this requires a fully quantum treatment of the electromagnetic field. Instead, we can incorporate it in an ad-hoc manner by way of an approximate master equation [13]. But first we must define the density operator $\hat{\rho}$:

$$\hat{\rho} = \sum_i p_i |\psi_i\rangle\langle\psi_i| \tag{2.124}$$

$\hat{\rho}$ describes a classical distribution of quantum states, each realized with a probability of p_i. The Schrödinger equation can be expressed in terms of $\hat{\rho}$ as:

$$i\hbar\partial_t\hat{\rho} = [\hat{H}, \hat{\rho}] \tag{2.125}$$

Equation 2.125 is sometimes referred to as the Liouville equation, which is its classical analog. It reduces to $\partial_t|\psi\rangle = \hat{H}|\psi\rangle$ when $\hat{\rho} = |\psi\rangle\langle\psi|$ for some $|\psi\rangle$, which defines a pure state. Now, spontaneous emission from the state $|E_i\rangle$ to the state $|E_j\rangle$ can be incorporated into the dynamics described by Equation 2.125 by including a sum of terms:

$$i\hbar\partial_t\hat{\rho} = [\hat{H}, \hat{\rho}] + \sum_{ij} \gamma_{ij} \mathcal{L}(\hat{\rho}; \hat{\sigma}_{ij}) \tag{2.126}$$

where γ_{ij} refers to the Einstein A coefficient for the transition $|E_i\rangle \rightarrow |E_j\rangle$ ($|E_i\rangle$ assumed to be the higher energy state) and $\mathcal{L}(\hat{\rho}; \hat{A})$ is a Lindblad term of the form [63, 13]:

$$\mathcal{L}(\hat{\rho}; \hat{A}) = \hat{A}\hat{\rho}\hat{A}^{\dagger} - \frac{1}{2}\{\hat{A}^{\dagger}\hat{A}, \hat{\rho}\} \tag{2.127}$$

Near-resonant excitation

The effect of driving an electronic transition near resonance with laser light is to transfer population from one state to the other. For simplicity, we will describe this process for a carrier transition, as described by Equation 2.112, but the same analysis can be used for any other resonantly-selected two-level system (including motional sideband transitions)

and the basic procedure can be generalized for the case where we must consider more than two levels. It is convenient to transform Equation 2.112 into another rotating frame that preserves the essential physics, by way of the unitary operator $\hat{U} = \exp(-i\Delta t|e\rangle\langle e|)$. The effective Hamiltonian in this rotating frame is then found to be (Equation 2.99):

$$\hat{H}_{\mathrm{RF}} = \hbar\frac{\Omega}{2}|e\rangle\langle g| + \hbar\frac{\Delta}{2}|e\rangle\langle e| + \mathrm{h.c.} \tag{2.128}$$

If we take γ to be the spontaneous emission rate from $|e\rangle$ to $|g\rangle$, then from Equation 2.126, we find the equations of motion:

$$\dot{\rho}_{ee} = -i\frac{\Omega}{2}\rho_{ge} + i\frac{\Omega^*}{2}\rho_{eg} - \gamma\rho_{ee} \tag{2.129}$$

$$\dot{\rho}_{eg} = -(\gamma/2 + i\Delta)\rho_{eg} + i\frac{\Omega}{2}(\rho_{ee} - \rho_{gg}) \tag{2.130}$$

where $\rho_{ij} = \langle i|\hat{\rho}|g\rangle$ and the time evolution for the other two matrix elements follows immediately from the hermiticity of the density matrix ($\rho_{ge} = \rho_{eg}^*$) and conservation of probability ($\rho_{gg} + \rho_{ee} = 1$). This set of equations is often referred to as the *optical Bloch equations.*

Now we would like to consider the steady-state dynamics obtained for laser drive times long compared to $1/\gamma$. In this case, we assume that $\dot{\rho}_{ee} = \dot{\rho}_{eg} = 0$, which allows us to solve for ρ_{ee} using Equations 2.129 and 2.130:

$$\rho_{ee}^{(\mathrm{ss})} = \frac{R}{2R + \gamma/2} \tag{2.131}$$

where R is given by:

$$R = \frac{\gamma}{2}\left|\frac{\Omega/2}{\Gamma}\right|^2 \tag{2.132}$$

and Γ by:

$$\Gamma = \gamma/2 + i\Delta \tag{2.133}$$

For small drive strengths $|\Omega| \ll \gamma/2$, $\rho_{ee}^{(\mathrm{ss})}$ has the form of a Lorentzian with a full width at half maximum (FWHM) of γ:

$$\rho_{ee}^{(\mathrm{ss})} \approx \frac{|\Omega/2|^2}{(\gamma/2)^2 + \Delta^2} \tag{2.134}$$

At larger drive strengths $|\Omega| \sim \gamma$, the lineshape deviates from a Lorentzian due to an effect known as power broadening. This results from the fact that $\rho_{ee}^{(\mathrm{ss})}$ in Equation 2.131 saturates at a population of $1/2$ with respect to $|\Omega|$. This is illustrated in Figure 2.14.
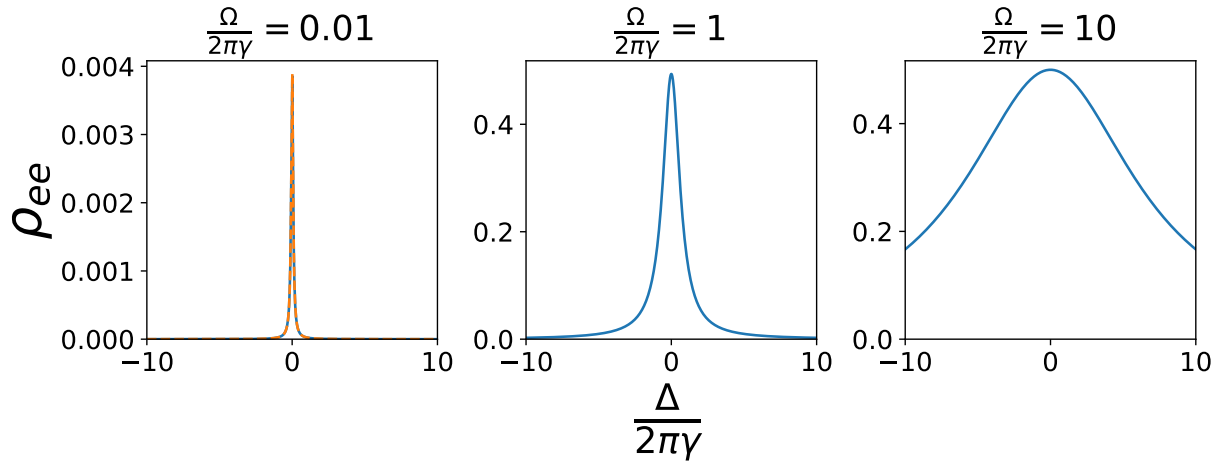
Figure 2.14: Steady-state excited state probability for a damped two level system. $\rho_{ee}^{(\text{ss})}$ is plotted in blue as a function of laser detuning from resonance for various laser driving strengths. In the left-most plot, where $|\Omega| \ll \gamma$ the lineshape has a form of the Lorentzian as described by Equation 2.134, which is plotted with an orange dashed curve.

AC Stark shift

Generally, approximating resonantly driven transitions as two level systems works quite well for predicting the dynamics of our experiments given the typical operating parameters (laser intensities, static magnetic field strengths, detunings, etc.). However, it is often necessary to include a perturbative treatment of off-resonant couplings of the nearest allowed transitions, which tend to shift the energy levels of the resonant transition [42]. This is known as the *AC Stark effect*.

The small parameter we consider is $\frac{|\Omega|/2}{\Delta} \ll 1$. When this condition holds for a particular carrier transition $|e, n\rangle \leftrightarrow |a, n\rangle$, the energy shift is given by [31]:

$$\delta E_g = \hbar \frac{|\Omega|^2}{4\Delta} \tag{2.135}$$

$$\delta E_a = -\hbar \frac{|\Omega|^2}{4\Delta} \tag{2.136}$$

where δE_g (δE_a) corresponds to the shift of the unperturbed energy of the state $|g, n\rangle$ ($|e, n\rangle$). These equations hold for both positive and negative $\Delta = \omega_L - (E_a - E_g)/\hbar$.

When a carrier transition is driven resonantly but there is also an off-resonant interaction with another far-detuned transition, only one state of the resonant transition experiences a

shift[24], as illustrated in Figure 2.15(a). However, a very common situation where the AC Stark shift must be taken into account is when a sideband transition is being driven. In this case, the detuning is relatively small and the interaction strength of the off-resonant carrier transition is stronger than the sideband transition by a factor of $1/\eta$. Moreover, both states of the sideband transition are affected by the Stark shift, so the effect is doubled. This is illustrated in Figure 2.15(b). For $\Omega = 2\pi \times 100$ KHz and a $2\pi \times 1$ MHz vibrational sideband, a resonant blue sideband transition will also experience a $2\pi \times 5$ KHz Stark shift from the off-resonant carrier interaction. Given $\eta \sim 0.06$, this shift is of the same order as the coupling to the sideband.

When driving a far-detuned transition, the AC stark shift is the dominant effect in the small parameter $|\Omega|/2\Delta$, but a small amount of population will also be driven into the off-resonantly coupled excited state. This scales as $(|\Omega|/4\Delta)^2$ and provides a limit on the strength with which sideband transitions can be driven within the two level approximation (Though, by adiabatically switching on the light, it is possible to significantly suppress these off-resonant excitations).

(a)   **(b)**
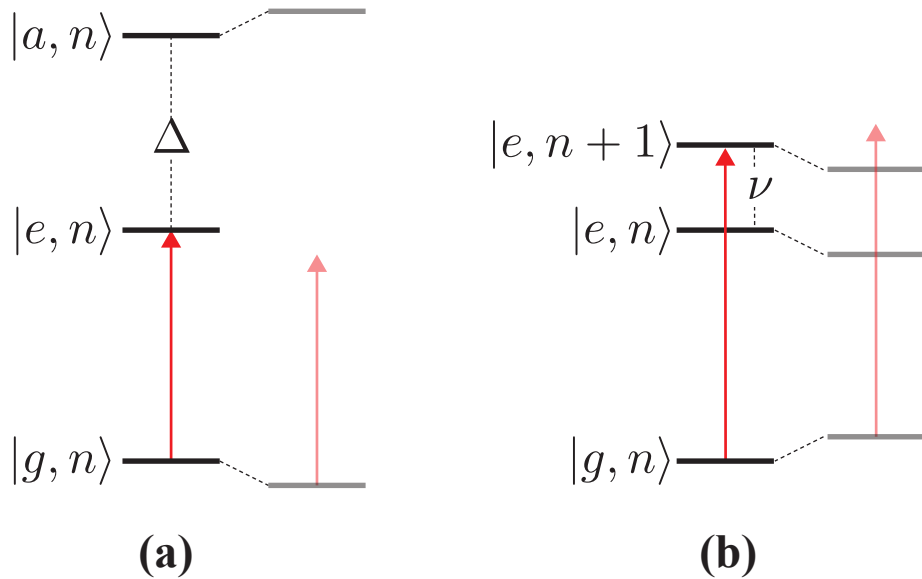
Figure 2.15: AC Stark shift due to an off-resonant carrier transition when resonantly driving a different carrier transition $|g, n\rangle \leftrightarrow |a, n\rangle$ **(a)** and a blue sideband transition $|g, n\rangle \leftrightarrow |e, n+1\rangle$ **(b)**. In the case of the blue sideband transition, both energy levels of the resonant transition are affected, so the effective shift off of resonance is doubled.

---

[24]Referencing the labels in Figure 2.15(a), this statement assumes that there either is no coupling allowed between $|e, n\rangle \leftrightarrow |a, n\rangle$ and/or the detuning of the laser from this transition is much larger.

Chapter 3

Experimental toolbox

3.1 Introduction

In this chapter, we provide a basic overview of the core techniques used for preparing, manipulating and measuring trapped ions in the experiments outlined later in this thesis. We begin in Section 3.2, by describing the two-step photoionization process used to selectively ionize the desired ^{40}Ca isotope of neutral calcium. Then, in Sections 3.3 and 3.4, we describe how we prepare ^{40}Ca^{+} ions in a well-defined quantum state with respect to both its electronic (Section 3.4) motional (Section 3.3) degrees of freedom. Next, in Sections 3.5 and 3.6, we describe how we precisely and coherently manipulate the quantum state of the ion using well-focused, narrow linewidth laser light. In particular, in Section 3.6, we describe how we can control the electric interaction between two ions, generating entanglement. Finally, in Section 3.7, we describe how we can read out the state of the ions using a technique known as electron shelving.

3.2 Photoionization
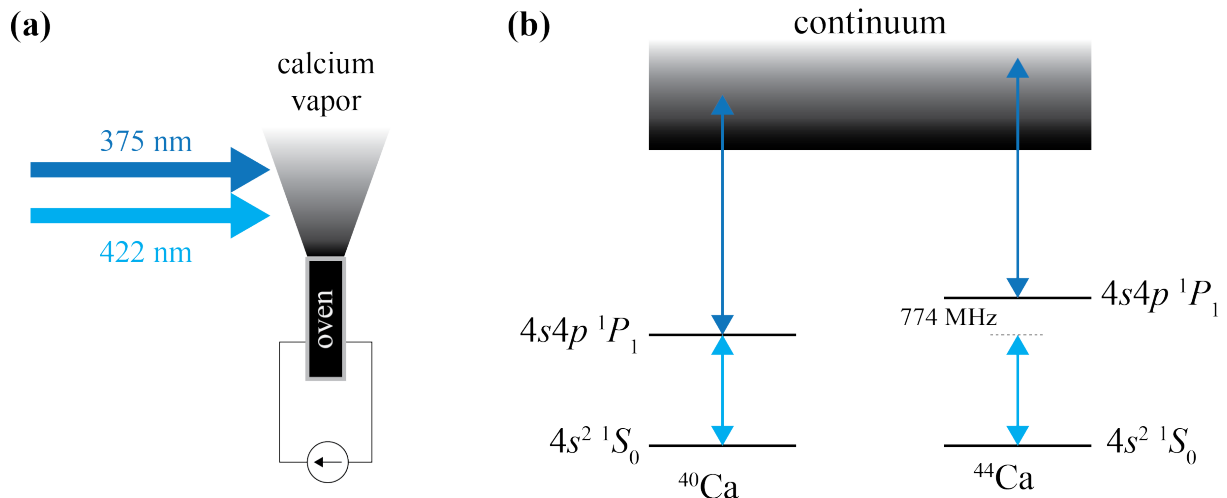
Figure 3.1: ^{40}Ca Isotope-selective photoionization scheme. **(a)** A calcium vapor is produced by resistively heating a tube filled with calcium granules (see also Chapter 4). Light at 375 and 422 nm is sent perpendicularly to this vapor stream to minimize Doppler shifts and is used to photoionize neutral ^{40}Ca atoms via the two-step process shown in **(b)**. The 422 nm light is tuned to an $S \to P$ transition that is sufficiently different amongst the various isotopes of calcium to allow for selective photoionization of ^{40}Ca. Note that the vertical axis is not to scale.

The single ionization energy of calcium is about 6 eV, which corresponds to a wavelength of around 200 nm. Light so deep in the UV tends to cause charging when incident upon dielectric materials, which makes it non-ideal for photoionization near the trapping region [43]. For this reason, we use a two-step process as illustrated in Figure 3.2(b) whereby a 422 nm photon excites the valence electron from the $^2S_0$ state to the $^1P_1$ state and then a 375 nm photon excites it into the continuum. This procedure has the additional benefit of providing isotope-selective photoionization since the typical isotope-shifts of the $^2S_0 \to^1 P_1$ are on the order of several hundred MHz [64].

Typically, the first step after setting up a new vacuum chamber/trap assembly is to "check for fluorescence." This entails generating an in-vacuum calcium vapor cloud, shining 422 nm light on it, and observing for scattered 422 nm light. In a dark room, this signal should be visible by eye and can be made more pronounced by continuously scanning the 422 nm laser light through resonance. This procedure ensures that there is non-oxidized calcium loaded in the oven, that the control lines to the oven are properly connected, and that the 422 nm light is properly aligned relative to the atomic vapor cloud (cooling lasers can then
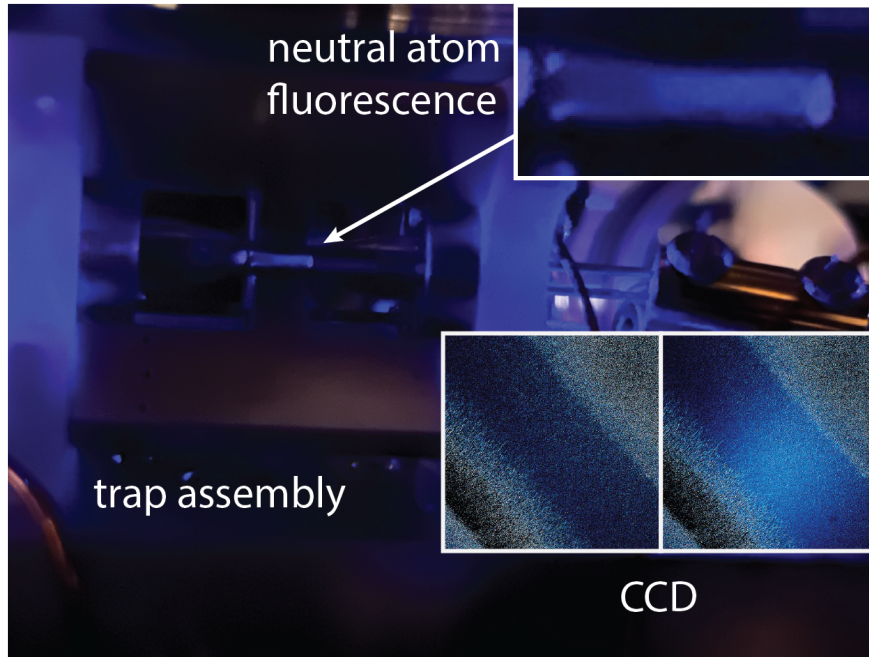
Figure 3.2: Neutral atomic calcium fluorescence. An image of neutral ^{40}Ca atoms fluorescing as 422 nm photons are scattered off of a $S \to P$ transition (see Figure 3.1). **Inset**: Images of the same fluorescence using a CCD camera. On the left, the 422 nm addressing beam is tuned off of resonance, and on the right it is on resonance.

mass number	natural abundance	$^1S_0 \leftrightarrow ^1P_1$ isotope shift
40	96.9%	0 MHz
42	0.647%	394 MHz
43	0.135%	612 MHz
44	2.09%	774 MHz
46	0.004%	1160 MHz
48	0.187%	1513 MHz

Table 3.1: Calcium natural isotope abundances and isotope shifts. Reproduced from [64].

be coaligned to this path). An image showing what the scattered signal should look like is given in Figure 3.2.

3.3 Laser cooling

We use laser cooling to prepare the ions in their motional ground states with high probability. During experimental operation, cooling is also necessary for crystallization [9] as discussed in Section 2.2 and to prevent the ions from escaping due to environmental background heating that will eventually cause their kinetic energy to exceed the trap depth [89, 73].

The principle underlying laser cooling is the fact that photons carry momentum. Thus, during a scattering event, where a photon is absorbed and then subsequently emitted by an atom, there is an exchange of momentum between the light and the atom. This interaction can be engineered to selectively reduce the momentum of the atom. If scattering is then performed on an atomic *cycling transition*, such that each spontaneous emission event returns the atom to its original state (before absorbing the photon), then the procedure can be repeated continuously, leading to an average cooling force on the atom.

For a harmonically trapped ion, with trapping frequency ν, two parameter regimes naturally arise depending on the relationship between ν and the spontaneous emission rate γ:

- $\nu \ll \gamma$: In this regime, it is sufficient to treat the ion as a free particle since the characteristic time for each scattering event $1/\Gamma$ is much less than a single vibrational period $1/\nu$. Because the absorption linewidth (Section 2.6) encompasses many discrete vibrational sidebands, this is often referred to as the *unresolved sideband regime*. Cooling relies on the Doppler effect and is achieved by red-detuning from the electronic transition. Because γ is large, cooling can be performed very quickly, but this limits the minimum achievable temperature since there is a non-negligible probability of heating the ion both during absorption and during emission.

- $\nu \gg \gamma$: The so-called *resolved sideband regime* since, here, the absorption linewidth is much smaller than the spectral spacing between adjacent vibrational sidebands. In this regime, one can selectively drive a red sideband of the electronic transition. If, in addition, the ion is in the Lamb-Dicke regime where the confinement is very strong, subsequent spontaneous emission is most likely to preserve the temperature of the ion. This procedure is referred to as *resolved sideband cooling* and is capable of driving the ion very close to its vibrational ground state, limited only by the probability of highly off-resonant blue sideband absorption (or decay). However, the requirement of small γ limits the rate at which this can be performed.

In practice, we utilize both regimes in a two-step cooling process, each involving a different electronic transition. In the first step, we Doppler cool the ions down to their fundamental limit by addressing a short-lived dipole-allowed transition. At this point, the motion of the ions is sufficiently constrained to allow for selective excitation of the red sidebands of the long-lived, dipole-forbidden $S_{1/2} \leftrightarrow D_{5/2}$ transitions. We use this feature in a technique known as resolved sideband cooling, to further pump the ion's motion down (very near) to

its vibrational ground state. In the following subsections, we will give a brief overview of the experimental implementation. More thorough treatments can be found in, for example, [30, 58, 67].

Doppler cooling

The principle underlying Doppler cooling is the Doppler effect. As illustrated in Figure 3.3, laser light with a wavevector $\mathbf{k}$ directed towards an ion that is moving with velocity $\mathbf{v}$ appears to the ion (in its own frame of reference) as if it were frequency-shifted by an amount:

$$\delta_{\text{Doppler}} = -\mathbf{k} \cdot \mathbf{v} \tag{3.1}$$

This means that the probability that this light will excite some atomic transition, via absorption of a photon, is velocity-dependent. For example, in the weak-driving limit $|\Omega| \ll |\Gamma|$ the steady-state excited state probability is given by (Equation 2.134):

$$\rho_{ee}^{(ss)} = \frac{|\Omega|^2}{\gamma^2 + 4(\omega_L - \omega_a - kv)} = \frac{|\Omega|^2}{\gamma^2 + 4(\Delta_0 - kv)} \tag{3.2}$$

where $\Delta_0 = \omega_L - \omega_a$ is the frequency detuning of the laser from the transition and where, for simplicity of the following calculations, we assume that the ion's motion is restricted to a single spatial axis that is aligned parallel to the direction of the laser beam such that
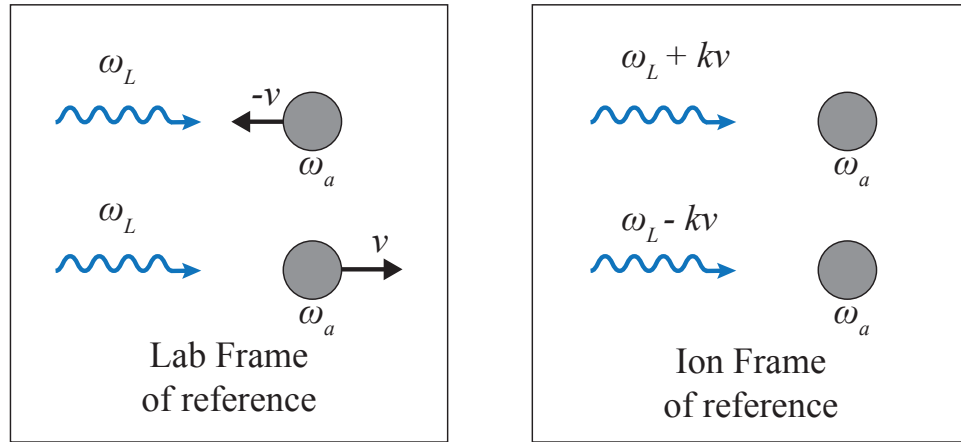
Figure 3.3: Doppler cooling. In the ion's frame of reference, the laser light is frequency-shifted by an amount $\mathbf{k} \cdot \mathbf{v}$.

$\mathbf{k} \cdot \mathbf{v} = kv$[1]. In the limit that δ_{Doppler} is much smaller than γ and Δ, we can linearize the steady state population about kv:

$$\rho_{ee}^{(ss)} \approx \left(\frac{|\Omega|^2}{\gamma^2 + 4\Delta_0^2} \right) \left(1 + \frac{8k\Delta_0}{\gamma^2 + 4\Delta_0^2} v \right) \tag{3.3}$$

Since each photon of laser light carries a momentum $\hbar k$, each absorption event causes the ion to experience an impulse $\Delta p = \hbar k$. This leads to a velocity-dependent, time-averaged force:

$$\langle F \rangle = \hbar k \gamma \langle \rho_{ee}^{(ss)} \rangle \tag{3.4}$$

and, thus, a time-averaged power:

$$\langle \dot{E}_{\text{absorption}} \rangle = \langle Fv \rangle = \hbar k \gamma \langle \rho_{ee}^{(ss)} v \rangle \tag{3.5}$$

$$= \left(\frac{|\Omega|^2}{\gamma^2 + 4\Delta_0^2} \right) \left(\frac{8k\Delta_0}{\gamma^2 + 4\Delta_0^2} \right) \langle v^2 \rangle \tag{3.6}$$

The important feature of Equation 3.6 is the fact that its sign is given by the sign of lab-frame detuning Δ_0. In particular, $\Delta_0 < 0$ implies that $\langle \dot{E}_{\text{absorption}} \rangle < 0$ meaning that there is a net flow of energy *out* of the system. This corresponds to the fact that, in this case, photons are preferentially absorbed when the ion is moving against the direction of the incident light since the Doppler effect causes these photons to appear blue-shifted.

The discreteness of the absorption process and the intrinsic randomness in the time of individual absorption events leads to a fundamental, finite variance of its momentum. This process can be modeled as a random walk in momentum space and leads to an effective heating rate [58]:

$$\langle \dot{E}_{\text{heating}}^{\text{abs}} \rangle = \frac{1}{2m} \frac{d}{dt} \langle p^2 \rangle = \frac{(\hbar k)^2}{2m} \gamma \rho_{ee}^{(ss)} \tag{3.7}$$

Likewise, the emission of photons also contributes to the diffusion of momentum:

$$\langle \dot{E}_{\text{heating}}^{\text{em}} \rangle = \frac{(\hbar k)^2}{2m} \gamma \rho_{ee}^{(ss)} \xi \tag{3.8}$$

where ξ is a geometric factor that takes into account the fact that the emission events occur in a random direction that is not restricted to the axis defined by the incident laser beam. The value of ξ depends on the radiation pattern of the transition. For a dipole transition, it has a value of $\xi = 2/5$ [58].

---

[1]The following calculations are then easily extended to the more general case if we assume the motion of the ions along each spatial axis is uncoupled. (A reasonable approximation according to Section 2.2). Note that, in practice, it is necessary to align the laser beam such that it has at least some projection on each spatial axis so that all vibrational modes of the ions can be simultaneously cooled.

Equating the power in and power out allows us to solve for the equilibrium temperature:

$$T = \frac{\hbar\gamma}{8k_B}(1+\xi)\left[\frac{\gamma}{2|\Delta_0|} + \frac{2|\Delta_0|}{\gamma}\right] \tag{3.9}$$

which is minimized when $\Delta_0 = -\gamma/2$, giving the Doppler cooling limit:

$$T_{\min} = \frac{\hbar\gamma}{4k_B}(1+\xi) \implies \langle \hat{a}^\dagger \hat{a}\rangle = \frac{\gamma}{4\nu}(1+\xi) \tag{3.10}$$

Temperature here is defined under the assumption that the state of the vibrational mode after cooling can be described by a thermal density matrix [36]:

$$\hat{\rho}_{\text{thermal}} = \frac{e^{-\hat{H}/k_B T}}{\text{Tr}(-\hat{H}/k_B T)} \tag{3.11}$$

with $\hat{H} = \hbar\nu\hat{a}^\dagger\hat{a}$.

In practice, we implement Doppler cooling by driving the $S_{1/2} \leftrightarrow P_{1/2}$ transition, which has a lifetime of about 7 ns, using 397 nm light, as illustrated in Figure 3.4. For a trap frequency of $2\pi \times 1$ MHz, this results in mean phonon occupancy of around 8 quanta. Since there is a finite probability that the $P_{1/2}$ state will decay to the $D_{3/2}$ state we also simultaneously shine 866 nm light on the ion in order to *repump* it into the cooling cycle whenever it ends up there.
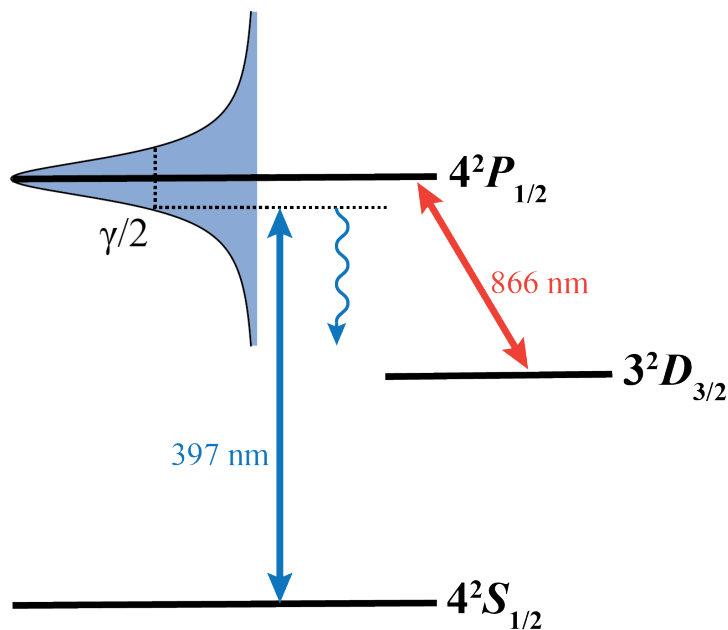
Figure 3.4: ^{40}Ca$^+$ Doppler cooling scheme. For efficient Doppler cooling, a short-lived (large γ) transition must be used. We use the 397 nm dipole-allowed $S_{1/2} \leftrightarrow P_{1/2}$ transition for this purpose. For weak driving laser intensity, the detuning is optimized at $\Delta_0 = -\gamma/2$. There is a finite probability that the $P_{1/2}$ state will decay to the $D_{3/2}$ state, taking the ion out of the cooling cycle. For this reason we also continuously drive the $D_{3/2} \leftrightarrow P_{1/2}$ transition with 866 nm *repumping* light.

Resolved-sideband cooling

When the trapping frequency ν is much larger than the spontaneous emission rate for a particular electronic transition, the vibrational sideband spectrum is well-resolved and a red-sideband transition can be selectively excited, removing a single quanta of motional energy from the ion. We use the dipole-forbidden $S_{1/2} \leftrightarrow D_{5/2}$ quadrupole transition for this purpose, which is addressed using a cavity-locked 729 nm laser. However, the lifetime of the $D_{5/2}$ state, approximately 1 second, is too large to allow for reasonably efficient cooling. For this reason, the $D_{5/2}$ state is *quenched* by illumination with a second laser with a wavelength of 854 nm that couples the $D_{5/2}$ state to the dipole-allowed $P_{3/2}$ state [67]. Since, in this configuration, the $P_{3/2}$ state is barely occupied, it can be adiabatically eliminated and its effect encapsulated by an effective linewidth for the $D_{5/2}$ state of approximately Ω^2/γ, where Ω is the coupling strength between $D_{5/2} \leftrightarrow P_{3/2}$ and γ is the spontaneous decay rate from $P_{3/2} \to S_{1/2}$. By tuning Ω a reasonable compromise can be made between maintaining a relatively small effective linewidth that preserves the resolution of the sidebands and a reasonably large cooling rate.

A cartoon illustration of the sideband cooling procedure is given in Figure 3.5. Just as with Doppler cooling, the minimum achievable temperature is fundamentally limited by the linewidth (in this case the effective linewidth) of the electronic transition. The dominant heating mechanisms are an off-resonant excitation of a blue-sideband transition with the 729 nm laser followed by a spontaneous decay event on the carrier transition and off-resonant excitation of the carrier transition followed by spontaneous decay on the blue sideband. Taking these two processes into account, the equilibrium temperature scales as [58]:

$$\langle \hat{a}^\dagger \hat{a} \rangle \propto \frac{1}{4} \left(\frac{\gamma}{\nu} \right)^2 \tag{3.12}$$

And, since we assume the resolved sideband limit where $\gamma \ll \nu$, this will be very close to the ground state of motion. For an effective linewidth $\gamma \sim 100$ kHz and a trap frequency of $\nu \sim 1$ MHz, this amounts to an equilibrium phonon occupancy of approximately 10^{-2} quanta.
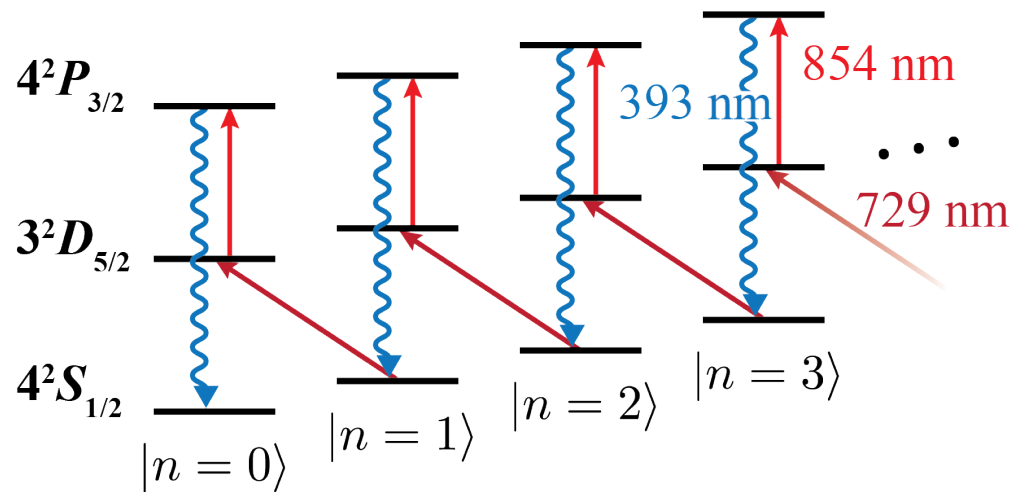
Figure 3.5: Sideband cooling scheme. (Not shown: 866 nm rempumping light).

3.4 Optical pumping

In order to prepare the ions in a well-defined electronic state, a frequency-selective optical pumping scheme is utilized [83]. As illustrated in Figure 3.6, 729 nm light is used to continuously drive population from the $|S_{1/2}, m_j = +1/2\rangle$ state to the $|D_{5/2}, m_j = -3/2\rangle$ state, while 854 nm light simultaneously pumps population out of the $D_{5/2}$ level and back into $S_{1/2}$. The $|S_{1/2}, m_j = +1/2\rangle \leftrightarrow |D_{5/2}, m_j = -3/2\rangle$ is most efficient, since there are two pathways for the ion to be pumped into the $|S_{1/2}, m_j = -1/2\rangle$ state but only one for the $|S_{1/2}, m_j = +1/2\rangle$. Just as with Doppler cooling, an 866 nm laser is used to repump the $D_{3/2}$ state.
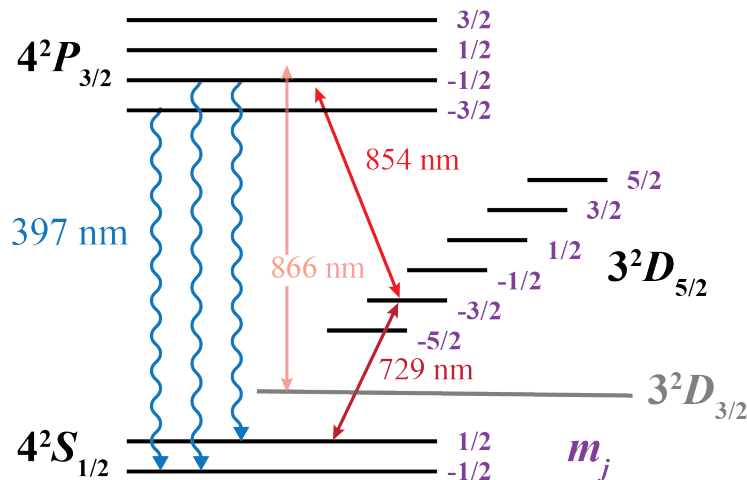
Figure 3.6: Optical pumping scheme for ^{40}Ca$^+$. For optical pumping into the $|S_{1/2}, m_j = -1/2\rangle$ state, the $|S_{1/2}, m_j = +1/2\rangle \leftrightarrow D_{5/2}, m_j = -3/2|\rangle$ quadrupole transition is the most efficient. Optical pumping into the $|S_{1/2}, m_j = +1/2\rangle$ can likewise be achieved by driving the $|S_{1/2}, m_j = -1/2\rangle \leftrightarrow D_{5/2}, m_j = +3/2|\rangle$ quadrupole transition.

3.5 Coherent single-ion control

For the experiments covered in this thesis, coherent manipulations of the electronic state of the ions are limited to Zeeman substates of the $S_{1/2}$ and $D_{5/2}$ fine structure levels of $^{40}\text{Ca}^+$. If a sufficiently narrow linewidth laser is used to address the ions[2], then a single transition can be resonantly selected and it is appropriate to model the electronic state of the ion as a two level system. The near-resonant interaction can be modeled by the Hamiltonian in Equation 2.112 from Section 2.6, which we reproduce here:

$$\hat{H}_{\text{int}} = \hbar \frac{|\Omega| e^{i\phi}}{2} e^{-i\Delta t} \hat{\sigma}_{eg} + \text{h.c.} \tag{3.13}$$

For a fixed laser geometry, $|\Omega|$ is tuned with the intensity of the laser beam, and ϕ is tuned with its phase. As before, Δ is determined by the detuning of the laser frequency ω_L from the frequency splitting of the two electronic energy levels ω_a such that $\Delta = \omega_L - \omega_a$ and $\hat{\sigma}_{eg}$ denotes the operator coupling the lower energy level to the higher energy level. For example, $\hat{\sigma}_{eg} = |D_{5/2}, m_j = 1/2\rangle\langle S_{1/2}, m_j = 1/2|$ in Figure 3.7.
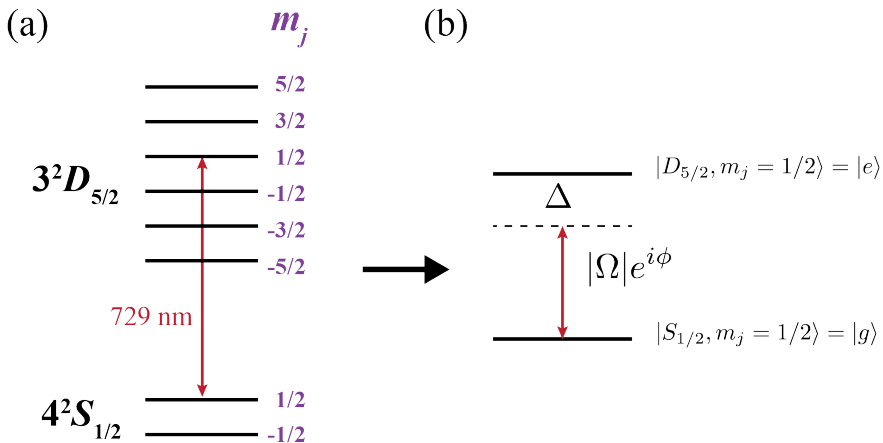
Figure 3.7: Coherent single qubit interaction.

For a resonant laser pulse, $\Delta = 0$ in Equation 3.13, if the interaction is turned on for a finite duration T, then the effect on the state of the ion, as found by solving the Schrödinger $i\hbar\partial_t|\psi\rangle = \hat{H}_{\text{int}}|\psi\rangle$, can be described by the unitary transformation:

$$|\psi(t = T)\rangle = \hat{U}(T)|\psi(t = 0)\rangle \tag{3.14}$$

where:

---

[2]Small relative to the spectral resolution of the Zeeman transitions.

$$\hat{U}(T) = e^{-i\hat{H}_{\text{int}}T/\hbar} = \begin{pmatrix} \cos(|\Omega|T) & -i\sin(|\Omega|T)e^{-i\phi} \\ -i\sin(|\Omega|T)e^{i\phi} & \cos(|\Omega|T) \end{pmatrix} \tag{3.15}$$

and:

$$|\psi(t=0)\rangle = a|g\rangle + b|e\rangle = \begin{pmatrix} a \\ b \end{pmatrix} \tag{3.16}$$

which ignores the effect of spontaneous emission out of the excited electronic state – valid when $T \ll 1/\gamma$ ($\gamma \sim 1$ second for the $D_{5/2}$ fine structure manifold).

If the ion is initialized in its ground state, then it can be transformed under $\hat{U}$ into any other possible (physically meaningful) state with an appropriate choice of laser parameters Ω and T:

$$|\psi(t=T)\rangle = \cos(\frac{\theta}{2})|g\rangle + e^{i\varphi}\sin(\frac{\theta}{2})|e\rangle \tag{3.17}$$

where we've taken $\theta/2 = |\Omega|T$ and $ie^{i\phi} = e^{i\varphi}$. The arbitrary two level state in Equation 3.17 has two free parameters[3] $\theta \in [0, \pi]$ and $\varphi \in [0, 2\pi]$ and it is customary to illustrate these as a point on the surface of a unit sphere, known in this context as the Bloch sphere [75]. In this representation, $\hat{U}(T; \Omega)$ is equivalent to rotation by an angle θ about an axis in the X-Y plane of the Bloch sphere that makes an angle of φ with the X-axis. For this reason, we will often refer to $\hat{U}$ as a rotation and denote it by $R_\varphi(\theta)$ or, for convenience, $R_X(\theta)$, $R_Y(\theta)$ when the axis of rotation is equal to X or Y, respectively [75] (see Figure 3.8). If the ion is initialized to the ground state $|g\rangle$, as is generally the case at the beginning of any experiment, then the absolute value of the laser phase ϕ is irrelevant (that is, we have freedom in deciding where the X and Y axes lie in the X-Y plane of the Bloch sphere). However, the relative laser phase of subsequent interactions will matter and this can be controlled by the phase of the RF applied to the acousto-optic modulator used to modulate the laser light parameters provided that the laser light phase remains stable (the coherence time of the laser is on the order of several ms)[4].

So far in this section, we have ignored the vibrational state of the ion. The previous results hold provided the vibrational mode is in a well-defined Fock state[5] $|n\rangle$, $n \in \mathbb{N}$. Under this condition, the preceding results can also be extended to laser interactions that drive vibrational sideband transitions, as discussed in Section 2.6, provided we make the replacements $|g\rangle \to |g\rangle \otimes |n\rangle$, $|g\rangle \to |e\rangle \otimes |m\rangle$ and $\Omega \to \Omega_{mn}$ (as defined in Equation 2.117).

---

[3]This is consistent with Equation 3.16, even though $a, b \in \mathbb{C}$ has 4 degrees of freedom, since conservation of probability ($\langle\psi|\psi\rangle = 1$) and the insignificance of the global phase ($|\phi\rangle$ and $e^{i\alpha}|\phi\rangle$ cannot be distinguished by measurement) remove two of them.

[4]See Chapter 4 for more details.

[5]This is true when the laser is pointed in a direction aligned with one of the ion's vibrational axes, say $\hat{z}$ such that for the laser's k-vector $\hat{k} \cdot \hat{z} = 1$, which we will assume in the remainder of this section. More generally, this is true when all three vibrational modes of the ion are individually in well-defined Fock states.
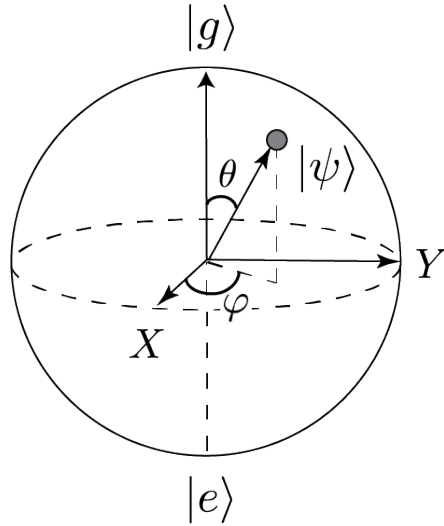
Figure 3.8: Bloch sphere. An arbitrary state $|\psi\rangle = \cos(\frac{\theta}{2})|g\rangle + e^{i\varphi}\sin(\frac{\theta}{2})|e\rangle$ of the two-level system $\{|g\rangle, |e\rangle\}$ is parameterized by the two variables θ and φ, which can be visualized as a point on the unit sphere. If the system is initialized in the state $|g\rangle$, then $|\psi\rangle$ can be obtained by applying the rotation $R_\varphi(\theta)$. More generally, $R_\varphi(\theta)$ can be used to transform an arbitrary state of the two level system to any other state with the appropriate choice of the parameters parameters θ and φ.

If the vibrational mode participating in the laser interaction is not initialized into a Fock state, then the two level approximation is no longer generally valid – leading to nontrivial effects. For example, if an ion is initialized into the state $|g\rangle \otimes |0\rangle$ and allowed to evolve under the resonant action of the Hamiltonian in Equation 3.13 this will result in sinusoidal oscillations between the ion's electronic states $|g\rangle$ and $|e\rangle$ at a frequency of $|\Omega|$:

$$P(|e\rangle)(t) = \sin^2(|\Omega|t) \tag{3.18}$$

These oscillations are typically referred to as *Rabi oscillations* and, in this context, $|\Omega|$ is referred to as the Rabi frequency. However if, instead, the ion is initialized into the electronic ground state $|g\rangle$ but the motional state begins in, say, a thermal state (Equation 3.11), then the laser will effectively drive multiple transitions, each with a slightly different Rabi frequency, as illustrated in Figure 3.9. In this case, the functional form of the time-evolution in Equation 3.18 is replaced by the weighted sum:

$$P(|e\rangle) = \sum_n p(n)\sin^2(|\Omega_{nn}|t) \tag{3.19}$$

where, to leading order, $|\Omega_{nn}| = |\Omega|(1 - \eta^2 n)$ (see Equation 2.120). This effect can be used to experimentally reconstruct the Fock state distribution $p(n)$, though, at least in the Lamb Dicke regime, it is more practical to use a sideband interaction for this purpose [55], since the leading order dependency on n is linear in η for sideband transitions. This is one method for estimating the temperature of the vibrational mode and, thus, the quality of the initial laser cooling.
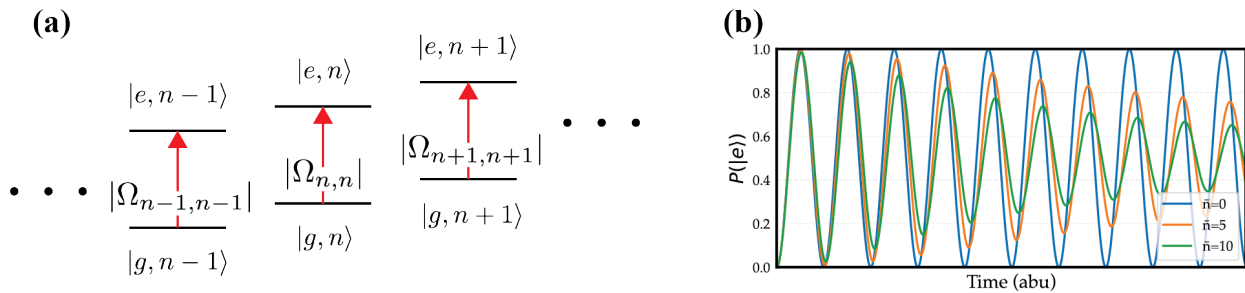
Figure 3.9: Hot Rabi oscillations. When the ion is initialized in the electronic ground state $|g\rangle$ but the vibrational mode is initialized in a thermal state the two level approximation is no longer valid for the dynamics under the interaction defined by $\hat{H}_{\text{int}}$ in Equation 3.13. In this case, there are multiple pathways to excite the ion into the electronic state $|e\rangle$ as illustrated in **(a)**. The probability of finding the ion in $|e\rangle$ at a particular point in time is then given by the weighted average in Equation 3.19, as illustrated in **(b)** for various thermal states characterized by the mean phonon occupation $\bar{n}$

3.6   Entanglement

Two quantum systems A and B are said to be entangled when they exhibit a correlated state described by a wavefunction that cannot be factorized into a product state of the form [75]

$$|\Psi\rangle = |\psi\rangle_A \otimes |\psi\rangle_B \tag{3.20}$$

For example, if we consider two identical ions A and B each containing a pair of electronic energy levels $|g\rangle$ and $|e\rangle$, then one such possible entangled state, known as a Bell state [75], is given by:

$$|\Psi\rangle = (|g\rangle_A|g\rangle_B + e^{i\phi}|e\rangle_A|e\rangle_B)/\sqrt{2} \tag{3.21}$$

which is maximally entangled in the sense that knowledge of the state of one of the ions yields full knowledge of the state of the other. Entangled states represent an intrinsically quantum phenomenon since the degree of correlation that they exhibit surpasses what can be achieved according to the laws of classical physics [5]. Much of the proposed advantage of quantum information processing devices over classical devices derives from this fact. In Chapter 6, we will utilize engineered states of the form in Equation 3.21 to improve the signal-to-noise ratio of a precise measurement of Lorentz invariance beyond what can be accomplished with two classically correlated ions.

At a minimum, generating a state as in Equation 3.21 requires a physical interaction between ions A and B[6]. It is difficult to generate this interaction directly between the internal states of the ions due to the disparity between the scale of the local atomic charge distribution (on the order of Angstroms) and the typical separation between the ions in a linear Coulomb crystal (on the order of microns).

On the other hand, the mutual Coulomb repulsion discussed in Section 2.2 does equate to a strong, always-on coupling between the individual center of mass motion of co-trapped ions. This coupling can be used to generate entanglement between the electronic states of a single ion and the collective, normal mode motion of a chain of ions by driving a sideband transition. Moreover, if this normal mode is first cooled down to its ground state, then this interaction can be conditioned on the electronic state of the laser-addressed ion. For example, a laser pulse tuned to the blue (red) sideband will only drive an electronic transition if the ion is in its electronic ground (excited) state. This feature can be leveraged to design a piecemeal pulse sequence that first entangles the electronic state of a single ion with the collective motion of the chain and then transfers the information encoded in the motion to the electronic state of another ion [20]. In this way, the collective motion of the ions acts as

---

[6]Actually, this is not quite true. For example, it is possible to entangle two ions by performing correlated measurements of two photons, one spontaneously emitted by each ion and each of which whose polarization is entangled with the electronic state of their respective ions [70]. In this case, the two ions can be entangled in the absence of any direct physical interaction.

a sort of quantum bus, communicating information about the electronic state of one ion to another.

As first pointed out by Mølmer and Sørensen [72], a similar strategy as outlined above can be applied more straightforwardly by simultaneously illuminating two ions with a light field consisting of two distinct tones. The key is to choose the frequencies of the two tones such that they have an equal, but opposite, detuning from a shared vibrational mode[7] of the two ions. This scenario is illustrated in Figure 3.10 (a). In this case, an energy-conserving two-photon transition between the electronic states $|g\rangle_A|g\rangle_B \leftrightarrow |e\rangle_A|e\rangle_B$ becomes possible. Four such transitions are simultaneously activated. As shown in [72] (b), these transitions interfere with one another in such a way that, to first order, the interaction becomes independent of the precise vibrational state of the ions – provided that the Lamb Dicke approximation is still valid. The resulting Hamiltonian is:

$$\hat{H} = \hbar\chi\hat{\sigma}_x^{(A)} \otimes \hat{\sigma}_x^{(B)} \tag{3.22}$$

where:

$$\chi \approx \eta^2\Omega^2/\delta \tag{3.23}$$

with η the Lamb-Dicke parameter of the participating vibrational mode and Ω proportional to the electric field amplitude of the light field. $\hat{H}$ results in Rabi-like oscillations between the two-level electronic subspace $\{|g\rangle_A|g\rangle_B, |e\rangle_A|g\rangle_B\}$ of the ions. And if the interaction is turned on precisely for the duration $t = \pi/2\chi$, then a maximally entangled state of the form in Equation 3.21 is produced, where the phase ϕ can be controlled through the global phase of the bichromatic light field.

To obtain the approximate Hamiltonian in Equation 3.22, it is assumed that the detuning δ from the sidebands is much greater than the direct (single-photon) coupling to these states:

$$\delta \gg \eta\Omega. \tag{3.24}$$

This ensures that the intermediate states of the transition, like $|g\rangle_A|e\rangle_B$, are not off-resonantly populated during the interaction. For a fixed laser, this sets a practical limitation on the strength of the entangling interaction. More generally, off-resonant coupling to higher-order sidebands, other vibrational modes or other electronic states will also limit the maximum detuning. However, if the goal is just to generate a maximally entangled Bell state, then the condition in Equation 3.24 can be relaxed, as described in detail in [93]. The rough idea is to tune the parameters of the interaction such that off-resonantly excited states are depopulated at precisely the same moment that the desired states are maximally correlated, known as the gate time. This is illustrated in Figure 3.11 (a).

The probability that a state $|\Psi\rangle$ of the form in Equation 3.21 is generated by the Mølmer-Sørensen gate is given by:

---

[7]Whose motion, in the simplest case, involves equal participation of both ions, which will always be the case for a pair of co-trapped ions with equal mass.
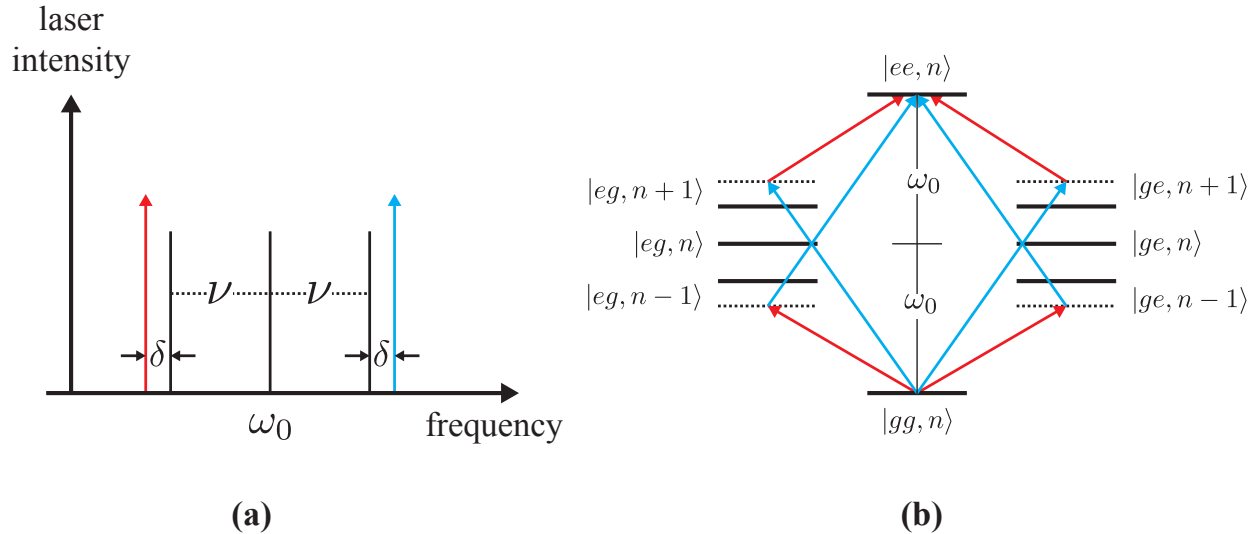
Figure 3.10: Mølmer-Sørensen interaction. **(a)** Frequency spectrum of the bichromatic light-field used for the Mølmer-Sørensen interaction. ω_0 corresponds to the frequency splitting between the individual electronic states of the ions $|g\rangle$ and $|e\rangle$ and ν corresponds to the frequency of the participating vibrational mode. **(b)** An illustration of the four interfering, two-photon transition pathways corresponding to the two-photon resonance condition $\omega_r + \omega_b = 2\omega_0$, where ω_r, ω_b correspond to the two tones of the bichromatic light-field.

$$\langle\Psi|\rho|\Psi\rangle = \frac{1}{2}(\rho_{ee} + \rho_{gg}) + |\rho_{eg}| \tag{3.25}$$

which we will refer to as the fidelity of the gate operation. Here ρ is the density matrix representing the physical state resulting from an experimental application of the gate. The first two terms on the right-hand side of Equation 3.25 correspond to the probability of finding the ions in the joint states $|e\rangle_A|e\rangle_B$ or $|g\rangle_A|g\rangle_B$, respectively, at the conclusion of the gate. These probabilities can be measured directly via the electron shelving method described in Section 3.7. The third term represents the amplitudes of the off-diagonal elements of the density matrix $\langle ee|\rho|gg\rangle = \langle ee|\rho|gg\rangle^*$. This can be measured by simultaneously applying a single-ion $\pi/2$-pulse to both ions, referred to as an analysis pulse, with a laser phase of φ relative to the global laser pulse of the bichromatic field, followed by measurement in the standard basis [86, 6]. The resulting parity signal Π, equal to the sum of the probability of finding both ions in the same electronic state minus the sum of the probabilities of finding them in opposite states, will oscillate sinusoidally as a function of the phase φ as $\Pi = A\sin(2\varphi + \phi)$. The amplitude of these oscillations $A/2$ is equal to the amplitude of the coherence $|\rho_{eg}|$. An experimental example of a parity oscillation is shown in Figure 3.11 (b).

(a)

(b)
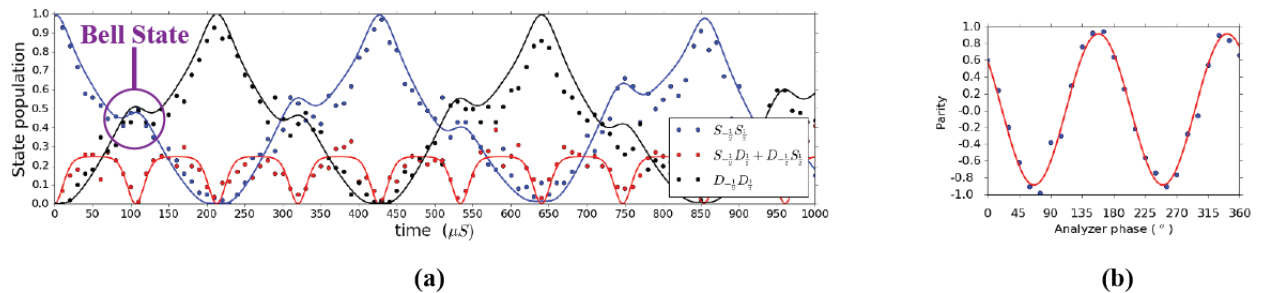
Figure 3.11: Mølmer-Sørensen Gate. **(a)** Example population dynamics for a strongly-driven Mølmer-Sørensen interaction. The states labeled D and S correspond to the states $|e\rangle$ and $|g\rangle$ (respectively) discussed in the main text. The point in time when the maximally entangled Bell state is generated, typically referred to as the gate time, is circled in purple. Note that, at this point the intermediate state populations, colored in red, are fully depopulated. The circles label experimental data and the solid lines label simulation. **(b)** An example of a parity oscillation. The analyzer phase corresponds to the phase of the global analysis pulse. Circles correspond to experimental data and the red curve corresponds to a sinusoidal fit. Along with the data in (a), the fidelity of the Bell state produced at the first gate time was found to be approximately 94%.

3.7   Measurement

To measure the ions, we scatter light off of the 397 nm $S_{1/2} \leftrightarrow P_{1/2}$ cycling transition, which is then focused and directed onto either a photomultiplier tube (PMT) or an EMCCD camera (see Section 4.5 for technical details). An example image taken using the camera is shown in Figure 3.13.

Using the electron shelving method [58], we are able to determine whether the ion is in the $D_{5/2}$ level. The method is illustrated in Figure 3.12. When the ion is in the $S_{1/2}$ level, incident 397 nm light will continuously scatter photons. On the other hand, if it is in the $D_{5/2}$ level, the ion will be transparent to this light. For a sufficiently long readout duration and low background light, the two count distributions, bright and dark, can be reliably distinguished with an appropriate threshold value.
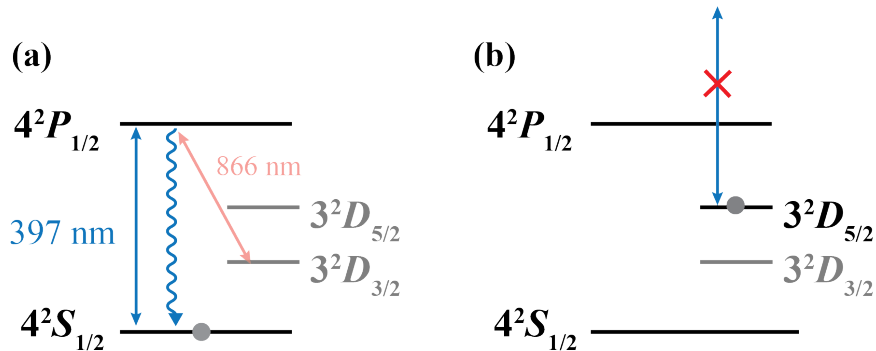
Figure 3.12: Electron shelving method. **(a)** When the ion is in the $S_{1/2}$ level, incident 397 nm light will continuously scatter photons. **(b)** When the ion is in the $D_{5/2}$ level, it is transparent to this light.
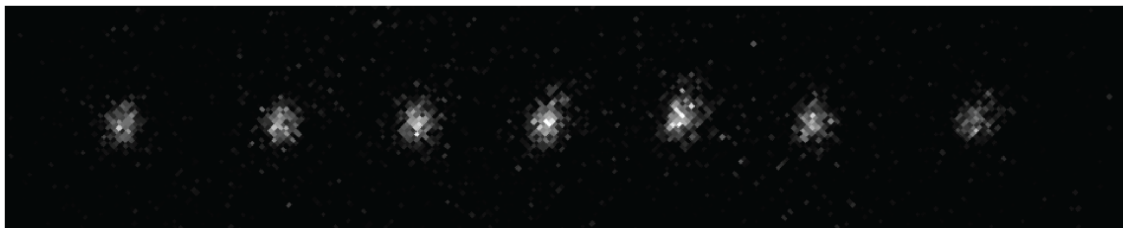
Figure 3.13: Chain of ions imaged on an EMCCD camera.

Chapter 4

Experimental setup

4.1 Introduction
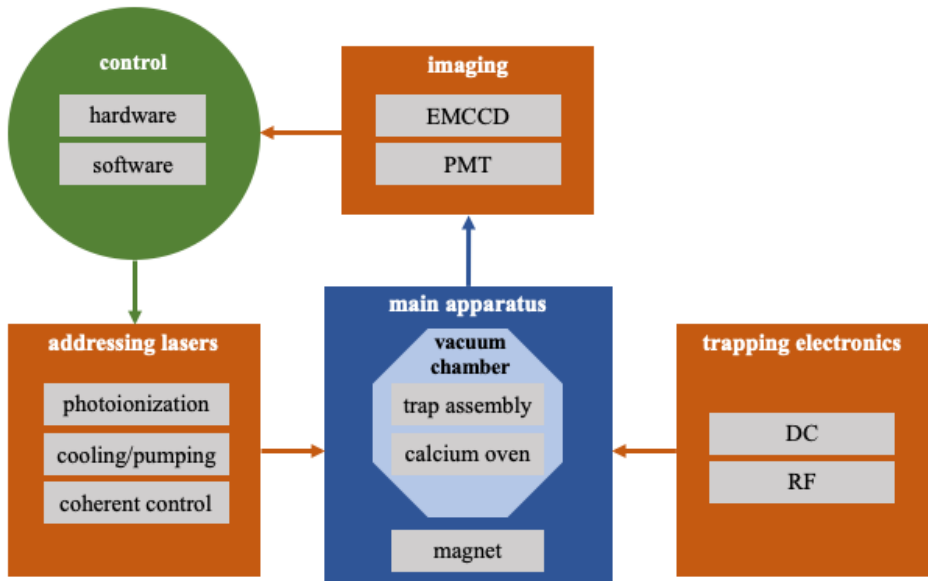
Figure 4.1: Main components of the experimental setup.

In this chapter, we sketch the physical apparatus used for trapping and controlling ions and performing the experiments in this thesis. An outline of the basic components is sketched in Figure 4.1. The main apparatus consists of the trap assembly used for generating the electric fields necessary to trap the ions, an oven used for sourcing neutral calcium atoms and a magnet for setting the quantization axis. All of this is housed in an chamber held at extreme high vacuum.

A set of laser beamss is used to photo-ionize the neutral calcium and manipulate the internal state of the ions. Measurement of the ion's state is performed using either an EMCCD camera or a PMT. All control is facilitated through a hardware/software stack with both real-time and asynchronous capabilities.

4.2 Main apparatus
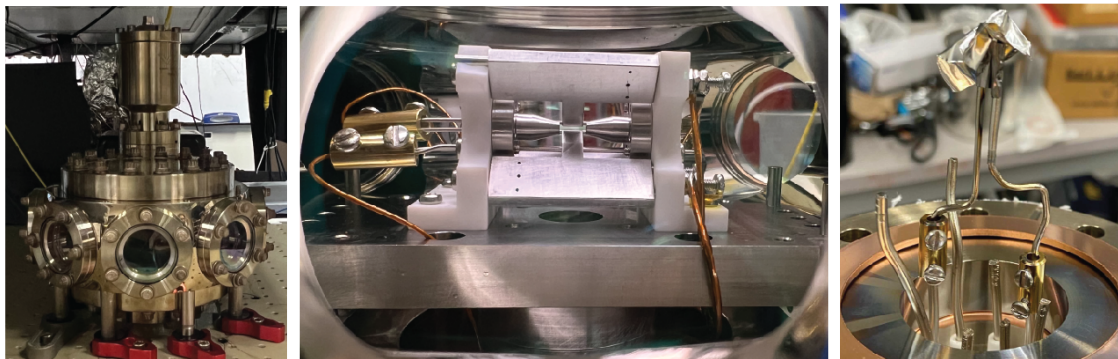
Figure 4.2: From left to right, the vacuum chamber, trap assembly and calcium oven used for the experiments in this thesis. The internal pressure of the chamber is kept at $\sim 10^{-11}$ mbar. Contained inside is the trap assembly and a calcium oven, which sources the calcium atoms.

The trap assembly and vacuum chamber used for the experiments described in this thesis were designed and built by Thaned Pruttivarasin and Michael Ramm. A more detailed description[1] can be found in their theses [81, 82]. Here we provide a summary of the features relevant for this thesis.

Trap assembly

A diagram of the trap assembly is provided in Figure 4.3. The DC electrodes, or "end caps," are held at a static potential to trap the ions in the axial direction. The RF electrodes, or "RF blades," are driven with an oscillating voltage that generates the pseudopotential for trapping in the radial plane. Two coupled pairs of compensation electrodes allow compensation of any stray electric fields in the radial plane, which would otherwise induce excess micromotion. All electrodes are electrically connected to external sources using 1 mm thick,

---

[1]Specifically, the "improved" design described in [82].
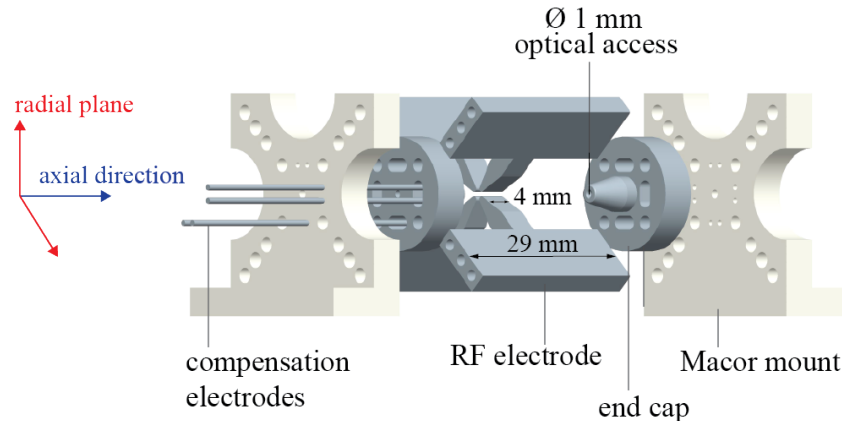
Figure 4.3: Trap assembly. Trap electrodes (gray) are composed of electropolished 316L stainless steel and supported on a Macor frame (beige). The DC electrodes have a 1 mm pinhole with rounded edges, which allows for optical access along the axis of the trap. The tips of the DC electrodes have a diameter of 5 mm. The tip-to-tip distance between endcaps is 5 mm and the gap between diametrically opposing RF electrodes is 1 mm. Image adapted from [82].

vacuum-compatible, Kapton-insulated copper wire. And all electrodes are capable of supporting at least several kilovolts while under vacuum [82]. Pinholes through the end caps provide optical access along the axial direction. The electrodes are supported by an vacuum-compatible, insulating Macor frame that is rated for continuous operation at temperatures of up to 800°C. The physical realization of the trap assembly is shown in the middle image of Figure 4.2.

Calcium oven

A calcium oven is used to source the atoms for experiments. It consists of a stainless steel tube, open-ended on one side and loosely packed with calcium granules. The tube is wrapped with a strip of tantalum foil connected by conductive wire to an external current source. When a sufficiently high current[2] is driven through this wire, the oven assembly is resistively heated to a high enough temperature to sublimate the calcium, which is then sprayed out of the open end. The oven is mounted below the trap assembly such that

---

[2]For trapping single ions, we typically run about 4 A through the oven, but during troubleshooting have gone as high as 12 A. At about, 10 A the oven begins to glow.

the direction of the calcium plume is directed vertically upwards. The trap assembly was originally designed for an experiment with an optical cavity and special precautions were taken to prevent the calcium spray from coating the mirrors. In particular, the plume is only able to reach the trapping region through a small 12 mm diameter hole in the base mount. We found that mounting a laser to the oven was helpful for alignment with this through-hole, which can otherwise be tedious. The actual oven used is shown in the right image of Figure 4.2. The open end of the oven tube is obscured by foil, but the tantalum strip is visible just below this.

Vacuum chamber
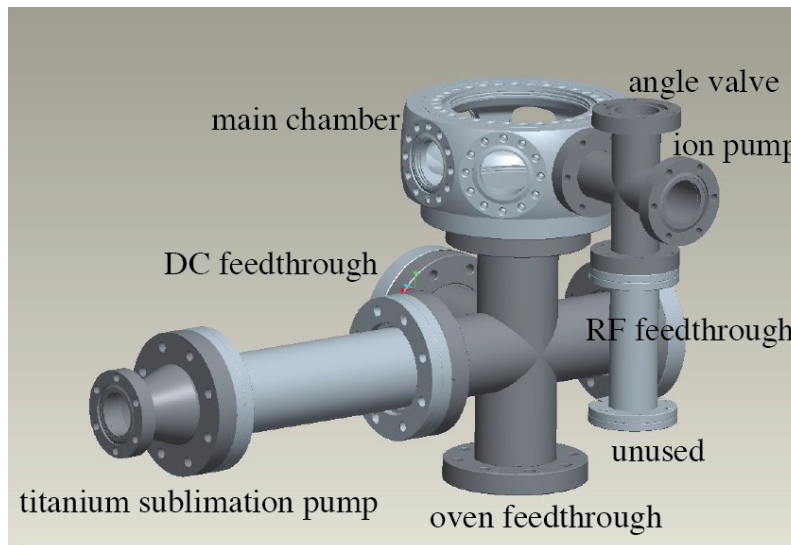
Figure 4.4: Diagram of the vacuum chamber. The labels correspond to the flanges where the corresponding component is mounted when the chamber is fully assembled. Image adapted from [82].

Both the trap assembly and oven are housed inside the main chamber of the vacuum assembly illustrated in Figure 4.4. The main chamber[3] is a spherical octagon with eight ports, allowing for optical through-access along four separate directions. When mounted, the axis of the trap is oriented along one of these directions. Separate RF and DC feedthroughs enable electrical connections to be made between the trapping electrodes and external voltage sources. The oven feedthrough provides the same function for an external current source. The angle valve is used to smoothly break vacuum and allows a simple connection to be made

---

[3]KPI MCF600-SO2000800

with, for example, an external turbo pump. When fired, the titanium sublimation pump deposits a thin layer of highly reactive titanium onto the interior surface of the chamber, which acts as a getter, and reduces the internal pressure (if the surface is not already saturated). We continuously run an ion pump while under vacuum, which is the main mechanism for maintaining (and typically improving) the quality of the vacuum over time. It also provides a limited ability to monitor the internal pressure, since this is related to the current through the pump. But field emission saturates this signal at about 10^{-9} mbar.

The average time that an ion can be contained within the trap is referred to as the trap's lifetime. If the ion is continuously laser-cooled, the lifetime is primarily determined by the internal pressure of the chamber (for a given trap depth). In our setup, pressures on the order of 10^{-11} mbar, resulted in lifetimes on the order of at least a week (typically, the cooling lasers would become unstable before the ion was lost). Starting with an opened chamber, we achieved this pressure with the following procedure:

1. With a turbomolecular pump connected through the angle valve, pump down the pressure to about 10^{-8} mbar, as measured by a residual gas analyzer (RGA).

2. If this is successful, confirm the quality of the chamber's seal by spraying helium gas around the exterior while simultaneously monitoring the partial pressure with the RGA.

3. If no leaks are detected, place the chamber in a convective oven, set so that the temperature slowly ramps over several hours to about 180°C (this accounts for differences in the thermal expansion coefficients of the various materials).

4. Maintain this temperature while continuing to pump down with the turbo until an adequate pressure is reached (typically on the order of several days to several weeks, depending on the cleanliness of the interior surface). At these temperatures pressures of around 10^{-8} mbar are reasonable.

5. Slowly ramp down the temperature, close the angle valve and remove the turbo pump.

6. Fire the titanium sublimation a few times, which should lower the pressure another order of magnitude or so (this effect is rather immediate).

7. Activate the ion pump.

Fortunately, this procedure only needed to be performed once for the experiments in this thesis. The final pressure was estimated to be on the order of 10^{-11} mbar.

Magnetic field

We apply a magnetic field to the calcium ions to resolve the Zeeman levels and set their quantization axis. We generate this using a collection of Sm_2Co_17 magnets placed inside

of 3D-printed holders designed by Nicole Greene and shown in Figure 4.5. The magnitude and direction of the field are controlled by adjusting the number of layers of magnets in the various holders. Typically, we worked with a magnetic field of around 4 Gauss.
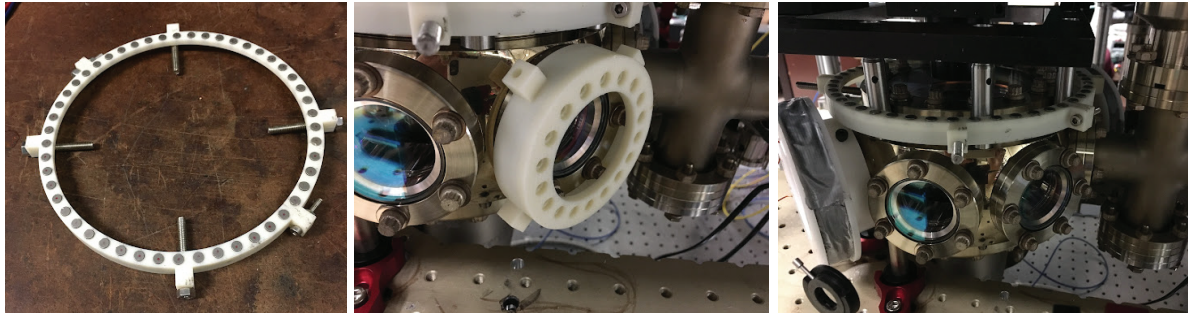
Figure 4.5: Magnets and holders. In the working configuration, two pairs of these are used. One pair each for both the horizontal and vertical directions, placed on opposite sides of the chamber. Pictures were taken by Nicole Greene.

4.3 Trapping electronics

To generate a suitable confining potential for the ions, the trap electrodes are driven with a collection of DC and RF voltage signals with magnitudes on the order of 0.1-1 kV. Connections to the external sources are made through the various chamber feedthroughs, which are internally connected to the electrodes via copper wire. In the following section, we describe the basic setup. Note that whenever a common point is indicated in a circuit diagram, it refers to a single-star ground, which is an electrically isolated copper sheet. Any circuit elements not explicitly referenced to this ground are assumed to be floating. This design is meant to prevent ground loops.

DC electronics

The voltages on the end caps and compensation electrodes are sourced by iseg SHQ222M low-noise, high-voltage power supplies. Both end caps are held at about +800 V, corresponding to a single-ion axial trapping frequency of around 1 MHz. The voltages on the micromotion compensation electrodes have to be adjusted every so often but rarely need to be set to a magnitude higher than several hundred volts. The signal from the isegs is

routed into the chamber through a low-pass, PCB filter board mounted directly to the DC feedthrough labeled in Figure 4.4. Each low-pass filter consists of a simple, two-pole RC design with cutoff frequencies of around 1 kHz.
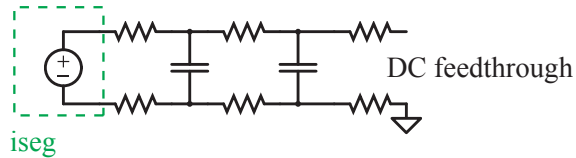
Figure 4.6: Low pass filter for DC electrodes.

RF electronics

To create the pseudopotential in the radial plane, the RF electrodes are driven with an oscillating voltage with a frequency of around $\Omega \sim 2\pi \times 30$ MHz and an amplitude of $V_{\text{p-p}} \sim 300$ V. This signal is generated by a Rhode & Schwarz SMB100A connected in series with a low-noise Mini Circuits ZHL-20W-13 RF amplifier. The output impedance of the amplifier is $Z_o = 50$ ohms, whereas the electrodes are essentially capacitors with a total capacitance of $C_{\text{trap}} \approx 30$ pF. It is impractical to drive any purely reactive load Z_l from a source with real output impedance since all of the power is reflected back to and dissipated in the source:

$$|P_{\text{reflected}}| = \left| \frac{Z_l - Z_o}{Z_l + Z_o} \right|^2 \tag{4.1}$$

To convert the input impedance of the trap into a real value, we combine an inductor, of inductance L, in parallel with the trap capacitance to form the resonator illustrated in Figure 4.7(a). The inductor is constructed by wrapping several loops of copper wire around a low-loss, iron-powder, toroidal core[4]. If the series resistance R is small, then the resonance frequency ω will occur when the reactance of the inductor is approximately equal to the reactance of the trap capacitance:

$$\omega L = \frac{1}{\omega C_{\text{trap}}} \implies \omega = \frac{1}{\sqrt{LC_{\text{trap}}}} \tag{4.2}$$

In this case, an impulse of current sent into the circuit will oscillate back and forth between the inductor and capacitor until its energy is finally dissipated on the resistor. On resonance, the input impedance is purely real as desired:

---

[4]Amidon, material 6.
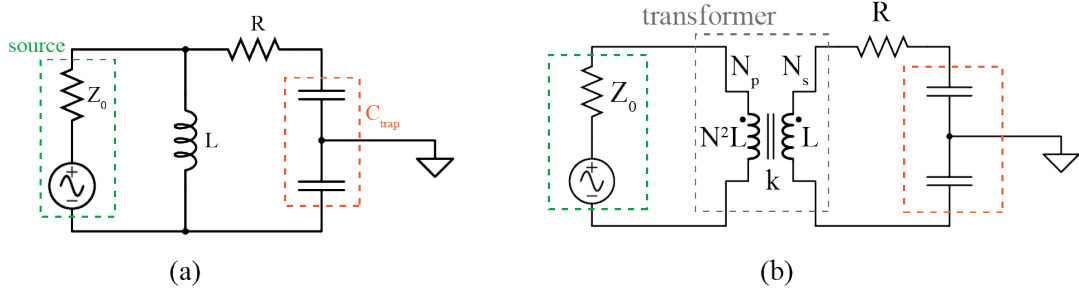
Figure 4.7: Impedance matching circuit. **(a)** The resonant circuit is used to convert the trap capacitance to a real impedance. Each trap electrode contributes about 15 uF of capacitance for a total of $C_{trap} \sim 30$ pF. Based on this value, the inductor is then chosen to achieve the desired resonance frequency of approximately 30 MHz. The main contribution to the non-ideal series resistance R tends to be due to the inductor (core loss and skin effect). **(b)** By coupling into the resonator through a transformer, the magnitude of the real input impedance of the resonator can be matched to Z_0. Here $N = N_p/N_s$ is the ratio of primary to secondary turns for the transformer. k is a dimensionless coupling constant, such that the mutual inductance of the transformer is $M = kL$. We assume this to be ≈ 1 for the analysis in the main text. In practice, k can be determined with the equation $k = \sqrt{1 - \frac{L'_p}{L_p}}$ where L'_p is the inductance of the primary coil with the secondary short-circuited and L_p is its inductance with the secondary open [3, 21]. The effect of a non-unity k on the transformer circuit is described in detail in [3].

$$Z_{\mathrm{in}}^{\mathrm{resonator}} = \frac{L}{C_{\mathrm{trap}}R} \qquad (4.3)$$

However, choosing L such that $\omega^{\mathrm{res}} = \Omega$, means that $Z_{\mathrm{in}}^{\mathrm{resonator}}$ will be on the order of tens of kohms (for $C_{\mathrm{trap}} \sim 30$ pF). So, according to Equation 4.1, most of the power will still be reflected back into the source. For this reason, rather than drive the resonator directly, we inductively couple into it through a step-up transformer as shown in Figure 4.7(b). The transformer is constructed by wrapping another wire a different number of times around the same ferrite core. According to the normal rule for transformers, the input impedance is determined by the ratio of turns N as:

$$Z_{in}^{\text{transformer}} = \underbrace{\left(\frac{N_p}{N_s} \right)}_{N}^{2} Z_{in}^{\text{resonator}} \tag{4.4}$$

Now we can achieve the desired input impedance $Z_{in}^{\text{transformer}} = Z_0$ by setting the ratio of turns as:

$$N = \sqrt{\frac{Z_0}{Z_{in}^{\text{resonator}}}} = \sqrt{\frac{Z_0 R C_{\text{trap}}}{L}} \tag{4.5}$$

Equation 4.4 is equivalent to saying that there is a voltage gain over the transformer of:

$$G_v = \frac{V_s}{V_p} = \frac{Z_{in}^{\text{resonator}}}{Z_0} = \sqrt{\frac{L/C}{R Z_0}} \tag{4.6}$$

Alternatively, this can be written in terms of the quality factor of the resonator $Q = \omega/\delta\omega$:

$$G_v = \sqrt{\frac{Q\sqrt{L/C}}{Z_0}} \tag{4.7}$$

From which it is clear that to maximize the G_v, one should also maximize Q. For $R \sim 1\Omega$, we achieve a voltage gain of $G_v \sim 20$, while also matching the input impedance of the trap electrodes to the source.

Based on the design principles just discussed, we use the following procedure to build the full impedance matching circuit. First, we build a resonator with the appropriate frequency while also optimizing the quality factor. The parameters involved are the core/wire materials and coil geometry. Then, we add the primary coil to the core, starting with a low number of turns and then working up while optimizing on the transmitted power[5] and coupling. Note that it is important not to try and optimize the quality factor this way. For a properly matched circuit, this will only be half of the maximum value since, in this case, half of the power is being dissipated by the source. This last point is illustrated in Figure 4.9.

The actual impedance matching circuit used in experiments, includes several additional elements, as illustrated in Figure 4.8 and described in the caption.

---

[5]Typically, we determine this by driving the circuit through a directional coupler and measuring the reflected power
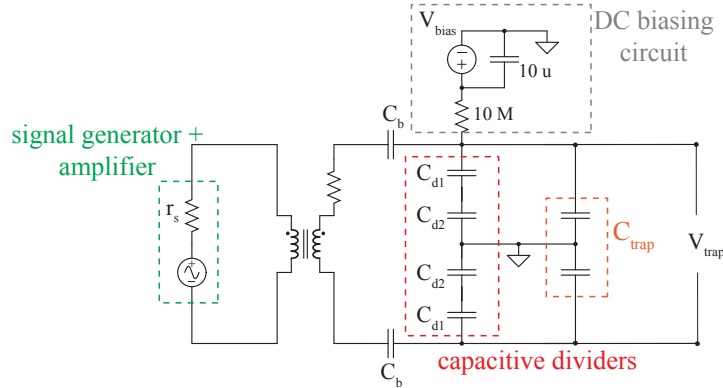
Figure 4.8: Additional components. The blocking capacitors C_b and bias voltage circuit allow us to generate a DC quadrupole potential in the radial plane. The blocking capacitors are chosen such that $C_b \ll C_{\text{trap}}$. The capacitive dividers C_d's, allow us to monitor V_{trap}. C_{d1} is chosen such that $C_{d1} \ll C_{\text{trap}}$ to avoid loading the circuit.
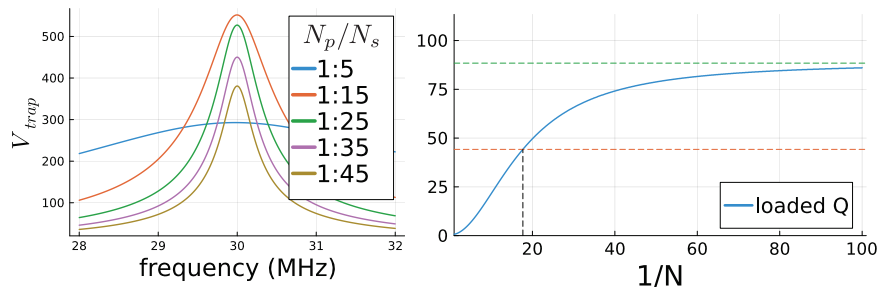
Figure 4.9: Impedance matching is achieved in practice by adjusting the number of turns on the primary coil while monitoring the transmitted power. One should not try to optimize the quality factor this way since the measured value will be half of its maximum when the circuit is properly matched to the source. In the plot to the right, the green dashed line corresponds to $Q = \frac{1}{R}\sqrt{\frac{L}{C}}$. The orange dashed line is half of that value. And the vertical black dashed line corresponds to N as given by Equation 4.5. The simulation assumes $C_{\text{trap}} = 30$ pF, $Z_0 = 50$ Ω, $R = 1$ Ω and a resonance frequency of 30 MHz.

4.4 Laser system and addressing optics

The six continuous wave diode laser sources we use to prepare and control the ions are housed in a separate, temperature-stabilized room and routed to our experiment via fiber optical cables. We share these sources with the various other experiments in the lab, which reduces the human cost of maintenance. A detailed description of the optical setup in the laser room is provided in [81]. The 375 nm and 422 nm lasers, used for photo-ionizing neutral calcium, are free-running. The 397 nm, 854 nm and 866 nm lasers used for addressing the short-lived dipole transitions in ^{40}Ca$^+$ are locked using a Pound-Drever-Hall scheme [27] to external reference cavities whose effective cavity lengths can be tuned remotely via piezo actuators. The 729 nm used for coherent manipulation of the ion is unique in that it requires a sub-kHz linewidth and a high-degree of long-term stability. The details of this laser are described in a separate section.

In Figure 4.10 we provide a schematic outlining the relative orientation of the lasers into the trap. In Figure 4.11 we provide a schematic of the optical control components used to further manipulate the laser light after it has been received on the optical table for the experiment.

729 nm laser

The 729 nm laser light is used to produce and manipulate coherent superpositions of the $S_{1/2}$ and $D_{5/2}$ states and, therefore, is required to have a uniquely narrow linewidth and long-term stability. This is accomplished by locking the diode output to a high-finesse cavity from Stable Laser Systems using a DLpro Fast Analog Linewidth Control (FALC) circuit [81]. A rough upper bound on the effective laser linewidth, at the position of the ions, is determined by Ramsey spectroscopy of the two-ion, magnetic field insensitive $(|S_{1/2}, m_j = -1/2\rangle|S_{1/2}, m_j = 1/2\rangle + |D_{1/2}, m_j = -1/2\rangle|D_{1/2}m_j = 1/2\rangle)/\sqrt{2}$ state, from which we estimate an FWHM value of $\approx 500\,\mathrm{Hz}$ (Figure 4.12) [19].

The cavity-locking process has the unintended consequence of imprinting sidebands on the laser spectrum at the frequency of the FALC's control loop. Since these features are heavily suppressed by the cavity, they can be observed in a beat note measurement between the light coming directly out of the diode and the same light after being transmitted through the cavity. An example measurement is shown in Figure 4.13.

The position of the servo bumps, at $\pm\,750$ kHz, tends to coincide with our axial trapping frequency and can cause significant driving of the carrier transition when exciting the axial sidebands. We can reduce the strength of the servo bumps by lowering the gain on the FALC, but there is a limit before the lock becomes unstable. Instead, we use the filtered light transmitted through the cavity to run our experiments.

But the intensity is very weak, so we use a two-stage injection locking scheme to provide sufficient amplification. Details of this scheme can be found in [2] and also in Dylan Gorman's thesis [39], but the essential idea is that the light transmitted through the cavity is used to *seed* another free-running 729 nm diode, known as the supervisor. If the supervisor's
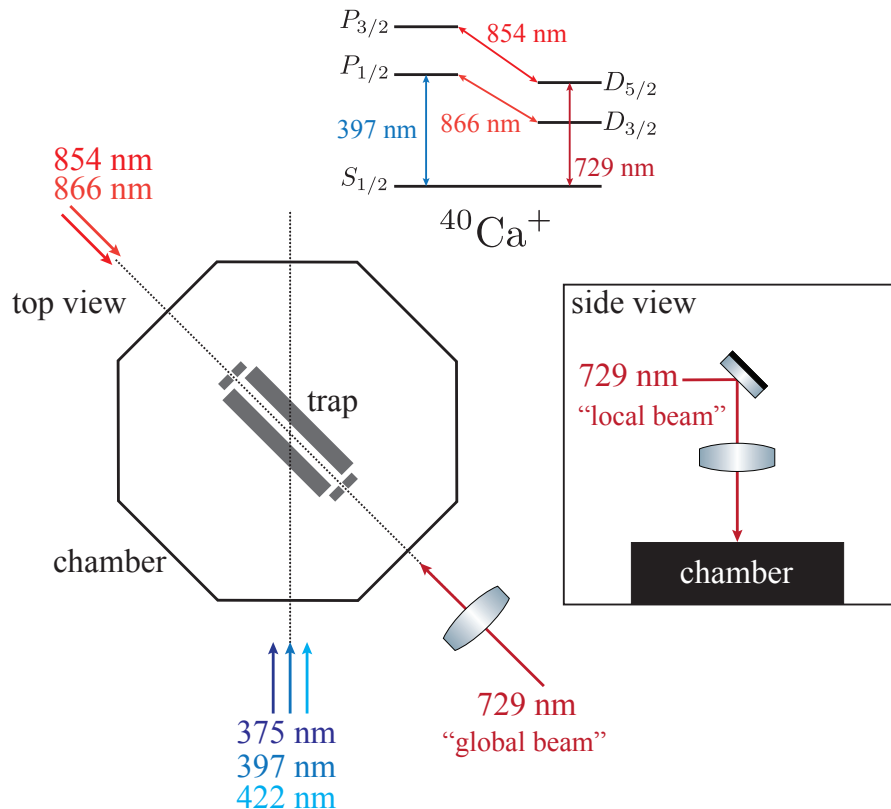
Figure 4.10: Orientation of addressing beams relative to vacuum chamber. The 375 nm, 397 nm and 422 nm light is all output from the same fiber. The orientation is chosen such that the 397 nm beam has an equal projection on all trapping axes in order to provide efficient Doppler cooling. Two separate 729 nm beam paths are used. The "global" 729 nm beam is directed through a pinhole in the endcaps and along the axis of the trap so that it can simultaneously address all ions. The diameter of the pinhole and the distance of the endcap from the trapping point prevents us from focusing the beam waist down to more than about 100 μm. The "local" 729 nm beam is directed down into the chamber from an elevated position and focused through a custom-built objective (Table 4.1). We can achieve a spot size with a diameter of several μm so this beam can be used for single-ion addressing.
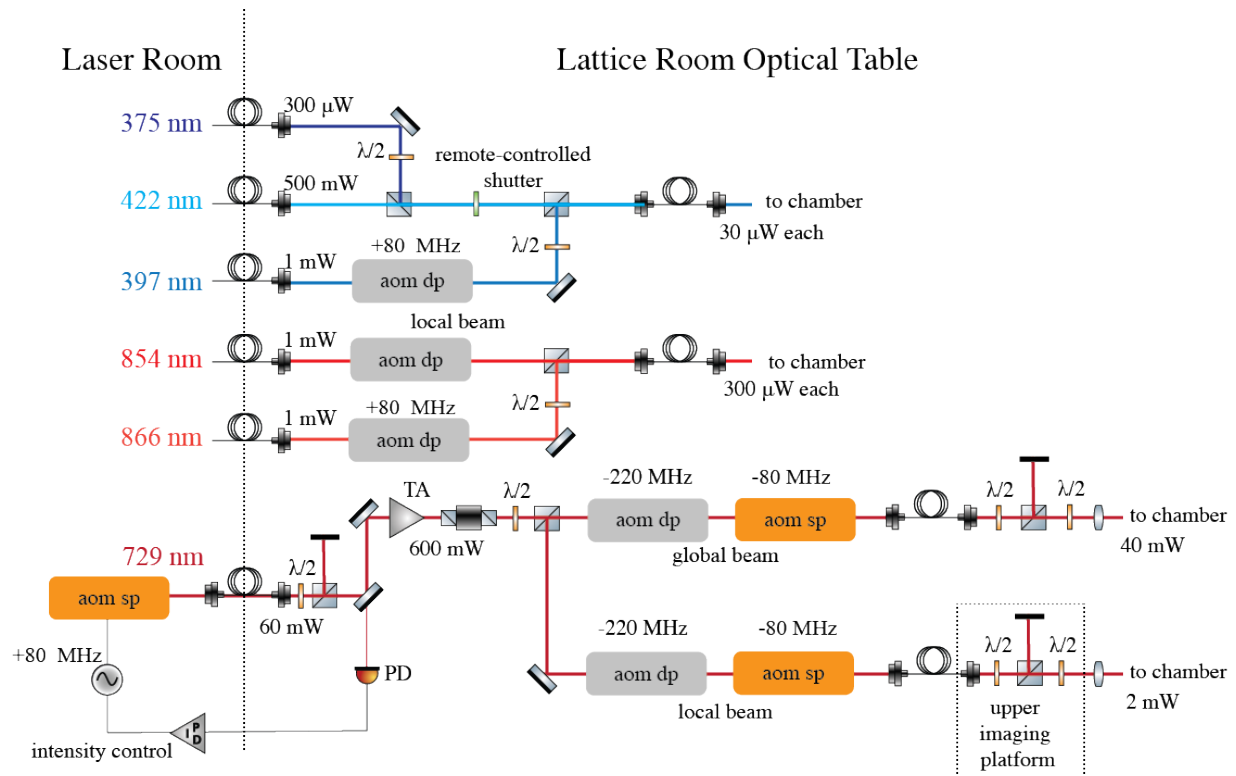
Figure 4.11: Lattice room optical layout. A sketch of the optical setup in the experiment room (known as the lattice room for historical reasons). Typical laser intensities are displayed, as measured directly after the fiber from the laser room and directly before entering the vacuum chamber. During experiments, fine-tuning of the laser frequencies is accomplished using a collection of acousto-optic modulators (AOMs) arranged in standard single pass (sp) or double pass (dp) configurations. The RF modulation signals used to drive the AOMs are all sourced from AD9910 direct digital synthesizer chips controlled by an Artiq Sinara control crate [12] and then sent through MiniCircuits RF amplifiers (2 W). The frequencies shown next to the AOMs correspond to their center frequencies and the sign indicates whether we out-couple the positive or negative first-order modulation sidebands. A remote-controlled shutter is used to quickly switch off the photo-ionization beams after the desired number of ions has been trapped. Additional details regarding the 729 nm paths are provided in Section 4.4. Not shown: various half and quarter waveplates and a cylindrical lens used for shaping the output beam from the TA.
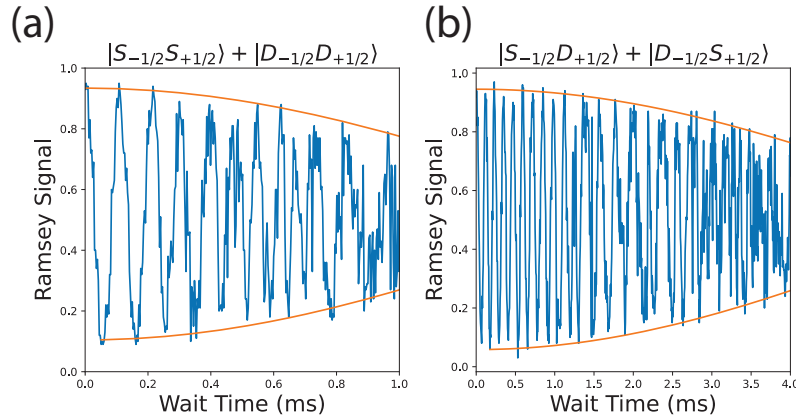
Figure 4.12: Effective laser linewidth measurement. **(a)** Ramsey spectroscopy of the state $(|S_{1/2}, m_j = -1/2\rangle|S_{1/2}, m_j = 1/2\rangle + |D_{1/2}, m_j = -1/2\rangle|D_{1/2}, m_j = 1/2\rangle)/\sqrt{2}$. This state is insensitive to magnetic field noise (both branches of the superposition have the same g-factor) but sensitive to laser phase noise. The orange curve is the fit of the data (blue curve) to a Gaussian decay envelope. If we assume that the phase noise of the laser is slow relative to the wait times, we can use the fitted decay constant to make a crude estimate for the laser linewidth of approximately 500 Hz. **(b)** It's interesting to compare the result in (a) to Ramsey spectroscopy on the $(|S_{1/2}, m_j = -1/2\rangle|D_{1/2}, m_j = 1/2\rangle + |D_{1/2}, m_j = -1/2\rangle|S_{1/2}, m_j = 1/2\rangle)/\sqrt{2}$ state, which is insensitive to laser phase noise, but sensitive to magnetic field noise. The coherence time is significantly longer, implying that, in many cases, our coherence times are limited by laser phase noise.

frequency is close enough to the seed, it will lock to it and output at the seed frequency. The supervisor's free-running frequency is adjusted by adjusting its temperature and drive current. In general, the lock tends to become less stable as the is driven at higher currents and/or higher temperatures, which both correspond to a larger output power. This is why we require the use of two stages.

Typically, we set the injection diodes to a fixed temperature and then adjust the currents as needed during the operation of the experiment and as determined by monitoring a beat note signal between the output of the master diode and another point in the beam path downstream of the second injection locking stage. If one of the injection diodes becomes completely unlocked, the beat note signal disappears. But often, it will only become "partially" unlocked, resulting in an excessively noisy spectrum. The current is then adjusted to recover a clean signal (there is a bit of an art to the process).

Once the 729 nm light is received on the experiment's optical table, it is fed through a tapered amplifier (TA). The long 20 m optical fiber used to route the light from the laser
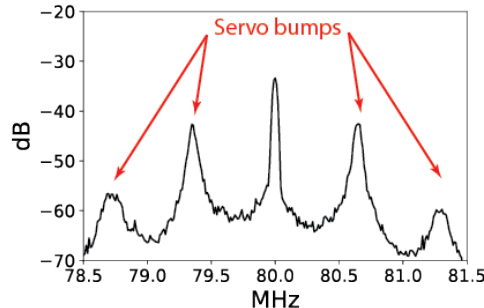
Figure 4.13: Servo bumps. Beat note measurement where 729 nm light output from the diode is overlapped on a polarizing beam splitter with the same light after being transmitted through a cavity and modulated at 80 MHz by an AOM. The intensity of the overlapped light is measured on a photo-diode. The strong sidebands at around 750 kHz (and higher multiples) are due to the cavity-locking process and are known as servo bumps.

room tends to induce significant polarization noise, which is inevitably converted to intensity noise at the position of the ions due to the polarizing beam splitters we use to maintain a well-defined linear polarization. The TA reduces this effect since we use a seed intensity well into the saturation regime (approximately 35 mW). To avoid over-seeding and damaging the TA, the seed intensity is fixed by a PID, which feeds back to an 80 MHz AOM in the laser room and uses a photodiode measurement of pickoff light from a mirror before the TA. This is the primary reason for the additional AOM single passes on the local and global beam paths shown in Figure 4.11. But we find that these are also useful when modulating the light with many tones, since, in this case, using the double pass would also result in the various sum tones being imprinted on the light.

The standard deviation of intensity fluctuations on the light measured directly after the TA is about 1% of its mean. But by the time it makes it to the vacuum chamber, this is increased to about 4%. We found that we could further reduce this to about 2% by covering the entire beam path with boxes, as shown in Figure 4.14.
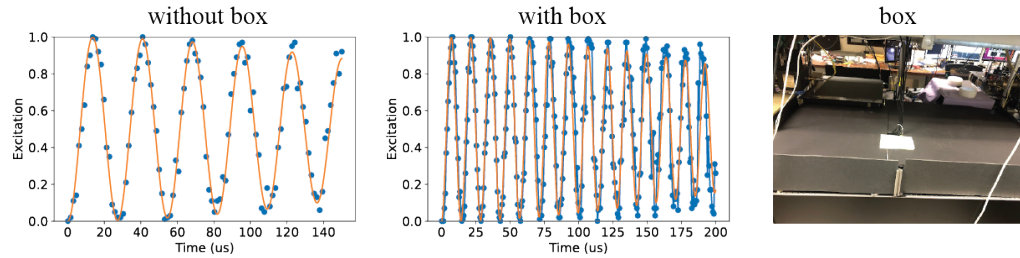
Figure 4.14: 729 nm laser intensity stability. Driven excitation of a $S_{1/2} \leftrightarrow D_{5/2}$ transition before and after boxing the beam path (rightmost image). Blue circles are data points and the orange curve is a fit to signal with Gaussian decay envelope. From the fitted decay constant, we estimate the relative intensity fluctuations (see Chapter 2).

4.5 Imaging

Ions are imaged by collecting 397 nm light scattered off of the $S_{1/2} \leftrightarrow P_{1/2}$ transition in a directional orthogonal to that of the laser beam. The scattered light is collected by a custom-built objective, designed by Jan Benhelm [6]. The known specifications are listed in Table 4.1. Importantly, the objective was designed to focus both 397 and 729 nm light[6], so it can be simultaneously used for single-ion addressing with the help of a dichroic mirror (see Figure 4.15). Once the 397 nm light passes the dichroic mirror it is split into two paths with a pellicle, one goes to an EMCCD camera and the other to a PMT.

For measurement, the PMT has the advantage of high quantum efficiency and a direct interface with the real-time control stack used to run the experiments. This allows conditional logic to be performed based on measurement results in real-time. The EMCCD, a Nuvu HNu 512, is currently not supported by the control hardware so we can only talk to it in real-time (by, for example, sending a TTL pulse to trigger a detection window), but not listen to it. The quantum efficiency of the Nuvu EMCCD is quite good ($\sim 95\%$) and we can reliably distinguish between a dark and bright ion with as low as several hundred μs of exposure time. However, we found that we needed to switch over to a binary threshold method for state discrimination, as opposed to the Gaussian fit method described in [82] and used previously (see Figure 4.16).

---

[6]but only on the optical axis

focal length	f-number	NA
70 mm	f/1.6	0.3125

Table 4.1: Known objective specifications.
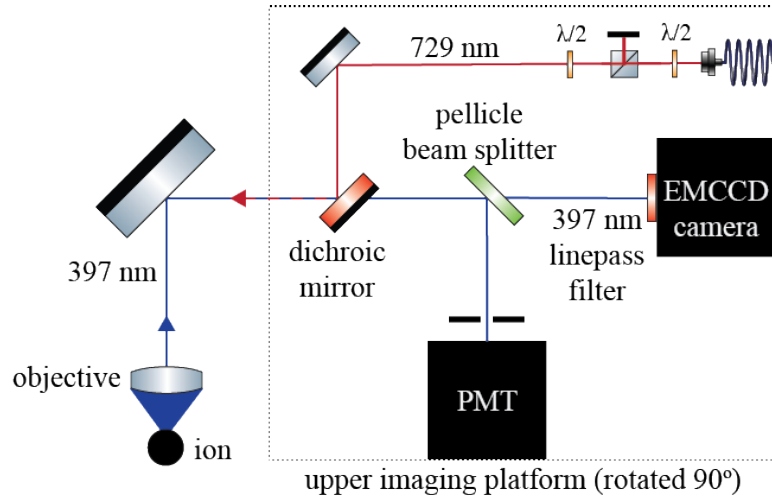
Figure 4.15: Imaging setup. The same objective is used to collect 397 nm light scattered off the ion and to focus down 729 nm light onto the ion for single-ion addressing. The rotation of the upper imaging platform by 90°indicated in the figure is about the axis connecting the dichroic mirror with the EMCCD camera. Figure is adapted from [81, 39].
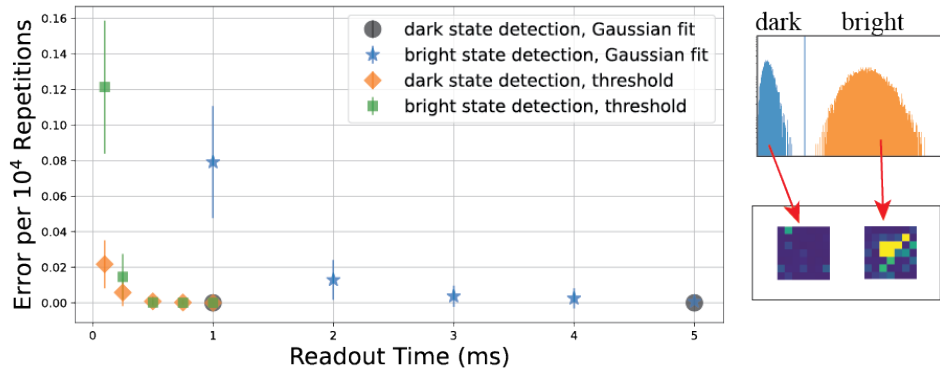
Figure 4.16: Camera readout fidelity as a function of readout duration. 10^4 camera exposures are taken with the 397 nm and 866 nm light shining on the ion, resulting in the bright distribution as labeled in the rightmost plot. And another 10^4 exposures are taken with the 866 nm light off, resulting in the dark distribution (population is quickly shelved in the $D_{3/2}$ state). For low exposure times, the binary threshold method (illustrated in right-most images) significantly outperforms the Gaussian fit procedure outlined in [82]. The region of interest used for these data points was 10x10 pixels large.

4.6 Hardware and software control

Running a trapped-ion experiment requires the coordination and control of a number of devices, often interfaced by different computers and, in some cases, shared with other experiments. Sometimes this coordination must be specified in real time. For example, a pulse sequence consists of turning on and off a sequence of laser pulses for precise durations. For these tasks we use an Artiq control system [12]. Other tasks do not require real-time control but do require asynchronous communication with a distributed collection of devices spread over the lab's local network. For these tasks, we use the LabRAD[7] control software developed by the John Martinis group at UCSB.

Since the functionalities provided by LabRAD and Artiq are different, it is straightforward to combine them within a single control procedure, which we often do. For example, the Artiq control system lacks support for our EMCCD camera. So when using the camera to measure the ions at the culmination of a pulse sequence, we communicate with it via a LabRAD server. In an "initialize" stage we set the user-specified camera parameters (e.g. region of interest, exposure time, number of exposures, etc.), and then, while the experiment is running, we have Artiq generate a TTL pulse that triggers the camera to take an exposure at a specific point in time (the point at which we would like to measure the state of the ions). Since we cannot coordinate with the camera in real-time, we allow the image data to accumulate in the camera's buffer and then transfer this information to the control PC where it is processed and stored, all of which is performed asynchronously so as not to interfere with the real-time execution of the experiment.

In the remainder of this chapter, we will describe the LabRAD and Artiq implementations in separate subsections. The entire control stack is more of a prototype than a finished product (though currently completely functional). It represents the first effort in the lab to integrate the Artiq control system into the preexisting architecture. For this reason, the focus will not be to flesh out the details but, rather, to provide a rough sketch of the basic structure and most important components, where to find things and what they do, to provide enough information for future students to pick up the development.

A schematic illustrating some of the basic components of the stack is provided in Figure 4.17 and a listing of some of the most important files and directories pertaining to the control code is found in Table D.1. In what follows, unless otherwise specified, file locations will refer to the main experimental (lattice) control computer.

LabRAD control

Essentially, LabRAD provdies us with a remote procedure call (RPC) protocol, whereby evaluation of some function defined in a LabRAD server[8], living somewhere on the local network, can be requested via TCP by another program, living somewhere else on the local

---

[7]https://github.com/labrad/pylabrad/wiki

[8]A basic example server, written in Python, can be found at ∼/LabRAD/common/tutorial/test-server.py
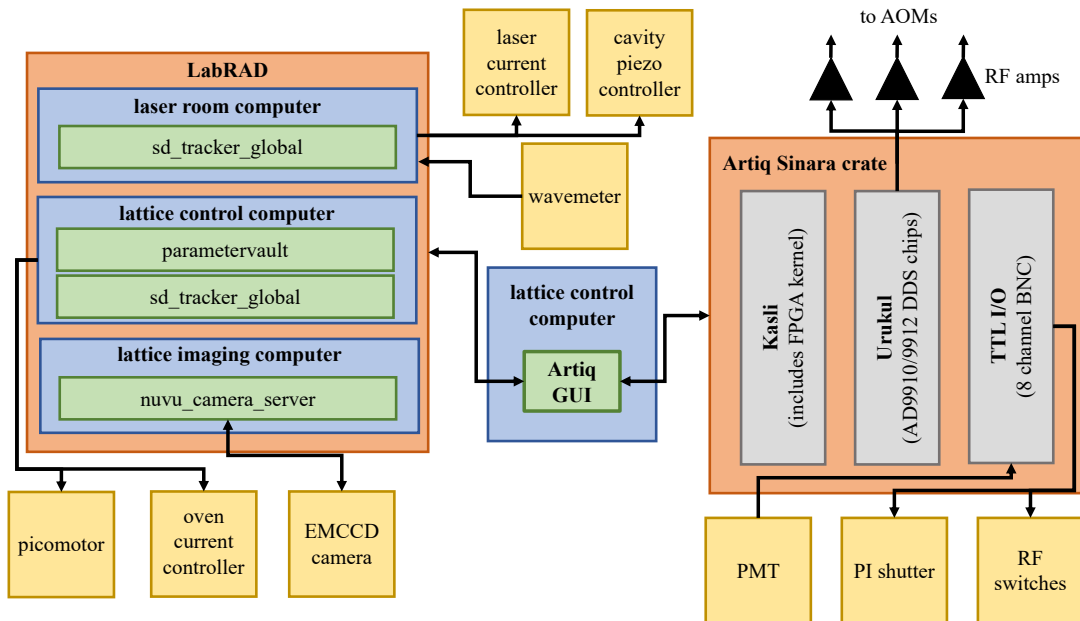
Figure 4.17: Hardware/software control stack. The two main control systems we use for running experiments are LabRAD and Artiq. LabRAD consists of a collection of servers running on computers distributed throughout the lab, which can be accessed from anywhere on the local network via remote procedure calls. Servers can either interface with physical devices (yellow boxes) or be self-contained software packages (e.g. parametervault or sd_-tracker_global). Artiq facilitates the real-time control of hardware that includes RF signal generators and TTL input/ouputs. The user primarily interacts with both of these controls through the Artiq GUI located on the main (lattice) control computer.

network. This allows for a highly modular architecture. Servers can be run on different computers, in different languages and can be shared simultaneously by multiple end-users. For example, on the main experimental control computer (called the "lattice control computer" in Figure 4.17) we run a GUI (called the "Artiq GUI"), which is the primary way that a user interacts with the experimental controls. This GUI contains modules written in Python3 that allow the user to monitor and specify parameters of the laser control system located in the laser room[9]. But the software that provides the actual interface to the various laser control devices is run in Python2 on a computer located in the laser room. LabRAD makes the integration of these different software packages seamless.

The first step in getting LabRAD up and running for experiments is to run the LabRAD web manager and lattice_control node server. A desktop icon on the lattice control computer allows this all to be done with a single click. The code launched by the desktop icon can be

---

[9]Code located at ∼/lattice/artiq/artiq/dashboard/laser_room

found at ~/launch_scripts/labrad_startup.sh. Once this is done, the lattice_imaging node server should be run on the lattice imaging computer (Windows machine), which primarily facilitates communication with the EMCCD camera.

Artiq control

Artiq is an open-source control suite, developed by M-Labs, that provides a high-level Python API for describing experiments, which can then be compiled down and run on an FPGA kernel that communicates with a collection of dedicated physical devices in real-time with sub microsecond resolution. For us, it essentially replaces the pulser and scriptscanner developed internally for running real-time experiments [82, 81]. These tools worked very well, but we found that there was a barrier to adding new features due to a lack of detailed documentation and since, on the software side, this required a working knowledge of event-driven programming and, on the hardware side it required the design and fabrication of new digital electronics boards. Artiq's high-level API, modular hardware architecture and well-maintained documentation[10] together overcome all of these limitations.

Artiq ships ready to run experiments out of the box. But we have built a minimal API on top of that based on the architecture of the scriptscanner software. This is all defined in the PulseSequence class, which inherits from the base EnvExperiment class provided by Artiq, and can be found at[11] ~/artiq/artiq/.pulse_sequence/pulse_sequence.py on the main experimental control computer. PulseSequence does the following:

- Resets and initializes all of the Artiq hardware.

- Determines scan parameters.

- Loads all needed parameters from the parametervault LabRAD server.

- Initializes the camera or PMT for measurement.

- Iterates through the scan parameters and for each scan point, runs code from a user-defined subsequence() function.

- For each shot composing the scan point, runs code from a user-defined sequence() function.

- Performs measurement with the camera or PMT.

- Compiles the measurement data, plots it and stores it to file.

- Resets the hardware to its initial state.

---

[10]https://m-labs.hk/artiq/manual/
[11]This is just a fork of the main Artiq github repo, so to incoporate any recent Artiq updates, they must be manually merged.

More technical details regarding the experimental control software, including the organization of the code on the experimental computer and some pulse sequence examples, are provided in Appendix D.

Chapter 5

Bounding causal nonlinear quantum mechanics

5.1 Introduction

Linear time evolution is a fundamental assumption of quantum mechanics [76]. Nonetheless, it has been demonstrated that reasonable theories relaxing this constraint, theories of so-called nonlinear quantum mechanics (NLQM), can be self-consistently designed [8, 97, 98, 24]. But rigorous experimental tests of these theories have been performed [91, 33, 10, 18, 96, 65] and, in all cases, no nonlinear effects were observed. Moreover, these NLQM theories have proven, quite generally, to violate causality when extended to the case of multipartite systems [37, 38, 78].

However, a fully causal NLQM (cNLQM) framework, building on earlier work by Kibble [54], has recently been proposed by David Kaplan and Surjeet Rajendran [52]. The interest in this work extends beyond simple theoretical curiosity since it predicts measurable effects that turn out to be poorly bounded by previous experiments. This is surprising given the remarkable success that standard quantum mechanics has demonstrated in accurately predicting the results of the immense amount of experiments performed in well-controlled quantum systems in recent years. The reason underlying the lack of sensitivity to the new theory in these systems is that (a) in the proposed cNLQM framework one is no longer free to separate out the center of mass (COM) degrees of freedom and (b) the magnitude of the nonlinear effects is generally decreased as the spread of the physical wavefunction increases.

This dependency on the center of mass coordinates means that standard atomic and nuclear spectroscopy, the gold standard in precision metrology, fails to provide a sensitive testbed for cNLQM unless the COM coordinates are localized on a scale comparable to the internal atomic or nuclear degrees of freedom, which is generally not possible. According to the authors of [52], the best estimate for the previously existing bounds on cNLQM, inferred from the current uncertainty in measurements of the Lamb shift, is just a factor 10^4 less than the leading order linear effects. This motivates the need for tailor-made experiments

specifically designed to be sensitive to causal nonlinear effects. This is especially true given the sweeping implications a nonlinear theory of quantum mechanics would hold across all areas of physics including cosmology, gravity and quantum information processing [52, 1].

In this chapter, we summarize an experiment that was designed and performed to test cNLQM using a single trapped $^{40}Ca^+$ ion [14]. The key feature of this experiment is that spectroscopy is performed directly on the quantized COM motion of the ion, which is tightly confined in a standard Paul trap. In short, a superposition of the ground and the first excited harmonic state of the ion is prepared and Ramsey interferometry is performed. The energy splitting between these two states is much smaller than many of the ion's experimentally accessible electronic transitions, which would ordinarily make them a poor choice for a precision experiment. But, as will be explained, the superposition of these states turns out to be highly susceptible to casual nonlinear effects, more than compensating for this limitation. Via this method, we can provide an improved bound of 5.4×10^{-12} on the magnitude of the unitless factor that scales the causal nonlinearity in a perturbative treatment. This represents an improvement of about seven orders of magnitude compared to the previous best estimates.

5.2 Theoretical background

When applied to a physical system, the hallmark of a nonlinear theory of quantum mechanics is the presence of terms in the system's Hamiltonian that are nonlinear with respect to its wavefunction. These terms can be interpreted as an interaction of the wavefunction with itself and, thus, tests of NLQM can be viewed as tests of the superposition principle since, even in an isolated system, a superposition of two states will generally no longer be stable in a nonlinear theory [1]. This self-interaction of the wavefunction also poses the central challenge in the preservation of causality in a nonlinear theory. This is due to the two seemingly contradictory features of standard quantum mechanics that the response of the wavefunction to some local interaction is instantaneous and that the wavefunction of an entangled multi-particle state is a nonlocal property shared by all constituent particles. This means, for example, that by performing a local operation on one-half of an EPR pair whose constituent particles are separated by a sufficiently large distance, one can superluminaly affect the other half of the pair through their shared wavefunction. In standard quantum mechanics, it is well-established that this superluminal effect on the wavefunction cannot be used to transmit information – thus preserving causality. However, this protection is no longer guaranteed in nonlinear theories, since the self-interaction of the wavefunction can convert a local action into a nonlocal interaction [37].

This is not to say that such a nonlocal interaction is a necessary condition of a nonlinear theory. As first pointed out by Polchinski, there do exist restricted forms of nonlinearities that are strictly causal [78]. Recently, and for the first time, a systematic approach for incorporating causal nonlinear evolution into quantum mechanics has been developed by David Kaplan and Surjeet Rajendran [52]. Their approach differs from previous constructions

of NLQM in that nonlinear evolution is incorporated directly into quantum field theory (QFT) rather than as a modification to non-relativistic, single-particle quantum mechanics as has conventionally been the case. Interestingly, it is shown in [52] that, through this approach, the seemingly unmotivated constraints imposed by Polchinski can be derived as a direct consequence of QFT. The basic idea presented in [52] is to introduce nonlinearities into a system's time-evolution by shifting any relevant bosonic field operators by a small amount proportional to the expectation value of the field operator acting on the full quantum state, which in some sense adds a sort of classical field interaction where the field is sourced by the position-space distribution of the system's interacting particles. In this way, causality is manifestly preserved through the normal machinery of field theory.

Beyond preserving causality, the QFT-first approach of the cNLQM framework presented by Kaplan and Rajendran has a couple of other features that differentiate it from previous NLQM theories. Firstly, it is a field-dependent theory. This means that it does not preclude the possibility that nonlinear effects scale differently with different interacting field theories. This feature is at odds with the motivation put forth by Steven Weinberg in his approach to NLQM [97, 98] where he hoped to propose precision tests of quantum mechanics that were independent of any specific field theory. Secondly, the new cNLQM theory breaks the basis-independence of linear quantum mechanics. Instead, just as in QFT, the position basis becomes the preferred basis. This feature is essential to the preservation of causality in the theory. This is because in cNLQM the self-interaction of a particle's wavefunction is treated as a "physical" interaction[1] rather than as a simple abstract addition of terms to its equations of motion. And the locality of this "physical" interaction is most naturally described in the position basis.

The special significance of the position basis in cNLQM is also the main reason why bounds set by previous tests of NLQM are inapplicable to the causal theory. For example, in the experiment performed by Bollinger et al. [10] nonlinear time-evolution was tested by performing Ramsey interferometry on a superposition of two hyperfine states of a $^9\text{Be}^+$ ion confined in a Penning trap [23]. A general feature of nonlinear time-evolution is that the phase measured by a Ramsey experiment on a two-level system will no longer be independent of the relative population weighting of the two branches of the superposition. That is to say, for a superposition of the two hyperfine states $|\uparrow\rangle$, $|\downarrow\rangle$:

$$|\psi(t)\rangle = \sqrt{p}|\uparrow\rangle + \sqrt{1-p}e^{i\phi(t)}|\downarrow\rangle \tag{5.1}$$

one should expect a dependence of ϕ on p if nonlinearities are present in the Schrödinger equation. This fact is used in the experiment to obtain a quite stringent bound on any possible nonlinearities on the order of a fraction 10^{-27} of the binding energy per nucleon of the ^9Be nucleus.

But the fundamental assumption made in obtaining this bound is that the Schrödinger equation can be expressed in an arbitrary basis – in this case, the approximate two-level basis

---

[1]In some sense, Kaplan and Rajendran's theory can be considered as a more literal interpretation of "wave-particle duality."

$\{|\uparrow\rangle, |\downarrow\rangle\}$. Under this assumption, ϕ is predicted to include a term due to the potential non-linearity ϕ_{nl}, which scales with p, the probability of finding the ion in a particular hyperfine state – a rather abstract modification of the Schrödinger equation given its basis-independent description. The bound on the nonlinearity is then obtained by failing to measure such a dependence on p at the limits of the sensitivity of the experiment. In contrast, the nonlinear effect predicted by cNLQM is assumed to be due to an electromagnetic field sourced by the properties of the ion and distributed in space according to the position-space expectation value of the wavefunction. However, the local strength of this field is damped by the large position-space spread of the ion's wavefunction due to its orbital motion in the Penning trap, severely compromising the sensitivity of the experiment.

It is helpful to illustrate cNLQM with an example, which will also set the stage for describing our experimental test of its predictions[2]. Though cNLQM is, by design, a fully relativistic theory capable of handling multiple particles (as verified in [52]), it also predicts novel phenomena in the single-particle, non-relativistic limit. For example, treated perturbatively, a single particle with charge q and Hamiltonian $\hat{H}$ is predicted to have the following nonlinear time evolution:

$$i\hbar\partial_t \Psi(t, \mathbf{x}) = \left(\hat{H} + \tilde{\epsilon}_\gamma \frac{q^2}{4\pi\varepsilon_0} \int d^4\mathbf{x}_1 |\Psi(t_1, \mathbf{x}_1)|^2 G_r(t, \mathbf{x}; t_1, \mathbf{x_1}) \right) \Psi(t, \mathbf{x}) \qquad (5.2)$$

where $\tilde{\epsilon}_\gamma$ is a small unitless parameter that scales the strength of the nonlinear perturbation and G_r is the relativistic retarded Green's function from the spacetime coordinates $(t_1, \mathbf{x}_1)$ to $(t, \mathbf{x})$. The nonlinear term added to the standard Hamiltonian in Equation 5.2 admits the simple interpretation of a classical Coulomb potential sourced by the quantum probability distribution of the charged particle's position. The causality of this self-interaction is protected by the Green's function.

In the nonrelativistic limit, when $||H||/\hbar \ll c/|\mathbf{x}_1 - \mathbf{x}|$, Equation 5.2 becomes:

$$i\hbar\partial_t \Psi(t, \mathbf{x}) = \left(H + \tilde{\epsilon}_\gamma \frac{q^2}{4\pi\varepsilon_0} \int d^3\mathbf{x}_1 \frac{|\Psi(t, \mathbf{x}_1)|^2}{|\mathbf{x}_1 - \mathbf{x}|} \right) \Psi(t, \mathbf{x}) \qquad (5.3)$$

where it is clear that the denominator of the integrand scales with the full position-space spread of the wave function, damping the perturbation accordingly. This is the primary effect responsible for the poor sensitivity of previous experimental tests of NLQM when applied to the causal theory.

This is not to say that it is impossible to design a sensitive experimental test of cNLQM[3]. One rather straightforward way to accomplish this goal is to take advantage of the net charge and tight and stable spatial confinement of a trapped ion by performing Ramsey

---

[2]This example is based on notes from personal communications with David Kaplan

[3]Under the reasonable assumption that our observed universe is classical in the sense that it has a significant overlap with the complete wavefunction of the total universe. See [52] for a discussion of this point.

interferometry on a superposition of the ground and first excited Fock states of one of its vibrational modes. If one prepares such a state:

$$|\psi(t=0)\rangle = \sqrt{p}|0\rangle + \sqrt{1-p}e^{i\phi_0}|1\rangle \tag{5.4}$$

(p assumed to be real) and allows it to evolve for some time T, then the dominant nonlinear effect is an additional p-dependent phase accumulation between the two branches of the superposition state:

$$|\psi(t=T)\rangle = \sqrt{p}|0\rangle + \sqrt{1-p}e^{i\phi_0+i\phi_L(T)+i\phi_{NL}(p,T)}|1\rangle \tag{5.5}$$

Here, $\phi_L(T)$ is a phase accumulated due to standard quantum mechanics and proportional to the frequency of the harmonic oscillator and $\phi_{NL}(p,T)$ is the p-dependent phase accumulated due to the nonlinear term. They are given by:

$$\phi_L(T) = \nu T \tag{5.6}$$

$$\phi_{NL}(p,T) = \tilde{\epsilon}_\gamma \frac{1-9p}{30\sqrt{2\pi}\hbar} \frac{e^2}{4\pi\varepsilon_0 x_0} T \tag{5.7}$$

where ν is the angular trap frequency of the harmonic oscillator, e is the fundamental charge of the electron, $x_0 = \sqrt{\hbar/m\nu}$ is the characteristic length scale of a harmonic oscillator with mass m and frequency ν and $\tilde{\epsilon}_\gamma$ is a unitless parameter that scales the strength of the nonlinearity in this perturbative calculation (the subscript γ indicates that this nonlinear term is associated with an electromagnetic field). The expressions in Equations 5.6 and 5.7 are found by plugging in the standard quantum mechanical oscillator Hamiltonian into Equation 5.3 and solving perturbatively, to leading order in $\tilde{\epsilon}_\gamma$, given the initial state in Equation 5.4.

All of the parameters on the right-hand side of Equation 5.7, except for $\tilde{\epsilon}_\gamma$, are either known or can be experimentally controlled. The total relative phase of the superposition state at time T (Equation 5.5), $\Phi(T,p) = \phi_0 + \phi_L(T) + \phi_{NL}(p,T)$ can be measured directly using Ramsey interferometry [71]. The phase due to the nonlinearity $\phi_{NL}(p,T)$ can then be disambiguated by repeating the Ramsey experiment with two different values of p, which allows us to compute:

$$\Delta\phi_{NL}(\{p_i\},T) = \Phi(T,p_1) - \Phi(T,p_2) = \phi_{NL}(T,p_1) - \phi_{NL}(T,p_2) \tag{5.8}$$

The quantity $\Delta\phi_{NL}(\{p_i\},T)$ then allows us to make an empirical estimate of the strength of the nonlinearity $\tilde{\epsilon}_\gamma$. This method is particularly nice since, by default, it eliminates many potential systematic sources of uncertainty in the estimate like those due to slow drifts over time of the trap frequency ν or initial phase ϕ_0, which might result from unstable trapping potentials or laser parameters.

Even for standard experimental parameters, the ϕ_{NL} is not expected to be particularly small. For example, if a $^{40}Ca^+$ ion has a $\nu \sim 1$ MHz trap frequency and is prepared in the superposition state described in Equation 5.4 it will accrue a phase of order $10^{10} \times \tilde{\epsilon}_\gamma$ for each millisecond of interrogation time. Ramsey experiments like this have been performed [88] with interrogation times exceeding tens of milliseconds. But these experiments are generally performed for a fixed $p = 0.5$, which maximizes the Ramsey contrast. So these results cannot directly distinguish between ϕ_L and ϕ_{NL}. Though, for these experiments, given reasonable assumptions about the intensity stability of the laser used to generate the initial state and, thus, assumptions about the variance of the actual value of p generated from run-to-run, one should already guess that the bound on $\tilde{\epsilon}_\gamma$ will be tighter than the 10^{-4} estimate obtained from Lamb shift measurements[4]. Nonetheless, a dedicated experiment that directly measures $\Delta\phi_{NL}(\{p_i\}, T)$ from Equation 5.8 in order to obtain an unambiguous estimate of $\tilde{\epsilon}_\gamma$ is warranted. In the remainder of this chapter, we describe the design and implementation of an experiment that does just that.

We make two final remarks to conclude this section. First, the quantity computed in Equation 5.7 assumes an isotropic quantum harmonic oscillator for simplicity. In general, ion trap experiments are performed in an anisotropic regime. If we label the trap frequency for the vibrational degree of freedom along which we generate the superposition state as ν_z (formally labeled simply as ν in Equation 5.7) and label the trap frequencies for the other two spatial degrees of freedom as $\nu_{x,y}$, then the anisotropy can be accounted for by multiplying ϕ_{NL} by a factor of $\sqrt{\nu_x \nu_y / \nu_z}$. Secondly, if the ion's vibrational modes are not initialized precisely into the ground state but, rather, a low-temperature thermal state (as would be the case for imperfect laser cooling), then this must be taken into account in the calculation of x_0 in Equation 5.7. In general, the increased spread of the spatial wavefunction will reduce the strength of the nonlinear signal in addition to reducing the contrast of the Ramsey oscillations.

5.3 Experimental implementation

To test the new theory of cNLQM, we perform a Ramsey experiment, as described in the previous section, using a single $^{40}Ca^+$ ion confined in a three-dimensional Paul trap with trap frequencies of $\nu_z \approx 2\pi \times 1.01$ MHz, $\nu_x \approx 2\pi \times 2.52$ MHz and $\nu_y \approx 2\pi \times 2.79$ MHz along the three spatial axes. Here, the z-direction is taken to be along the axial direction of the trap, as defined in Chapter 2. As described in Chapter 4, confinement along the axial direction is particularly stable since the axial trapping potential is sourced by DC electrodes as opposed to the RF potential used to generate the pseudopotential in the x and y directions. For this reason, it is along this direction that we ultimately prepare the Fock state superposition for the Ramsey experiment.

---

[4]Given the p-dependence of ϕ_{NL}, fluctuations in p will manifest as a decoherence mechanism in the Ramsey experiment provided that $\tilde{\epsilon}_\gamma$ is nonzero

At the outset of each experimental run, the ion is prepared in the electronic state $|4^2S_{1/2}, m_j = -1/2\rangle$ using optical pumping. By subsequently exciting either the $|4^2S_{1/2}, m_j = -1/2\rangle \leftrightarrow |3^2D_{5/2}, m_j = -1/2\rangle$ or $|4^2S_{1/2}, m_j = +1/2\rangle \leftrightarrow |3^2D_{5/2}, m_j = +1/2\rangle$ and comparing the excitation probabilities, we confirm that the ion is indeed prepared in the $|4^2S_{1/2}, m_j = -1/2\rangle$ with a rough lower bound of 99% probability (though we expect that this probability is likely higher by at least an order of magnitude). The vibrational state of the ion along the axial direction, is likewise prepared with greater than 93% probability in its ground state using a combination of Doppler cooling and resolved sideband cooling. This probability is calculated[5] by taking the measured ratio of the maximum excitation of blue sideband versus red sideband transitions as well as by fitting measured blue sideband Rabi oscillations to Equation 3.19. Characteristic data for these measurements is illustrated in Figure 5.1. The vibrational motion of the ion along the two radial directions is only Doppler-cooled to a mean thermal phonon occupancy of approximately 3 quanta.
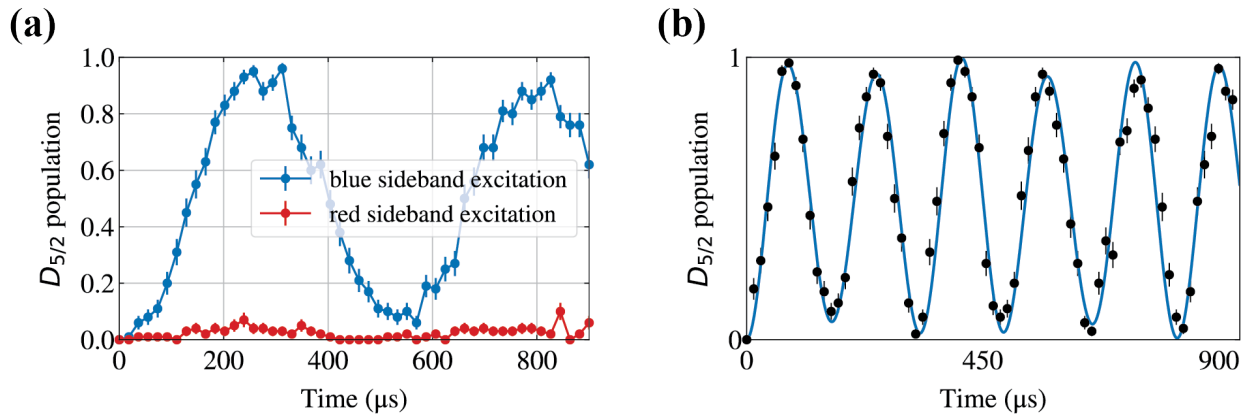
Figure 5.1: Axial mode temperature measurements. **(a)** After preparing the ion in the state $|4^2S_{1/2}, m_j = -1/2\rangle$ and laser cooling its axial motion, blue and red sidebands of the $|4^2S_{1/2}, m_j = -1/2\rangle \leftrightarrow |3^2D_{5/2}, m_j = -1/2\rangle$ transition are driven with well-focused laser light. By assuming a thermal distribution for the axial vibrational state and comparing the maximum excitation probabilities, a mean phonon occupancy of $\bar{n}_z \approx 0.073$ quanta is estimated. In practice, this is determined by performing spectroscopy on these transitions. **(b)** A complementary estimate of $\bar{n}_z$ is found by driving a blue sideband Rabi oscillation and performing a least squares fit, again assuming a thermal distribution. In agreement with **(a)**, this results in an estimate of $\bar{n}_z \approx 0.077$ quanta.

Once the ion is initialized into the state[6] $|S, n_z = 0\rangle$, the next step is to prepare a

---

[5]Under the assumption that the ion is prepared in a low-temperature thermal state.

[6]For the remainder of this section we will simplify the notation describing the ion's state as $|4^2S_{1/2}, m_j = -1/2\rangle = |S\rangle$, $|3^2D_{5/2}, m_j = -1/2\rangle = |D\rangle$. We will also suppress the radial vibrational states, which don't play a direct role in the dynamics.

superposition of the ground and first excited Fock state. The simplest way to accomplish this is to address the blue sideband with a controlled laser pulse amounting to a rotation of the ion's state $R_{\phi_0}^{\text{BSB}}(\theta)$, in the notation of Section 3.5, such that:

$$R_{\phi_0}^{\text{BSB}}(\theta)|S, n_z = 0\rangle = \cos(\theta)|S, 0\rangle + \sin(\theta)e^{i\phi_0}|D, 1\rangle \tag{5.9}$$

where we drop the explicit reference to the n_z in the Fock state description here and for the remainder of this section. In this case, the experimental sequence is as illustrated in Figure 5.2(a). After a free evolution time of T, the two branches of the superposition in Equation 5.9 accumulate a relative phase with respect to the addressing laser of:

$$\Phi(T, p) = \phi_0 + \frac{B}{2}(g_D - g_S)T + \phi_{NL}(T, p) \tag{5.10}$$

where $p = \cos^2(\theta)$ is the population of the electronic ground state and B is the magnitude of the magnetic field at the position of the ion. After a time T, a blue sideband π-pulse is used to map the relative phase information onto the electronic populations that are then measured via the electron shelving method. The problem with this method is the sensitivity of the phase to the ambient magnetic field, the stability of which limits the interrogation time to only a few milliseconds (see Figure 5.3).

To overcome this limitation, we instead use a combination of carrier and blue sideband pulses to generate the state [88]:

$$|D\rangle \otimes (\cos(\theta)|0\rangle + \sin(\theta)e^{i\phi_0}|1\rangle) \tag{5.11}$$

where the electronic state of the ion is disentangled from the superposition of Fock states. The procedure for preparing this state consists of two steps. First, a superposition with the desired population weightings is generated on the electronic states by driving a carrier transition. Second, a blue sideband π pulse is applied. Since, ideally, the ion is initially cooled down to its ground state of motion, this second blue sideband pulse only affects the population in the electronic state $|S\rangle$ – thus mapping the superposition of electronic states onto the vibrational state of the ions. At the end of the interrogation time, a second blue sideband π-pulse is used to remap this superposition onto the ion's electronic states and then a final carrier $\pi/2$-pulse is used to write the relative phase information of this state onto the electronic populations. An illustration of this procedure is provided in Figure 5.2(b).

At the end of the experiment, the probability of measuring the ion to be in the state $|D\rangle$ is explicitly given by:

$$P(T) = B - \frac{A(T)}{2}\cos[\Phi(T, \theta) + \xi_L] \tag{5.12}$$

Here $0 \leq A(T) \leq 1$ is the signal contrast, which will generally be less than one when $\theta \neq \pi/2$ and will also generally decrease superlinearly in time due to decoherence. $B \approx 1/2$ is an offset that is expected to be very close to $1/2$ but may deviate slightly from this value due to imperfect state preparation and off-resonant excitations of the laser interactions. The

parameter ξ_L is an offset in phase that depends on several relatively stable experimental parameters, like the detuning of the laser pulses from resonance, but can also be fully controlled modulo 2π by adjusting the phase of the final carrier pulse relative to the initial pulse.
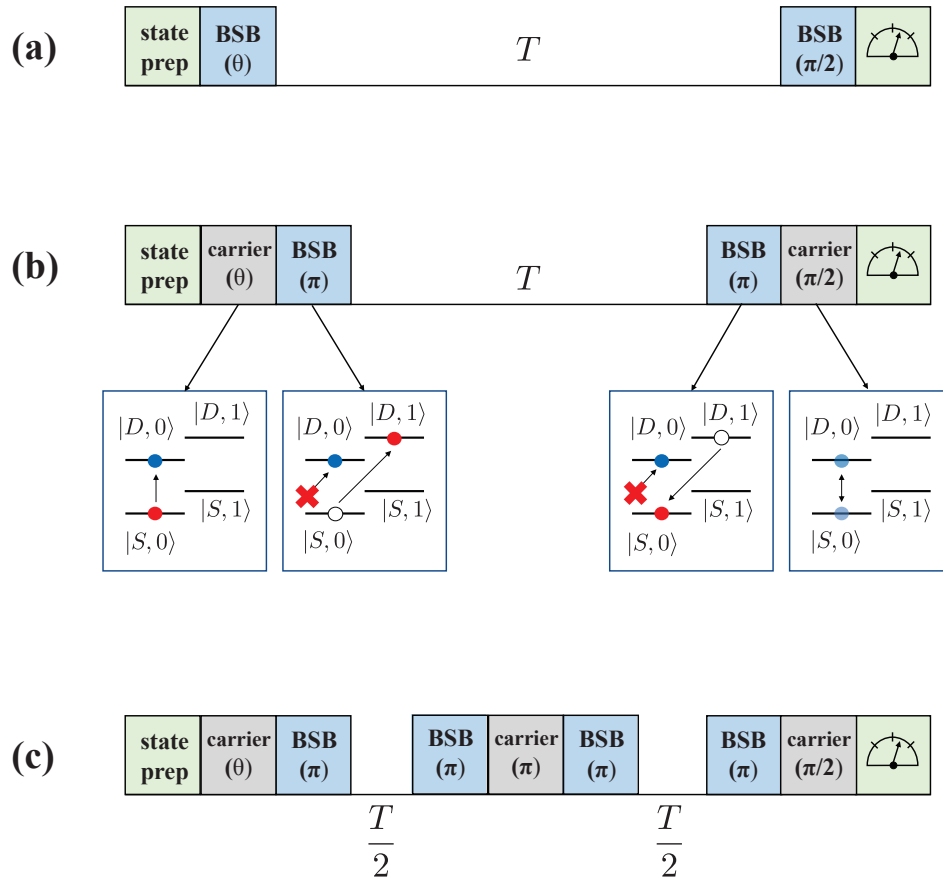
Figure 5.2: Pulse sequences for testing cNLQM. A simple experiment that is sensitive to cNLQM is Ramsey interferometry performed on a superposition of the states $|S, 0\rangle$ and $|D, 1\rangle$, as illustrated in **(a)**. But this superposition is also sensitive to ambient magnetic fields, which limits the interrogation time. An alternative approach is to use a combination of carrier and blue sideband pulses to generate a superposition of the ground and first excited Fock states, which is *disentangled* from the magnetic field sensitive electronic states. This method is illustrated in **(b)**. A further improvement can be made by applying a sequence of carrier and blue sideband pulses midway through the interrogation time, as shown in **(c)**. This has the effect of swapping the probability amplitudes between the two Fock states, analogous to a spin echo pulse in a standard Ramsey experiment, and provides two benefits. First, it cancels out the effect of drifts in the initial phase ϕ_0 (due, for example, to drifting trap potentials) provided that these drifts are slow relative to T. Second, it results in a direct measurement of $\Delta\phi_{NL}$ (Equation 5.8), which otherwise requires two measurements.
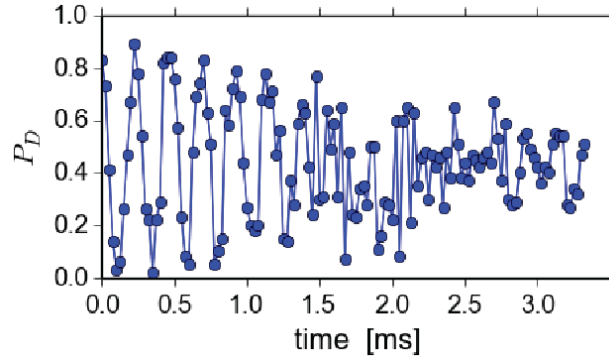
Figure 5.3: Noisy carrier Ramsey. Measured Ramsey oscillations as a function of inter-rogation time on a superposition of the electronic states $|4^2S_{1/2}, m_j = -1/2\rangle \otimes |0\rangle$ and $|3^2S_{5/2}, m_j = -1/2\rangle \otimes |0\rangle$. Because these two states have different g-factors and, thus, dif-ferent magnetic field susceptibilities, the coherence time of the superposition is limited by ambient magnetic field fluctuations.

We gauge the performance of the Ramsey experiment by applying a small detuning Δ from resonance to the first blue sideband pulse, which, in the rotating frame, breaks the degeneracy of the $|0\rangle$ and $|1\rangle$ states leading to a time-dependent contribution to the phase Φ (Equation 5.8) of ΔT. The resulting Ramsey oscillations are plotted in red in Figure 5.4(a) from which the coherence time can be estimated to be on the order of several tens of milliseconds. The dominant decoherence source is found to be reasonably well modeled by a Markovian heating of the vibrational mode, presumably caused by ambient electric field fluctuations at the position of the ion and, perhaps, high-frequency noise on the trapping potential [89]. If the ion is cooled down to its ground state and allowed to freely evolve, the effect of this heating can be incorporated into the dynamics of the system with the following master equation [16]:

$$i\hbar\partial_t\hat{\rho} = 2\gamma(N+1)\mathcal{L}(\hat{\rho};\hat{a}) + 2\gamma N\mathcal{L}(\hat{\rho};\hat{a}^\dagger) \tag{5.13}$$

where $\mathcal{L}$ are Lindblad terms as defined in Equation 2.127, $\hat{a}$ is the annihilation operator for the vibrational mode, γ is a constant that characterizes the strength of the heating and N is the mean phonon occupancy of the environment, which is taken to be large enough such that $N \gg \langle\hat{a}^\dagger\hat{a}\rangle(t)$ for all times t of interest. Practically speaking, Equation 5.13 describes a random process where the vibrational mode may spontaneously absorb a phonon from the environment. When n phonons are absorbed, the state of the system after the final blue sideband pulse will be $|S\rangle(\alpha_0|n\rangle + \alpha_1|n+1\rangle)$ and the result of the final $\pi/2$-pulse, regardless of Φ, will be a symmetric distribution of $\{|S\rangle, |D\rangle\}$ – diminishing the averaged signal contrast.

More precisely, under Equation 5.13, if the ion is initially prepared in a thermal state with a mean phonon occupancy of $n_0 = \langle\hat{a}^\dagger\hat{a}\rangle(t=0)\rangle$ then at some later time t it will have evolved

into a thermal state with a mean phonon occupancy of $\hat{a}^\dagger\hat{a}(t)\rangle = n_0(1 - e^{-\gamma t})$. Thus, for times t, such that $\gamma t \ll 1$, the increase of the ion's mean phonon occupancy is approximately linear. Figure 5.5 shows the results of independently measuring the temperature of the ion's vibrational mode as a function of time, from which we estimate that $\gamma \approx 10$ quanta per second. The black dashed curve in Figure 5.4(a) shows the results of simulating the decay curve for the full Ramsey experiment, including heating, under the assumption of this independently measured value of γ. The good agreement between this simulated decay envelope and the measured data verifies our claim that heating is the dominant decoherence process. We further verify this claim by performing the experiment illustrated in Figure 5.2(c), which includes a sequence of laser pulses midway through the experiment, analogous to a spin echo, that should effectively cancel out any slow drifts of ϕ_0 (due for example to slow drifts of the laser or the trapping potential), which we expect to be the next most significant source of decoherence. We find the coherence time to be largely the same as for the un-echoed Ramsey experiment.

To extract Φ from the electronic population measurements described by Equation 5.12, we perform three independent measurements at a fixed T but with three separate values of ξ_L, as controlled by the phase of the laser pulse. The values of ξ_L are separated by ninety degrees such that $\xi_L^{(3)} = \xi_L^{(2)} + \pi/2 = \xi_L^{(1)} + \pi$. The targeted value of $\xi_L^{(1)}$ is chosen to minimize the standard deviation of $\Phi(\tau)$:

$$|\delta\Phi(\tau)| = \sqrt{\sum_i \left(\frac{\partial\Phi}{\partial P_i}\delta P_i\right)^2} \tag{5.14}$$

which occurs when $\Phi(T) + \xi_L^{(1)} = \pi/2$. Here P_i is the population measurement associated with $\xi_L^{(i)}$ and δP_i is its standard deviation, nominally dominated by quantum projection noise (QPN) [49]. This is illustrated in Figure 5.6.

As discussed in the previous section, a potential nonlinear signal in the phase is most easily disambiguated by measuring Φ for two different values of $p = \cos^2(\theta)$ and taking the difference $\Delta\phi_{NL}$ (as in Equation 5.7). This method has the added benefit of being robust against slow drifts of the signal due to drifting trap potentials or laser parameters. For our experiment, we choose θ_1 and θ_2 such that the ground state population of the Ramsey superposition is initialized at either $p = 0.2$ or $p = 0.8$. The nonlinear signal $\Delta\phi_{NL}$ grows linearly with interrogation time T. But this effect must contend with the contrast decay, which increases the uncertainty of the signal (Eq. (5.14)) and which favors shorter, more frequent measurements [48]. The combination of these effects results in an optimal interrogation time, which we determine experimentally by measuring $\Delta\phi_{NL}(T)$ at various T and computing the sample standard deviation. These results are normalized to an integration time of $1\,\mathrm{s}$ and plotted in Fig. 5.4(b). The blue-shaded region is a corresponding simulation that assumes only QPN and vibrational heating bounded by $7 \leq \dot{n} \leq 13$ quanta/s. Based on this data, we fix $T = 15\,\mathrm{ms}$.
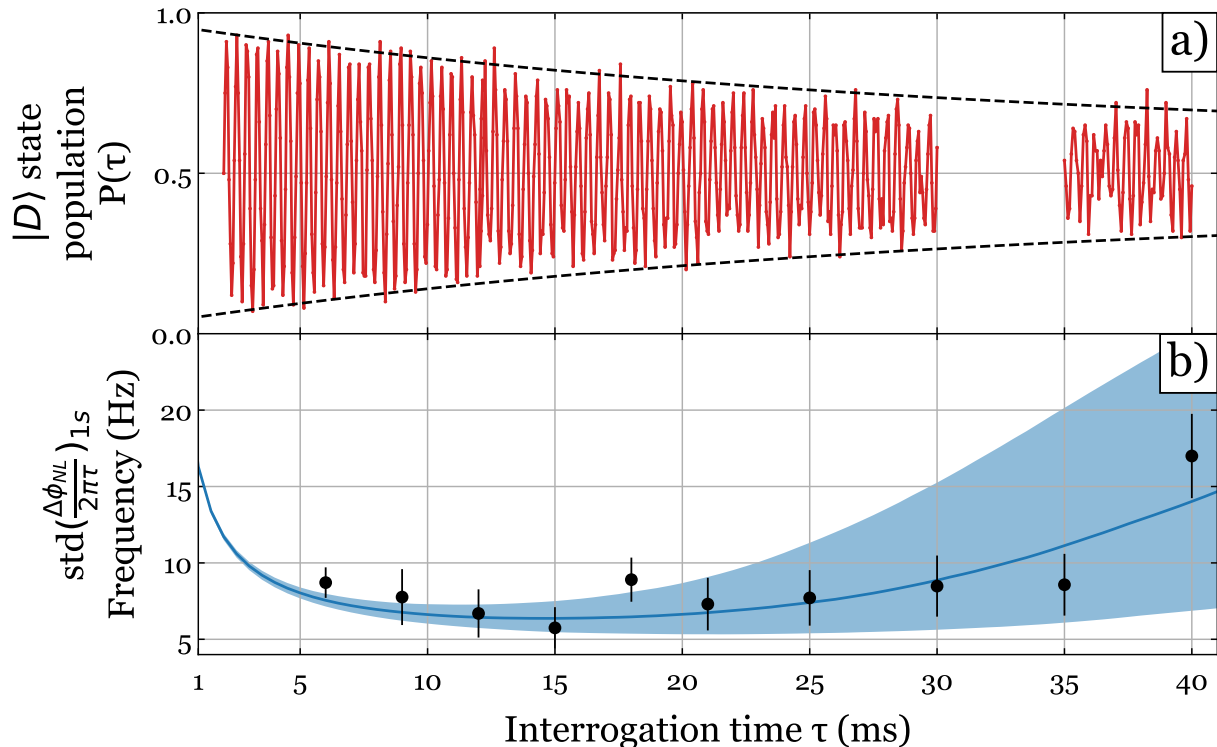
Figure 5.4: cNLQM experimental performance [14]. **(a)** Measured $P(\tau)$, as described by Eq. (5.12) (red). The black dashed line is the predicted decay envelope taking into account only heating of the vibrational mode at a rate of 10 quanta/s. The reasonable agreement between the predicted and measured decay suggests that the Ramsey signal contrast is dominated by this heating process. **(b)** The black circles represent the sample standard deviation from repeated measurements of $\Delta\phi_{NL}(\tau)$ taken at various interrogation times and normalized to an integration time of 1 s. The blue shaded region bounds the simulated predictions assuming only QPN and a heating rate between 7 and 13 quanta/s (lower and upper edge of the region, respectively). The dark blue line corresponds to 10 quanta/s.
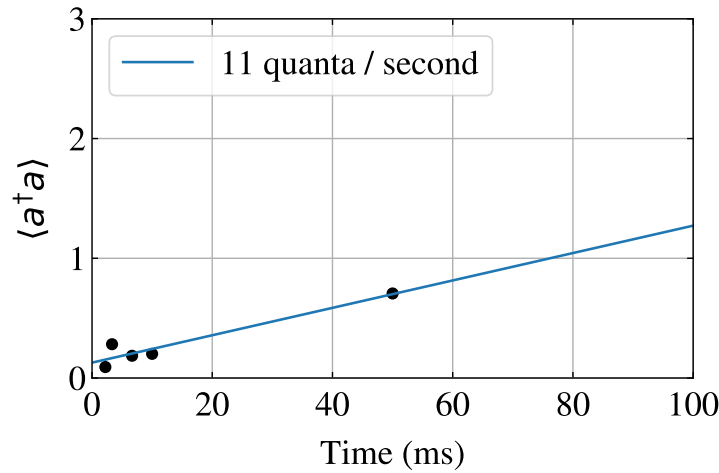
Figure 5.5: Heating rate measurement. The black circles represent measurements of the mean phonon number of the vibrational mode at various times. The blue curve is a linear fit to the data.
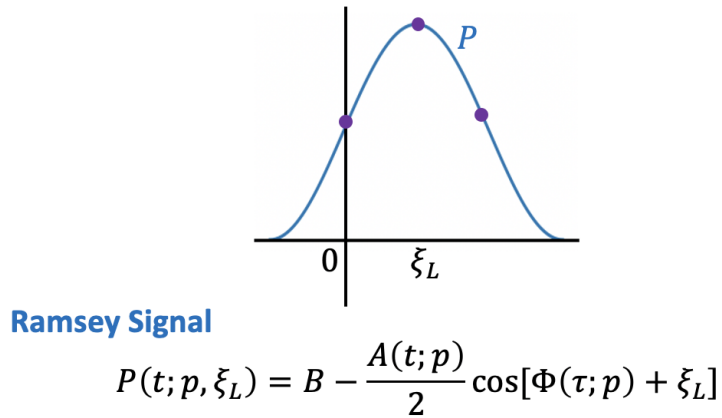
Figure 5.6: Three point Ramsey measurement. In order to extract the phase due to the hypothetical nonlinearity, for each fixed value of t and p, three separate measurements are performed with varying ξ_L separated from one another by ninety degrees.

5.4 Results

A sketch of the full experimental procedure that we used in our test of cNLQM is given in Figure 5.7. It begins with a passive calibration of the two initial ground state populations, corresponding to θ_1 and θ_2, and of the Ramsey superposition used to obtain our measurement of $\Delta\phi_{NL}$. For the most part, this consisted of a measurement of the $|D\rangle$ state population after the first carrier pulse. This value was then recorded and used in the final calculation of $\tilde{\epsilon}_\gamma$. However, if either θ_i drifted enough from the nominal values of 0.2 and 0.5 (due, for example, to drifts in the laser parameters) we would adjust the intensity of the laser pulse. After this, a three-point Ramsey measurement was performed to find the optimal bias point of the laser phase. These were performed with an initial ground state population of approximately $1/2$ to maximize the contrast of the signal. Finally, a pair of three-point Ramsey measurements were performed, one for each value of θ_i. These six phase estimates (each obtained from 200 sequential measurements) were performed in a random order to scramble any correlated drifts of Φ. Using the results of these six measurements a single value of $\Delta\phi_{NL}$ was computed, from which an estimate of $\tilde{\epsilon}_\gamma$ was estimated, according to Equation 5.7. In total, this amounts to 1500 single-shot experiments to obtain a single estimate of $\tilde{\epsilon}_\gamma$.
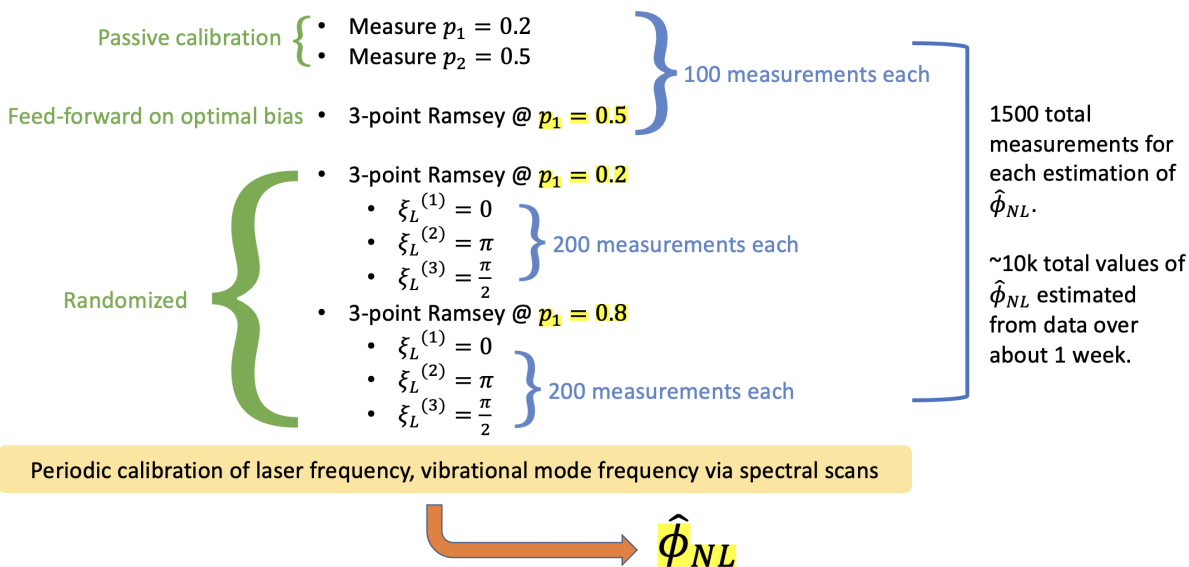
Figure 5.7: cNLQM experimental procedure. See text for more details.

This sequence was ultimately repeated about ten thousand times over the course of a week. In Figure 5.8(a) we illustrate the resulting measurements of the three parameters in Equation 5.12 as a function of time for a single day's worth of data. The red dots show data taken at $15\,\mathrm{ms}$ divided by the golden ratio $(1 + \sqrt{5})/2 \approx 9.27\,\mathrm{ms}$, which does not

improve the estimate of the nonlinearity but allows us to rule out the remote possibility that $\Delta\phi_{NL}(T{=}15$ ms) modulo 2π vanishes even though the perturbation is not small. The distribution of $\tilde{\epsilon}_\gamma$ computed from the measured values of $\Delta\phi_{NL}(T{=}15$ ms) and θ_i is shown in Fig. 5.8(b). The black curve is a Gaussian fit. The mean value is determined to be $5 \pm 5.4 \times 10^{-12}$ where the reported uncertainty corresponds to 1 standard deviation. The average uncertainty of the individual measurements computed using standard propagation of error and assuming only QPN is found to be 7.7×10^{-11}, which is in good agreement with the sample standard deviation 8.2×10^{-11}.
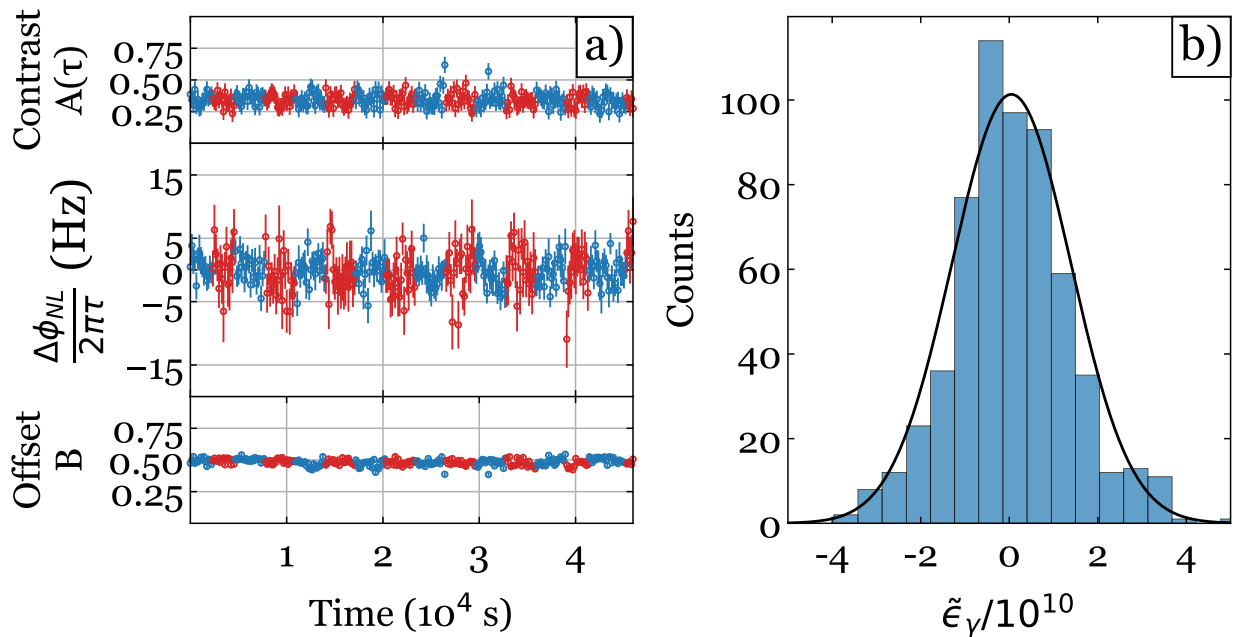
Figure 5.8: cNLQM results [14]. **(a)** (top to bottom) The measured contrast, frequency and offset over a full day of data collection. The blue circles represent data taken at an interrogation time of 15 ms and the red circles were taken at a time of 15 ms divided by the golden ratio ($\approx$9.3 ms). **(b)** The distribution of $\tilde{\epsilon}_\gamma$ estimated from the data. The mean value is $5 \pm 5.4 \times 10^{-12}$. The black curve is a Gaussian fit to the distribution.

In summary, using Ramsey spectroscopy on a superposition of the ground and the first excited state of the axial vibrational mode of a trapped $^{40}\text{Ca}^+$ ion, we have bounded the unitless scaling factor $\tilde{\epsilon}_\gamma$ of a hypothetical electromagnetic nonlinear perturbation to the Schrödinger equation to a value on the order of 10^{-11}. Compared to the previous best estimate of this bound, based on measurements of the Lamb shift of hydrogen, this represents an improvement of roughly seven orders of magnitude. In principle, this result could be improved with longer averaging times, longer coherence times, higher mass atoms, larger trapping potentials, and, perhaps, more sophisticated motional state superpostions. In most

cases, these improvements will lead to modest gains in spectroscopic performance, as we touch on in the concluding chapter of this thesis. As a final note, we emphasize that cN-LQM is field-dependent. Here we have provided a bound on electromagnetic fields, but the framework presented by Kaplan and Rajendran [52] is quite general and can be used to treat any interacting field theory. For example, it is interesting to think about how one might design complementary experiments that test for similar nonlinearities in gravitational fields, though, due to their small mass, atomic systems are likely ill-suited for this purpose.

Chapter 6

Using entanglement to improve the bounds on Lorentz symmetry

6.1 Introduction

The frequency sensitivity of Ramsey spectroscopy can be enhanced by the use of entanglement [11]. However, the same mechanism responsible for this improvement also causes an increased susceptibility to noise [48]. This calls into question whether entanglement is a useful resource in metrology. However, in many real systems, it is possible to engineer entangled states that are simultaneously sensitive to a particular signal of interest and insensitive to the dominant noise source [83]. In this chapter, we describe a Ramsey experiment that uses such a state, composed of two entangled ^{40}Ca$^+$, to provide empirical bounds on potential violations of local Lorentz symmetry – improving the previous bounds by a factor of two to four [68]. In addition to this improvement, a comparison of this work with a similar experiment that was previously performed [80] using two unentangled ^{40}Ca$^+$ provides a real-world case study on how entanglement can be leveraged to improve the sensitivity of precision measurements. We find that entanglement fundamentally improves the frequency sensitivity of the experiment by approximately a factor of two, matching theoretical predictions.

6.2 Violations of local Lorentz invariance

Local Lorentz invariance (LLI) is a fundamental assumption of relativity, requiring that the laws of physics remain unchanged when transforming from one local, inertial frame of reference to another. Nonetheless, some modern theories aimed at resolving remaining inconsistencies in our understanding of nature, such as the unification of general relativity and the standard model, suggest that Lorentz invariance may be broken at high enough energies. For example, energies approaching the Planck scale [57, 56, 79]. Motivated by these results, experimental efforts to push the already stringent experimental bounds set on Lorentz invariance remain an active area of research.

If the LLI of an electron is violated, then this would manifest as a dependence of its dispersion relation on its orientation in space-time. If LLI violations indeed become relevant near the Planck scale, then one might expect that the fractional shift of the electron dispersion should be given by the ratio of the electroweak and Planck energy scales, which is on the order of 10^{-17} [56]. Thus, it is possible for low-energy systems with extraordinary spectroscopic sensitivity to probe for such violations.

Trapped ions can be used for this purpose [80, 68]. The basic idea is as follows. An ion is prepared in a superposition of two anisotropic electronic orbitals with distinct spatial orientations as defined by an applied magnetic field. As the Earth rotates relative to some fixed frame, usually taken to be the Sun, so too does the magnetic field and, with it, the orientation of these orbitals. Thus, a hypothetical LLI violation should result in a periodic modulation of the energy difference between the atomic orbitals that is commensurate with the sidereal day. Using Ramsey spectroscopy, this energy difference can be measured allowing one to observe such a periodic energy variation if present or, if absent, bound it at the limits of the sensitivity of the experiment.

The energy difference between the electronic orbitals due to LLI violations can be computed according to the Standard Model Extension (SME) [57], a theoretical framework that extends the standard model by allowing for all possible LLI violations that do not also violate any other fundamental symmetries. In the nonrelativistic limit, the SME predicts that the Hamiltonian of the electron should be perturbed by the Hamiltonian [46, 56, 80]:

$$\delta \hat{H} = -C_0^{(2)} \frac{\hat{p}^2 - 3\hat{p}_z^2}{6m_e} \tag{6.1}$$

where m_e is the electron mass, $\hat{p}$ is its total momentum and $\hat{p}_z$ is the projection of its momentum along the applied magnetic field. The quantity $C_0^{(2)}$ is a spherical tensor defined in the laboratory frame that characterizes the magnitude of the LLI violation [46] and is what we aim to measure through experiment.

Labeling the cartesian components of $C_0^{(2)}$ in the laboratory frame with lowercase letters, the effect of the Hamiltonian in Equation 6.1 on the $D_{5/2}$ fine structure level $^{40}\text{Ca}^+$ is to induce a direction-dependent energy shift of [80]:

$$f_{LLI} = \frac{E_{LLI}}{h} = C_0^{(2)}[2.16 \times 10^{15} - 7.42 \times 10^{14} m_J^2] \text{ Hz} \tag{6.2}$$

$$= -8.9(2) \times 10^{15}(C_{xx} + C_{yy} - 2C_{zz}) \text{ Hz} \tag{6.3}$$

Note that the quadratic dependence of E_{LLI} on m_J, the projection of the valence electron's angular momentum on the magnetic field. This will be an important feature when we consider decoherence free states in the following sections. Finally, we point out that the transitions[1] $|D_{\pm 1/2}\rangle \leftrightarrow |D_{\pm 5/2}\rangle$ experience the maximum frequency shift under $\delta \hat{H}$ and, so, are most useful for spectroscopy.

---

[1]Here, and for what follows, we will only consider D states that belong to the $D_{5/2}$ manifold. So, without ambiguity, we will use the shorthand $|D_{m_J}\rangle \equiv |D_J, m_J\rangle$.

It is conventional to transform the tensor $C_0^{(2)}$ into a standard reference frame for ease of comparison with other experiments. The sun-centered celestial equatorial frame (SCCEF), which is centered on the sun, is typically used for this purpose. In the SCCEF, f_{LLI} in Equation 6.2 is transformed into

Labeling the cartesian components of the SCCEF with capital letters, the frequency shift for the two ions that we will use for the experiment is given by [46]:

$$f_{LLI}^{\text{SCCEF}} = A\cos(T) + B\cos(T) + C\cos(2T) + D\sin(2T) \tag{6.4}$$

where T is the time measured since the vernal equinox and the coefficients A, B, C and D depend on the colatitude at which the experiment is performed, the direction of the applied magnetic field and the components C_{MN} of the tensor $C_0^{(2)}$ expressed in the laboratory frame (which we distinguish from the lab frame coordinates through the use of the capital letters). In our experiment, we will fit our experimental data to the function in Equation 6.4 to obtain bounds on the components C_{MN}, which translates to bounds on any hypothetical space-like LLI violations of the electron.

6.3 Entanglement enhanced metrology

Ramsey spectroscopy is used to measure the frequency difference $\omega_\Delta = (E_\uparrow - E_\downarrow)/\hbar$ between two fiducial quantum states $|\downarrow\rangle$ and $|\uparrow\rangle$ that can be prepared, controlled and measured with high fidelity. The technique proceeds as follows. After initializing the system in the state $|\Psi\rangle = |\downarrow\rangle$, a $\pi/2$-pulse[2] is used to prepare the superposition:

$$|\Psi\rangle = |\downarrow\rangle \xrightarrow{R_Y(\pi/2)} (|\downarrow\rangle + |\uparrow\rangle)/\sqrt{2} \tag{6.5}$$

The state $|\Psi\rangle$ is then allowed to freely evolve for a time τ, at which point ω_Δ has been written onto an integrated phase difference $\varphi = \omega_\Delta \tau$ between the two branches of the superposition:

$$|\Psi\rangle \xrightarrow[\tau]{\text{free evolution}} (|\downarrow\rangle + e^{-i\varphi(\tau)}|\uparrow\rangle)/\sqrt{2} \tag{6.6}$$

A final $\pi/2$-pulse with a phase ϕ_L relative to the first maps the frequency information onto the populations of the fiducial states:

$$|\Psi\rangle \xrightarrow{R_{\phi_L}(\pi/2)} \sqrt{P_\downarrow}|\downarrow\rangle + e^{-i\phi_L}\sqrt{P_\uparrow}|\uparrow\rangle \tag{6.7}$$

where the probability of measuring the states $|\downarrow\rangle$, $|\uparrow\rangle$ are given respectively by:

---

[2]see Section 3.5.

$$P_\downarrow = \frac{1}{2}\left[1 + \cos\left(\varphi(\tau) + \phi_L\right)\right] \tag{6.8}$$

$$P_\uparrow = \frac{1}{2}\left[1 - \cos\left(\varphi(\tau) + \phi_L\right)\right] = 1 - P_\downarrow \tag{6.9}$$

An estimate of the frequency ω_Δ (modulo 2π) can be extracted from population measurements with an uncertainty of:

$$|\delta\omega_\Delta| = \frac{\delta P_\downarrow}{|dP_\downarrow/d\omega_\Delta|} \tag{6.10}$$

If the Ramsey procedure is repeated M times on N independent, but identically prepared, subsystems then, choosing ϕ_L such as to minimize Equation 6.10, one can derive the optimal frequency uncertainty of $|\delta\omega_\Delta|_{\min} = (MN)^{-1/2}\tau^{-1}$. Or, equivalently, a fundamental frequency sensitivity of $S = 1/|\delta\omega_\Delta|_{\min} = \sqrt{MN}\tau$. The scaling of the minimum uncertainty with $1/\tau$ is a consequence of the time-energy uncertainty relation [11]. The scaling with $1/\sqrt{N}$ is due to the statistical independence of the measurements performed on each subsystem and is often termed the Standard Quantum Limit (SQL) [49].

In theory, entanglement can be used to enhance the frequency sensitivity of this experiment [11]. Rather than preparing the N subsystems into uncorrelated superpositions, one can prepare the maximally entangled N-particle state:

$$|\Psi_N\rangle = \left(\otimes_{i=1}^{N}|\downarrow\rangle + \otimes_{i=1}^{N}|\uparrow\rangle\right)/\sqrt{2} \tag{6.11}$$

Under free evolution, this state picks up an integrated relative phase of $N\varphi$:

$$|\Psi_N\rangle = \left(\otimes_{i=1}^{N}|\downarrow\rangle + e^{-iN\varphi(\tau)}\otimes_{i=1}^{N}|\uparrow\rangle\right)/\sqrt{2} \tag{6.12}$$

Effectively amounting to an amplification of the frequency signal by a factor of N. This phase can be extracted by simultaneously performing $\pi/2$-pulse on each subsystem and then measuring the joint observable:

$$\hat{\Pi}_N = \bigotimes_{i=1}^{N} \hat{\sigma}_z \tag{6.13}$$

where $\hat{\sigma}_z = |\downarrow\rangle\langle\downarrow| - |\uparrow\rangle\langle\uparrow|$ is defined in the usual way.

The expectation value $\Pi_N = \langle\hat{\Pi}_N\rangle$ is the parity signal discussed in Section 3.6. Thus, we will refer to the combination of $\pi/2$-pulses and the evaluation of Π_N as a single parity measurement. It can be verified directly, that the action of the global $\pi/2$-pulse is to map the states $|+\rangle$, $|-\rangle$:

$$|\pm\rangle = \left(\otimes_{i=1}^{N} |\downarrow\rangle \pm \otimes_{i=1}^{N}|\uparrow\rangle \right)/\sqrt{2} \tag{6.14}$$

to states of even and odd parity, respectively. It follows that the probability of measuring a state with positive parity at the end of the experiment is given by:

$$\Pi_N = \cos\left(N[\varphi(\tau) + \phi_L] \right) \tag{6.15}$$

On the other hand, the quantum projection noise corresponding to the probability of measuring a state with even parity is functionally equivalent to $\delta P_\downarrow$. Therefore, the frequency sensitivity of the entangled Ramsey spectrometer is given by $S = \sqrt{M}N\tau$, a $\sqrt{N}$ improvement over the SQL – a fact which has been verified by experiment [45, 74, 69, 59]. The linear scaling of sensitivity with N is often referred to as the Heisenberg Limit (HL).

In practice, it is difficult to translate Heisenberg limited spectroscopy into any actual metrological gain. This is because real systems are inevitably subject to noise that causes random fluctuations of the frequency splitting between the branches of the Ramsey superposition. These fluctuations are integrated into the Ramsey phase such that the effect tends to grow with the interrogation time τ, resulting in a reduced Ramsey oscillation contrast. For example, the cosine terms in Equation 6.8 must be prepended by a scale factor $A(\tau)$, which will generally tend towards zero with τ. This reduces the value of the denominator in Equation 6.10, increasing the frequency uncertainty. Thus, an optimal measurement time emerges that makes the trade-off between longer interrogation times that are more sensitive to the signal of interest and shorter interrogation times that are less susceptible to noise.

Unfortunately, the same mechanism that lends itself to the phase amplification for the entangled system also tends to amplify the effect of the noise. Therefore, the optimal measurement time for the entangled Ramsey spectrometer will generally be shorter than for the non-entangled system. To make a fair comparison of the corresponding sensitivities, we consider a total measurement duration T, during which $M = T/\tau$ repeated experiments can be performed, then we have:

$$S_{\text{uncorrelated}} = \sqrt{NT\tau_{\text{uncorrelated}}} \tag{6.16}$$

$$S_{\text{entangled}} = N\sqrt{T\tau_{\text{entangled}}} \tag{6.17}$$

where the τ_i refer to the optimal measurement times for the two different cases. Since $\tau_{\text{entangled}}/\tau_{\text{uncorrelated}}$ is expected to decrease as a function of N, the benefit of using entanglement is brought into question. In fact, for many plausible noise models, such as when the frequency fluctuations can be described as a white noise process [48], we find that $\tau_{\text{entangled}}/\tau_{\text{uncorrelated}} = 1/N$, exactly negating the enhancement from the phase amplification and reducing the scaling of the entangled system's performance to the SQL.

However, under certain circumstances, it is possible to create a set of entangled states that are impervious to the effects of specific noise – a so-called Decoherence Free Subspace

(DFS) [61, 62]. For example, if the noise is global such that its effect on each subsystem is identical, then any linear combination of states that are degenerate energy eigenstates of the Hamiltonian governing the noise source will belong to such a DFS. In some cases, given a heterogeneous collection of two-level systems, it is possible to construct an entangled two-level subspace that is decoherence-free with respect to the dominant noise source while, at the same time, sensitive to the signal of interest. For example, given two co-trapped $^{40}\text{Ca}^+$ ions it is possible to prepare the state [83]:

$$|\Psi_{\text{DFS}}\rangle = (|D_{-1/2}\rangle|D_{+1/2}\rangle + e^{i\phi}|D_{-5/2}\rangle|D_{+5/2}\rangle)/\sqrt{2} \tag{6.18}$$

The component states of $|\Psi_{\text{DFS}}\rangle$ are degenerate with respect to the Zeeman Hamiltonian (Equation 2.62) since the Zeeman energy depends linearly on the value of m_J. On the other hand, they are non-degenerate under the Hamiltonian describing LLI violations (Equation 6.2) since this energy shift depends only on m_J^2

In the following two sections we will describe how, by using a two-ion entangled state of the form in Equation 6.18, we can enhance the spectroscopic sensitivity of a real-world measurement, when compared to an analogous experiment performed with two unentangled ions. In Section 6.4 we will discuss how comparing the spectroscopic sensitivities between these two cases is complicated by the fact that the unentangled system is no longer uncorrelated. Instead, the global nature of the magnetic field noise results in a measurable correlation between the two unentangled ions, which persists long after the single-ion Ramsey states have decohered. Nonetheless, we will find that the use of entangled two-ion states results in a fundamental enhancement in the spectroscopic sensitivity by a factor of two – exceeding even the $N^{1/2}$ improvement predicted when going from the SQL to the HL. In the final section of this chapter, we will describe experimental results that verify this improvement.

6.4 Spectroscopy with classically correlated $^{40}\text{Ca}^+$ ions

Following the procedure outlined in Section 6.3, we can perform Ramsey spectroscopy on two unentangled $^{40}\text{Ca}^+$ ions, each prepared in the state:

$$|\Psi_-\rangle = (|D_{-1/2}\rangle + |D_{-5/2}\rangle)/\sqrt{2} \tag{6.19}$$

which can be prepared via the following sequence of laser pulses:

$$|S_{-1/2}\rangle \xrightarrow{R_Y^A(\pi/2)} (|S_{-1/2}\rangle + |D_{-5/2}\rangle)/\sqrt{2}$$
$$\xrightarrow{R_Y^B(\pi)} (|D_{-1/2}\rangle + |D_{-5/2}\rangle)/\sqrt{2} \tag{6.20}$$

where the superscripts A and B on the rotation operators denote a laser pulse that addresses either the transition $|S_{-1/2}\rangle \leftrightarrow |D_{-5/2}\rangle$ or $|S_{-1/2}\rangle \leftrightarrow |D_{-1/2}\rangle$, respectively.

The state $|\Psi_-\rangle$ is sensitive to both potential violations of local Lorentz invariance as well as the local magnetic field, each contributing to a shift in the frequency splitting between the two component states of the superposition. Thus, after an interrogation time of τ, the state $|\Psi_-\rangle$ will pick up a Ramsey phase:

$$|\Psi_-\rangle \xrightarrow[\tau]{\text{free evolution}} (|D_{-1/2}\rangle + e^{-i(\varphi_B + \varphi_{LLI})}|D_{-5/2}\rangle)/\sqrt{2} \tag{6.21}$$

where we have explicitly separated the contribution to the phase from Lorentz invariance violations φ_{LLI} and from the Zeeman effect φ_B. Per Equation 6.16, the sum of these frequencies can be measured with an uncertainty of $(2M)^{-1/2}\tau^{-1}$ where M corresponds to the number of repetitions of the experiment. The factor of $1/\sqrt{2}$ comes from the fact that measurements are performed on two independent ions.

The sensitivity of this approach is damped by the strong magnetic field fluctuations present in the vicinity of the ions. These cause a frequency jitter that uniformly randomizes the Ramsey phase (modulo 2π) in a time on the order of several milliseconds (see Figure 5.3), limiting the interrogation time τ to a small value. On the other hand, if we can assume that the magnetic field experienced by both ions is identical, then this implies that even long after the individual population oscillations of each ion have been washed out, finite correlations will persist in the joint populations. We can see this by performing an inversion of the pulse sequence in Equation 6.20 and computing the expectation value of the parity operator, which is equivalent, in this case, to the covariance of $\hat{\sigma}_z^{(1)} \otimes \hat{\sigma}_z^{(2)}$:

$$\Pi = \text{cov}(\hat{\sigma}_z^{(1)}, \hat{\sigma}_z^{(2)}) = P_{SS} + P_{DD} - P_{SD} - P_{DS} = \frac{1}{2} \tag{6.22}$$

where the subscripts S and D refer to the states $S_{-1/2}$ and $D_{-5/2}$, respectively, and we have used Equations 6.8 and 6.9 to compute the terms in Equation 6.22. For example, assuming $\phi_L = 0$ since it does not affect the calculation:

$$\begin{aligned}
P_{SS} = P_S \cdot P_S &= \left\langle \frac{1}{4}\left(1 + \cos(\varphi_B + \varphi_{LLI})\right)^2 \right\rangle_{\varphi_B} \\
&= \frac{1}{4}\left[1 + 2\left\langle \cos(\varphi_B + \varphi_{LLI})\right\rangle_{\varphi_B} + \left\langle \cos^2(\varphi_B + \varphi_{LLI})\right\rangle_{\varphi_B}\right] \\
&= \frac{3}{8}
\end{aligned} \tag{6.23}$$

Here the angle brackets indicate averaging over φ_B, which we assume is uniformly random modulo 2π. Similar calculations give $P_{DD} = 3/8$ and $P_{SD} = P_{DS} = 1/8$ such that $\Pi = 1/2$, as stated in Equation 6.22.

The finite value of the parity/covariance $\text{cov}(\hat{\sigma}_z^{(1)}, \hat{\sigma}_z^{(2)})$ indicates that measurements of joint observables of the two ions might reveal some information about the signal of interest φ_{LLI}. But the example calculation in Equation 6.23 suggests that it will be difficult to

differentiate φ_{LLI} from φ_B since they both contribute to the total phase in a similar way. We can remedy this by preparing one of the ions in the state:

$$|\Psi_+\rangle = (|D_{+1/2}\rangle + |D_{+5/2}\rangle)/\sqrt{2} \tag{6.24}$$

such that the total wavefunction is given by the product state:

$$|\Psi_\pm\rangle = \frac{1}{2}|\Psi_-\rangle \otimes |\Psi_+\rangle = \frac{1}{2}(|D_{-1/2}\rangle + |D_{-5/2}\rangle) \otimes (|D_{+1/2}\rangle + |D_{+5/2}\rangle) \tag{6.25}$$

The Zeeman shift between the states in $|\Psi_+\rangle$ has the same magnitude but opposite sign of the Zeeman shift affecting the states in $|\Psi_-\rangle$. This results in a distinguishable effect between the negative correlation of the two ions due to the random φ_B and the positive correlation due to φ_{LLI}. The parity signal for Ramsey spectroscopy performed with the state $|\Psi_\pm\rangle$ is given by:

$$\Pi = \frac{1}{2}\cos(2\varphi_{LLI}) \tag{6.26}$$

Interestingly, the phase of this signal is amplified by a factor of two, the same factor that would occur for an entangled state. According to Equation 6.17, this leads to a factor of $\sqrt{2}$ increase in the frequency sensitivity. However, the contrast of the signal is also reduced by a factor of two. And, according to Equation 6.10, the sensitivity scales linearly with contrast. Thus, the overall frequency sensitivity of this method is equal to $(M)^{-1/2}\tau^{-1}$, which is the same as for a Ramsey measurement performed on a single ion in the absence of magnetic field noise. An experimental measurement of this signal is presented in Figure 6.1.

An alternative approach to deriving the result in Equation 6.26 begins by rewriting the product state $|\Psi_\pm\rangle$ in the basis $\{|\pm\rangle, |\pm'\rangle\}$:

$$|+\rangle = (|D_{-1/2}\rangle|D_{+1/2}\rangle + |D_{-5/2}\rangle|D_{+5/2}\rangle)/\sqrt{2} \tag{6.27}$$

$$|-\rangle = (|D_{-1/2}\rangle|D_{+1/2}\rangle - |D_{-5/2}\rangle|D_{+5/2}\rangle)/\sqrt{2} \tag{6.28}$$

$$|+'\rangle = (|D_{-1/2}\rangle|D_{+5/2}\rangle + |D_{-5/2}\rangle|D_{+1/2}\rangle)/\sqrt{2} \tag{6.29}$$

$$|-'\rangle = (|D_{-1/2}\rangle|D_{+5/2}\rangle - |D_{-5/2}\rangle|D_{+1/2}\rangle)/\sqrt{2} \tag{6.30}$$

If we first ignore the effects of magnetic field noise, then after a Ramsey interrogation time of τ the density matrix of $\rho_\pm = |\Psi_\pm\rangle\langle\Psi_\pm|$ is given in this basis by:

$$\rho_\pm = \frac{1}{2} \times$$

$$
\begin{array}{cccc}
|+\rangle & |-\rangle & |+'\rangle & |-'\rangle
\end{array}
$$

$$
\begin{pmatrix}
\cos^2(2\varphi_{LLI}) & \cos(2\varphi_{LLI})\sin(2\varphi_{LLI}) & 0 & 0 \\
\cos(2\varphi_{LLI})\sin(2\varphi_{LLI}) & \sin^2(2\varphi_{LLI}) & 0 & 0 \\
0 & 0 & \cos^2(2\varphi_{LLI}+2\varphi_B) & \cos(2\varphi_{LLI}+2\varphi_B)\sin(2\varphi_{LLI}+2\varphi_B) \\
0 & 0 & \cos(2\varphi_{LLI}+2\varphi_B)\sin(2\varphi_{LLI}+2\varphi_B) & \sin^2(2\varphi_{LLI}+2\varphi_B)
\end{pmatrix}
\begin{array}{c}
|+\rangle \\ |-\rangle \\ |+'\rangle \\ |-'\rangle
\end{array}
$$

$$(6.31)$$

Magnetic field noise can then be incorporated by averaging Equation 6.31 over φ_B to obtain the mixed state:

$$\langle \rho_\pm \rangle_{\varphi_B} =$$

$$
\begin{array}{cccc}
|+\rangle & |-\rangle & |+'\rangle & |-'\rangle
\end{array}
$$

$$
\frac{1}{2}
\begin{pmatrix}
\cos^2(2\varphi_{LLI}) & \cos(2\varphi_{LLI})\sin(2\varphi_{LLI}) & 0 & 0 \\
\cos(2\varphi_{LLI})\sin(2\varphi_{LLI}) & \sin^2(2\varphi_{LLI}) & 0 & 0 \\
0 & 0 & \frac{1}{2} & 0 \\
0 & 0 & 0 & \frac{1}{2}
\end{pmatrix}
\begin{array}{c}
|+\rangle \\ |-\rangle \\ |+'\rangle \\ |-'\rangle
\end{array}
$$

$$(6.32)$$

The interpretation of the result in Equation 6.32 is as follows. After some time t that is short relative to τ but longer than the coherence length of the magnetic field sensitive states $|\pm'\rangle$, it is as if we have randomly prepared the system in the decoherence free subspace $\{|\pm\rangle\}$ with a probability of 1/2. The other half of the time, the system is prepared in an equal mixture of the states $|\pm'\rangle$. Since a global $\pi/2$ rotation maps the triplet-like $|+'\rangle$ to a state with even parity and the singlet-like $|-'\rangle$ to a state with odd parity, together they produce zero net contribution to a subsequent parity measurement.

This analysis makes clear the form of the parity signal derived in Equation 6.26 – in particular, the factor of two amplifying the phase φ_{LLI} and the factor of 1/2 scaling the contrast. Furthermore, it becomes clear that any additional noise source present in the system that does affect a deterministically prepared entangled DFS state will equally affect the classical correlations present in the mixed state in Equation 6.32. Thus, in this case, entanglement provides an unambiguous practical enhancement by a factor of two to the spectroscopic sensitivity of the experiment.

Ramsey spectroscopy performed on the state $|\Psi_\pm\rangle$ is the technique that was used in [80] to derive the previous strongest bound on local Lorentz invariance violations. Following [83], we used this technique to measure the small quadrupole shift[3] of the fine structure levels

---

[3]The orientation of the magnetic field remained constant for all results in this chapter.

$D_{1/2}$ and $D_{5/2}$ that was described in Section 2.5. The results are presented in Figure 6.2. We find that the scaling of this shift with the axial center of mass vibrational frequency goes as -1.5 mHz/kHz near the operating point of $\approx$830 kHz. In addition, we measured the long-term stability of the axial center-of-mass frequency using resonance spectroscopy on a sideband transition and found it to be stable to within a few hundred Hz for over half a day. We will see in Section 6.6, that this signal is too small to contribute to the bounds we set on LLI violations.
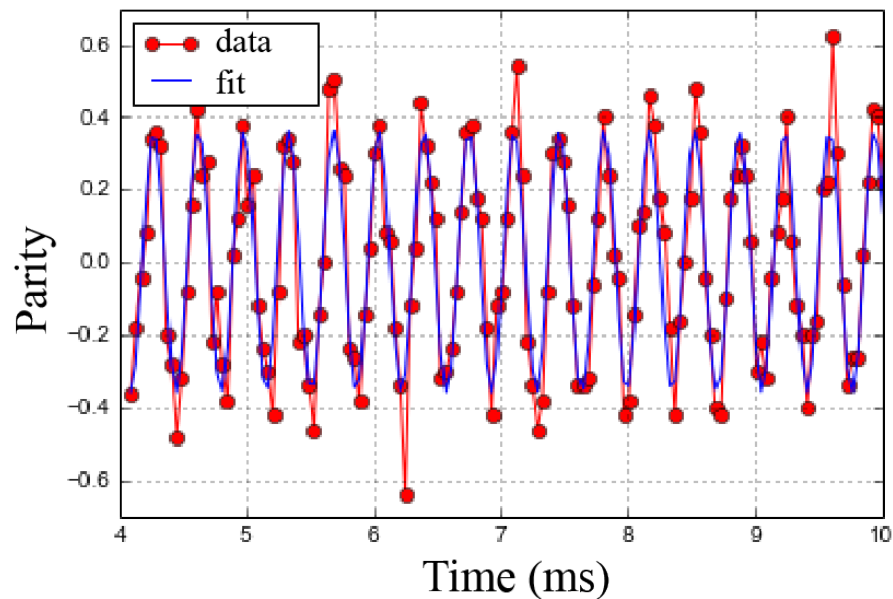
Figure 6.1: Parity measurement of two classically correlated ions. The parity signal is measured as function of interrogation using the state given in Equation 6.25. The red circles correspond to measurements and the blue curve corresponds to a fit to equation 6.26. In this case, the oscillations are due to the small quadrupole shift between the Zeeman levels $|D_{5/2}, \ m_J = 1/2\rangle$ and $|D_{5/2}, \ m_J = 5/2\rangle$ described in Section 2.5.
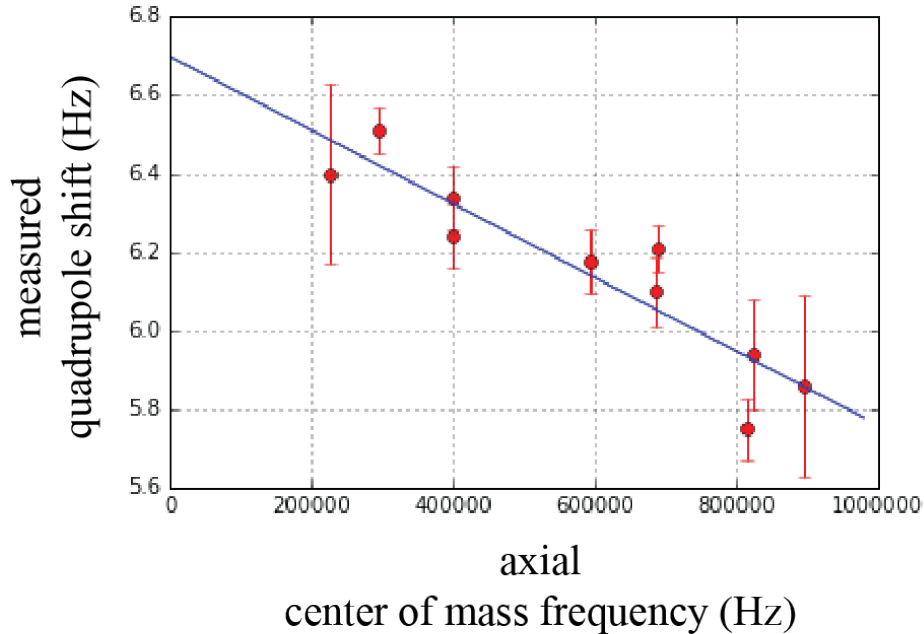
Figure 6.2: Quadrupole shift as a function of axial trap frequency. The circles correspond to measurements of the electric quadrupole shift between the $D_{1/2}$ and $D_{5/2}$ fine structure levels (vertical axis) as a function of the axial center-of-mass trap frequency (horizontal axis) obtained from parity scans similar to the one illustrated in Figure 6.1. The blue curve corresponds to a linear fit with a slope of -1.5 mHz/kHz.

6.5 Spectroscopy with entangled ^{40}Ca$^+$ ions

To prepare the entangled state $|\Psi_{\mathrm{DFS}}\rangle$ in Equation 6.18, we first laser cool both axial vibrational modes of the ions down to near their ground state using sideband cooling (Section 3.3) and then perform the following procedure. First, the two ions are prepared in the state $|S_{-1/2}\rangle|S_{-1/2}\rangle$ via optical pumping (Section 3.4) using global laser beams. Next, a local laser beam focused on only one of the ions[4] is used to optically pump that ion into the state $|S_{+1/2}\rangle$. By driving Rabi oscillations with the local beam and taking the ratio of the square of the frequencies observed on each ion, we estimate that the fractional intensity overlap of local beam onto the second ion is on the order of 10^{-3} (see Figure 6.3). Following optical

---

[4]Using the setup described in Section 4.4.

pumping, a Mølmer-Sørensen (MS) gate, like the one described in Section 3.6, is used to generate the entangled state:

$$|S_{-1/2}\rangle|S_{+1/2}\rangle \xrightarrow{\text{MS}} (|S_{-1/2}\rangle|S_{+1/2}\rangle + |D_{-1/2}\rangle|D_{+1/2}\rangle)/\sqrt{2} \tag{6.33}$$

Finally, two π pulses are used on the transitions $|S_{-1/2}\rangle \leftrightarrow |D_{-5/2}\rangle$ and $|S_{+1/2}\rangle \leftrightarrow |D_{+5/2}\rangle$, which we label as C1 and C2, respectively. Since each of these pulses is resonant with only one of the ions, a global laser beam can be used for this purpose. The final state is as desired:

$$|\Psi_{\text{DFS}}\rangle = (|D_{-1/2}\rangle|D_{+1/2}\rangle + |D_{-5/2}\rangle|D_{+5/2}\rangle)/\sqrt{2} \tag{6.34}$$
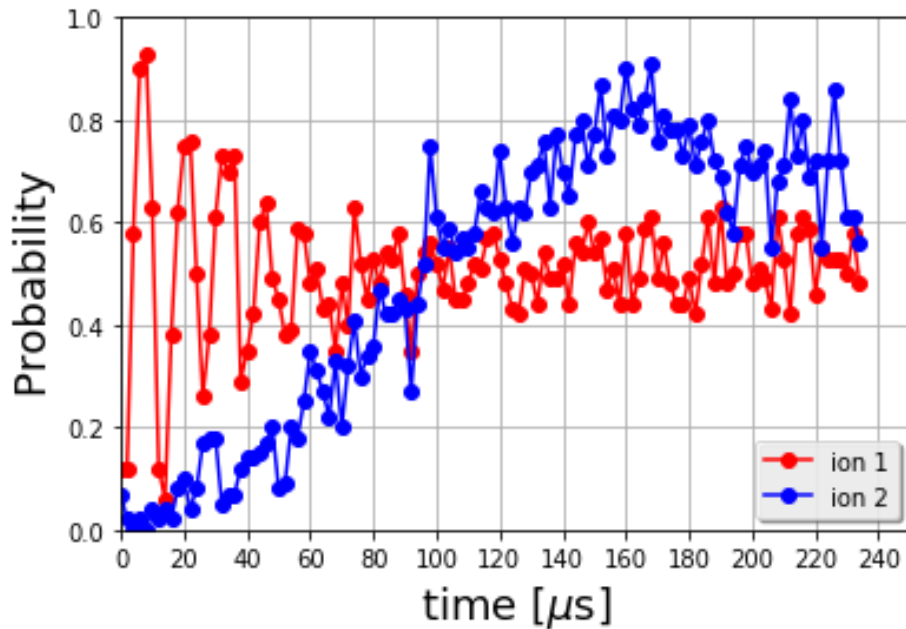
Figure 6.3: Local beam addressing. Both ions are prepared in the state $|S_{-1/2}\rangle|S_{-1/2}\rangle$ and the local beam, focused on only one of the ions, is used to drive Rabi oscillations. The red data corresponds to the oscillations measured on the focused ion. The blue data corresponds to the oscillations measured on the other ion. By taking the squared ratio of the observed oscillation frequencies, we estimate an intensity overlap of about 0.2% of the local beam on the unfocused ion.

Generating the MS interaction for the gate in Equation 6.33 is somewhat complicated by the fact that two separate electronic transitions are involved. This is similar to the case of entangling ions of different species [94, 4]. Two pairs of laser tones are required. The average frequency of each pair is centered on one of the electronic transitions $|S_{-1/2}\rangle \leftrightarrow |D_{-1/2}\rangle$ and $|S_{+1/2}\rangle \leftrightarrow |D_{+1/2}\rangle$, which we label as C3 and C4, respectively. The detuning of each tone in

a pair relative to their center frequency is chosen to be slightly greater than the frequency of the axial center-of-mass mode (by approximately 10 kHz). The transition diagram for this interaction is illustrated in Figure 6.4 (a).
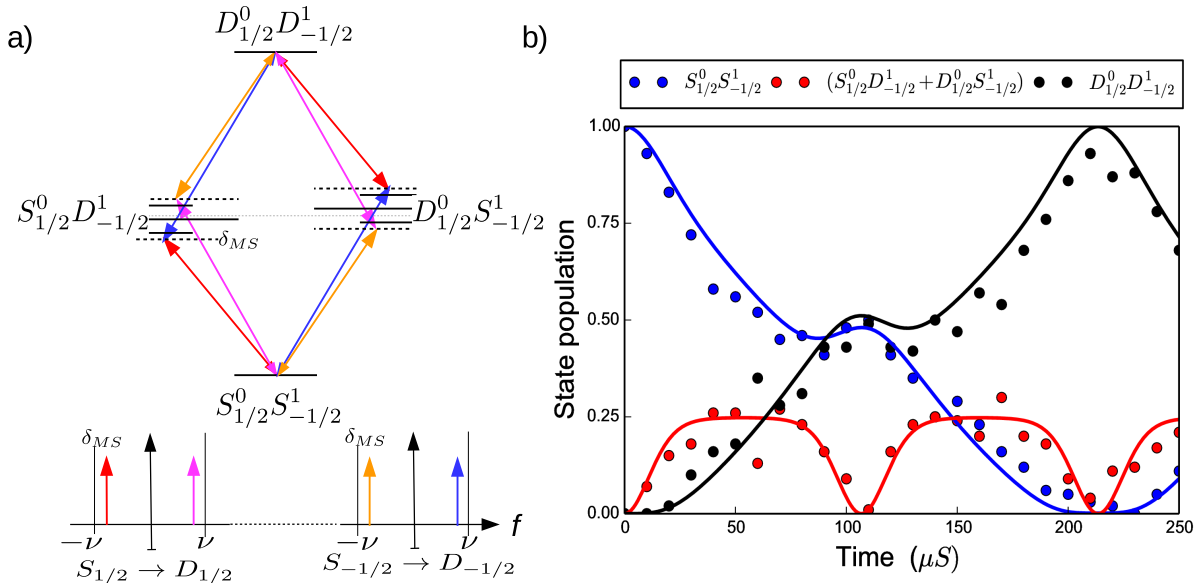
Figure 6.4: Dual carrier Mølmer-Sørensen gate. [68] **(a)** The transition diagram for the dual carrier Mølmer-Sørensen interaction. The axial center of mass frequency is labeled as ν in the lower plot and the detuning of the individual laser tones from the sideband transition frequencies is labeled δ_{MS}. **(b)** Measured population dynamics for the dual-carrier MS interaction. The circles represent experimental data points and the curves represent theory. At a gate time of approximately 100 μs, the fidelity of preparing the state in Equation 6.33 was found to be approximately 94%, which we believe was primarily limited by intensity fluctuations of the addressing laser.

We generate the six laser tones used in the preparation of $|\Psi_{\text{DFS}}\rangle$ using the configuration illustrated in Figure 6.5. In particular, the four tones used for the MS gate are derived from a common laser source using two AOMs with one in a double-pass configuration and the other in a single-pass configuration. In this case, the double-pass is used to write the carrier tones C3 and C4 onto the laser and the single-pass is used to split each one of these into the bichromatic pairs used for the MS. With this setup, in addition to producing the tones C3 and C4, the tone $(C3 + C4)/2$ is also coupled into the final beam. Care must be taken that this frequency is not resonant with any auxiliary transitions.
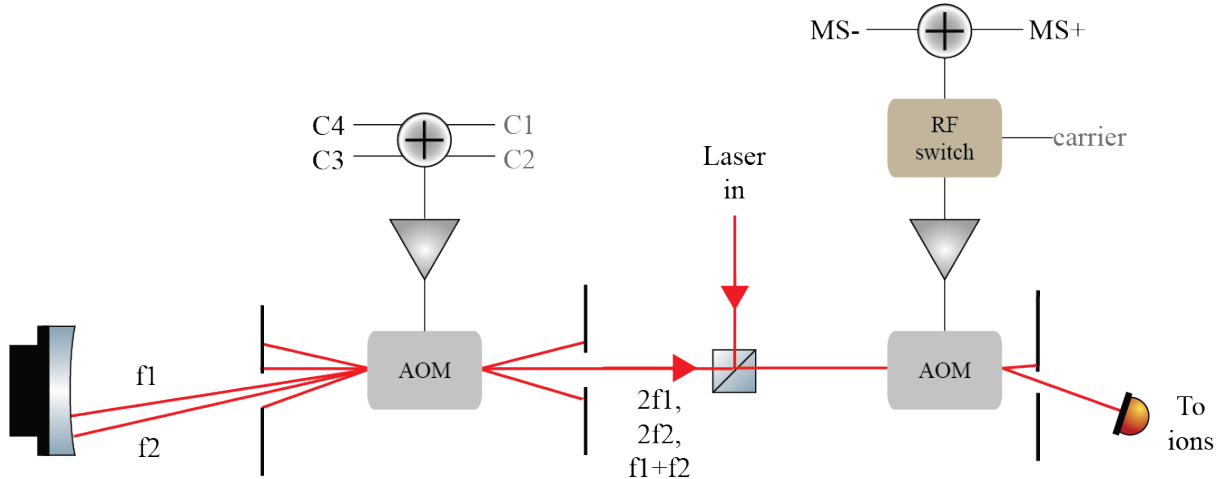
Figure 6.5: Laser control for preparation of an entangled DFS state. The double-pass AOM
on the right is used to write the carrier frequencies C1-C4 onto the laser beam. At most
two of these are driven at any given time, but it is necessary to use four different sources
since the RF sources used cannot switch back and forth between two different frequencies
coherently. Adjustable apertures are used to block unwanted, higher-order tones generated
by the AOMs. However, when the double-pass is simultaneously driven by both C3 and C4,
a tone with a frequency equal to their average will be produced that is too close in frequency
to the carriers to be effectively blocked out. Care must be taken that this frequency is not
resonant with any unwanted transitions in the ion.

When driving the dual-carrier MS interaction, each pair of bichromatic tones causes a
Stark shift of the opposite carrier transition, found empirically to be on the order of several
tens of kHz. To tune up the MS gate, we first prepare both ions in the same electronic
ground state, either $|S_{-1/2}\rangle$ or $|S_{+1/2}\rangle$, and then calibrate the single-carrier MS gate while
still addressing the ions with all four tones. This procedure is then repeated for the other
ground state. With this method, we were able to prepare the state in Equation 6.33 with
a fidelity of approximately 94% as measured using the technique described in Section 3.6.
We believe the primary factor limiting this fidelity was the intensity fluctuations of the laser
light driving the gate dynamics. The fractional size of these fluctuations was measured to
be around 5% using a photodiode placed near the point before the laser enters the chamber.
In addition to affecting the interaction strength of the MS gate (see Section 3.6), these
fluctuations also cause effective frequency noise due to the unbalanced Stark shifts.

To perform Ramsey spectroscopy using $|\Psi_{\mathrm{DFS}}\rangle$, we roughly follow the procedure outlined
in Section 6.3. The exact procedure that we use is illustrated in Figure 6.6 (a) and an
example of the resulting parity measurements is given in Figure 6.6 (b). To account for

drifts in the contrast of the Ramsey signal, we take two independent measurements for each experimental estimate of the Ramsey phase. These phase measurements are offset by 90 degrees as dictated by the phase of the laser light pulse used to drive the final $\pi/2$ rotations. We set the common laser phase offset of the final pulses to bias both of these data points near the zero-crossing of the parity signal where the frequency sensitivity is greatest (Equation 6.10). Once the Ramsey phase has been measured we use this information to update the laser phases for the next measurement so that we are constantly sitting at the optimal bias points.

These updates are necessary because of slow drifts of the absolute phase offset of the Ramsey signal due, for example, to systematic drifts in the laser parameters, which might affect the initial phase between the two branches of the prepared entangled state. To cancel out this effect, we perform the two-point Ramsey measurement at two different waiting times of 5 ms and 100 ms[5]. By computing the relative phase between these two measurements, we can cancel out the effect of any such drifts that can be neglected over the timescale of a single shot of the experiment (on the order of 0.1 seconds). It is evident in Figure 6.6 (b), that the contrast of the parity signal has degraded when going from a 5 to 100 ms wait time. This can primarily be attributed to the spontaneous decay of the ions from the excited $D_{5/2}$ manifold, which has a lifetime of approximately one second (Section 2.3).

Finally, we point out that there is a measurable magnetic field gradient at the position of the ions. This contributes to an energy shift between the components of the DFS state. We find that this gradient is relatively stable over time and believe that it is primarily due to the single permanent magnet that we use to set our quantization axis. Nonetheless, we cancel out this effect by performing two sets of experiments where the states of the ions are swapped. We label these states:

$$|\Psi_R\rangle = (|D_{+1/2}\rangle|D_{-1/2}\rangle + |D_{+5/2}\rangle|D_{-5/2}\rangle)/\sqrt{2} \tag{6.35}$$

$$|\Psi_L\rangle = (|D_{-1/2}\rangle|D_{+1/2}\rangle + |D_{-5/2}\rangle|D_{+5/2}\rangle)/\sqrt{2} \tag{6.36}$$

The effect of the magnetic field gradient on these two states is equal in magnitude but opposite in sign. Thus, by taking the average of the phase estimated for both configurations we cancel out this effect.

In summary, a single estimate of the energy difference between the components of the DFS state due to a hypothetical LLI violation consists of eight individual measurements. A single two-point measurement was performed at two separate wait times and repeated for both of the states $|\Psi_R\rangle$ and $|\Psi_L\rangle$. Altogether, this amounts to a total measurement time of roughly 40 seconds. In the final section of this chapter, we will describe how we used measurements like these to place an improved bound on LLI violations.

---

[5]The difference of these waiting times is chosen to be commensurate with the period of the 60 Hz to integrate out any remaining systematic effects due to fluctuations in the magnetic field from the power lines.
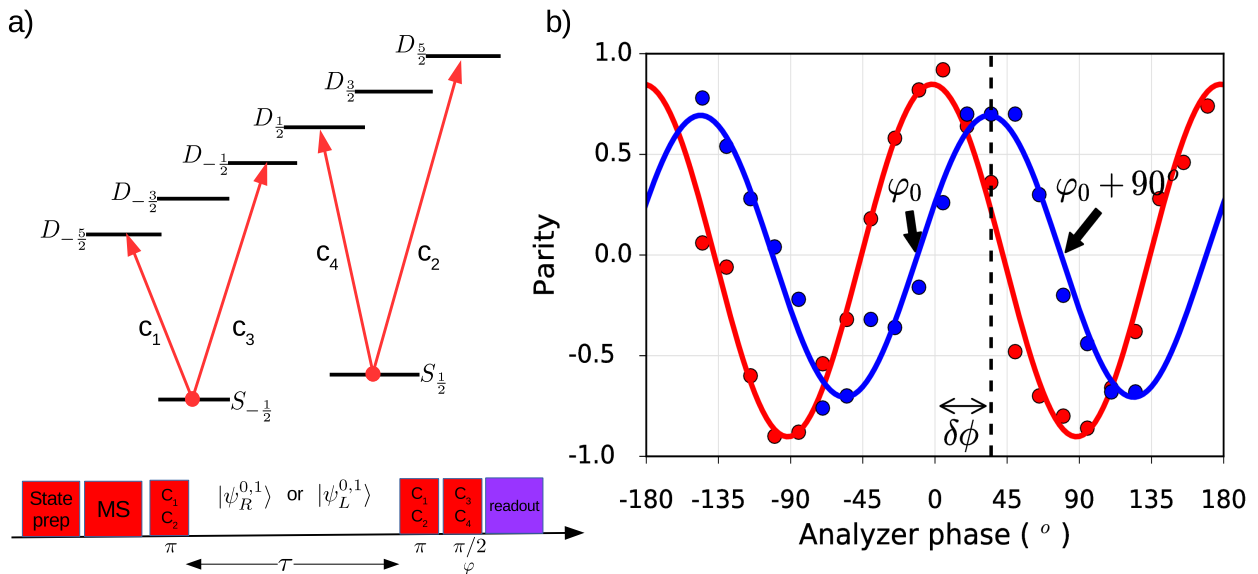
Figure 6.6: Entangled Ramsey spectroscopy. **(a)** The experimental pulse sequence. **(b)** Parity measurements were performed at 5 ms (red) and 100 ms (blue) waiting times. In practice, we measure only two points of the Ramsey fringe to extract both the phase φ_0 and the contrast. By varying the phase of the final $\pi/2$-pulses, we can bias the Ramsey oscillations such that these points are taken near the zero-crossing of the parity signal where the sensitivity is greatest (near the points of greatest slope). Using the phase estimates measured at each waiting time, we can determine the relative phase shift $\delta\phi$, eliminating the effect of any slow drifts. [68]

6.6 Results

Using the Ramsey scheme outlined in the previous section, we, more or less, continuously monitored the frequency splitting between the component states of $|\Psi_{\text{DFS}}\rangle$ over four days. The experimental results are plotted in the bottom frame of Figure 6.7. After every ten minutes of measurement time, we performed independent measurements of the carrier frequencies and the magnetic field magnitude and then used these results to optimize the performance of the pulse sequence. Measured deviations of the magnetic field strength from its mean are plotted in the top frame of Figure 6.7.

Other than drifts in the offset of the Ramsey phase and the presence of a finite magnetic field gradient – both of which are nullified by the measurement scheme – the only other known systematics that might affect the estimation of LLI violation at the limits of the sensitivity of the experiment are the quadratic Zeeman shift and the electric quadrupole shift. The quadratic Zeeman shift can be calculated as a function of the magnetic field strength [92]
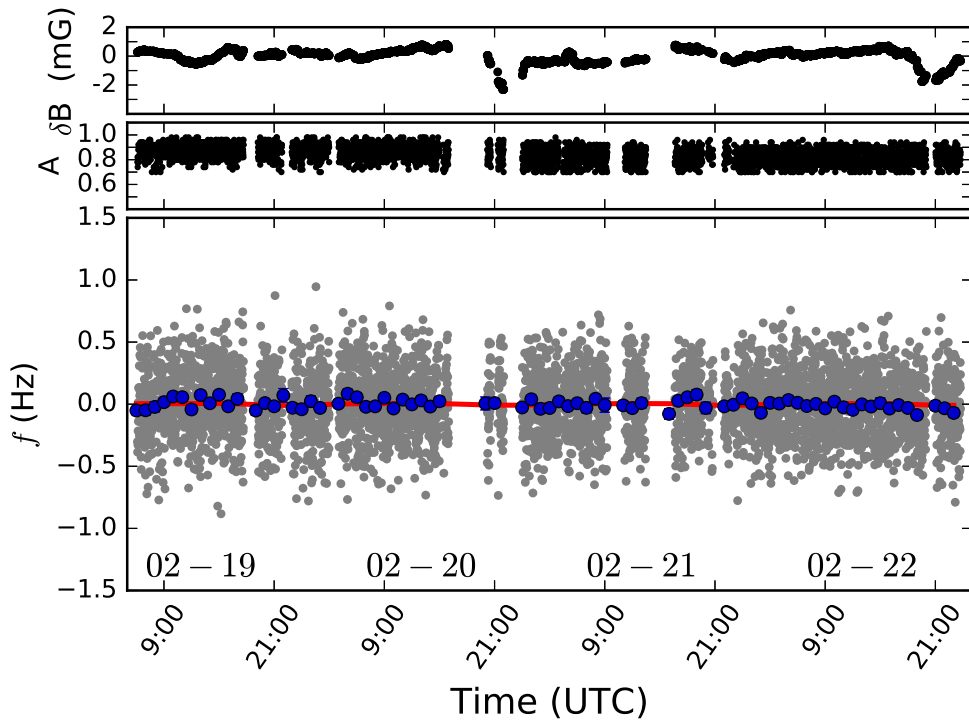
Figure 6.7: Measurements of the energy difference between the $|D_{-1/2}\rangle|D_{+1/2}\rangle$ and $|D_{-5/2}\rangle|D_{+5/2}\rangle$ states of ^{40}Ca$^+$. Here we plot our experimental measurements of the magnetic field, Ramsey contrast, and frequency splitting of the $|D_{-1/2}\rangle|D_{+1/2}\rangle$ and $|D_{-5/2}\rangle|D_{+5/2}\rangle$ states over roughly four days. The gray circles in the bottom frame represent the raw frequency data. The blue circles represent the same data binned in one-hour intervals. The red curve is a fit to Equation 6.4. [68]

and scales approximately as 4.5 mHz/mG. Using the measured values of the magnetic field, we apply a correction to our frequency estimates based on this calculation. On the other hand, based on the results in Section 6.4, the electric quadrupole shift is expected to vary, through drifts in the axial trapping potential, by several tenths of a mHz over the full-time scale of our measurements. Based on the bottom frame of Figure 6.7 it seems reasonable to suspect that these fluctuations can be ignored. This is confirmed in the full calculation of the bounds on C_{MN}, where we find that the inclusion of these fluctuations does not impact, to order-of-magnitude, the uncertainty of our estimates on these parameters (obtained by fitting the measured data to Equation 6.4).

To derive bounds on LLI violations from our data, we fit it to Equation 6.4 and translate the fitted values and associated uncertainty into the components C_{NM} described in Section 6.2. This translation requires a value for the orientation of the magnetic field in the

laboratory frame. We determine that the magnetic field is oriented parallel to the surface of the Earth with an angle of approximately $68°$ east of true north by performing excitation spectroscopy on several different $S_{1/2} \leftrightarrow D_{5/2}$ transitions and taking advantage of the dependency of their coupling strengths on the direction and polarization of the addressing laser relative to the orientation of the magnetic field (Section 2.6). Using this calculation we find that, on average, we improve the bounds on LLI violations to about 5×10^{-19}, which represents about a half an order of magnitude improvement over the previous best bounds [80]. The specific bounds on the C_{MN} components that we derived can be found in Table 1 of [68].

To compare the performance of Ramsey spectroscopy using two entangled DFS states with the performance of two classically correlated states [80], we compute the Allan deviation for both experiments and plot the results in Figure 6.6. Roughly speaking, the Allan deviation is a measurement of the variance of the frequency estimate as a function of total measurement duration τ. One should assume that for longer τ, more independent measurements of the frequency can be taken and their average can be used to produce a more precise frequency estimate. However, this assumption will fail if additional systematics, unaccounted for in the analysis, cause drifts in the underlying sample distribution. As shown in Figure 6.6, for both the case of two unentangled and two entangled ions, the Allan deviation is well fit as a function of $1/\sqrt{\tau}$, revealing no evidence of correlated noise or systematics over the full duration of the experiments. Furthermore, these results reveal that for the entangled state the frequency uncertainty scales as $1.72 \text{ Hz}/\sqrt{\tau}$, whereas for the mixed state, it scales as $3.54 \text{ Hz}/\sqrt{\tau}$. Thus, the entangled state outperforms the mixed state by roughly a factor of two, matching the prediction computed in Section 6.3 and demonstrating that, under certain circumstances, entanglement can enhance the spectroscopic sensitivity of real-world measurements.
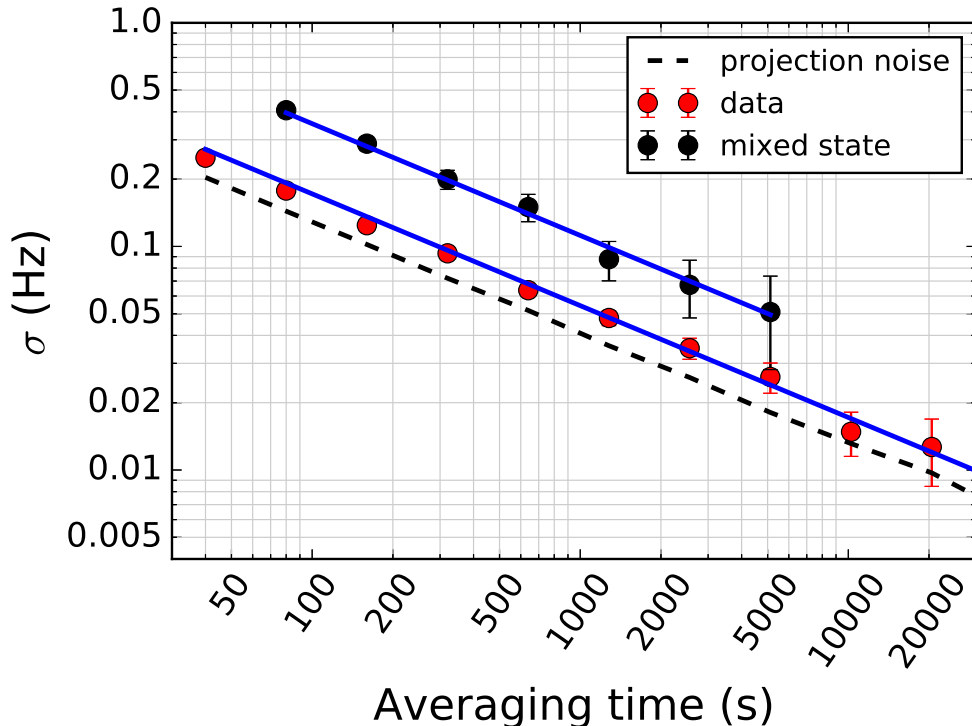
Figure 6.8: Allan deviation [68] The black circles represent the Allan deviation corresponding
to frequency measurements taken using two classically correlated ions [80]. The red circles
represent the Allan deviation corresponding to the unbinned frequency measurements taken
in this work and summarized in Figure 6.7 using a deterministically prepared entangled state.
The blue lines represent fits to the data from which we find that $\sigma = 1.72$ Hz$/\sqrt{\tau}$ and $\sigma =$
3.53 Hz$/\sqrt{\tau}$ for the entangled and mixed states, respectively. The factor of two improvements
in frequency uncertainty achieved by the entangled state matches the theoretical predictions
derived in Section 6.3 and demonstrates the viability of using entanglement to enhance
precision measurements in real-world systems. The dashed line represents the ideal case of
an entangled state limited only by quantum projection noise.

Chapter 7

Conclusion

In this thesis, we have presented the results of two experiments that used well-controlled quantum systems composed of trapped ^{40}Ca$^+$ ions to perform precise tests, with unprecedented sensitivity, of physical theories predicting novel phenomena. In both cases, by failing to observe any such phenomena, we have set more stringent empirical bounds on these theories. In this chapter, we will summarize these results and provide some outlook on the prospect of future work.

Test of causal nonlinear quantum mechanics

In Chapter 5, we described an experiment testing the linearity of time evolution in quantum mechanics [14]. Theories predicting a violation of this linearity have been previously proposed [8, 97, 98, 24] and carefully tested [91, 33, 10, 18, 96, 65]. However, naive generalizations of these theories have all generally led to violations of causality, limiting their viability. Recently, a new theoretical framework for causal nonlinear quantum mechanics has been developed [52], but, interestingly, it turns out to be poorly tested by standard atomic and nuclear spectroscopy and weakly bounded by previous experiments. The reason for this is that the new theory incorporates nonlinearities as a physical self-interaction of a system's wavefunction. For particles sensitive to electromagnetic fields, this is manifest as an interaction of the system's wavefunction with a field sourced by its expectation value. Thus, for, say, a superposition of the electronic states of an atom to be sensitive to this effect, its center of mass motion would need to be constrained to a volume comparable to the spread in its internal degrees of freedom.

To overcome this limitation, we made use of the net charge and tight confinement of a ^{40}Ca$^+$ ion contained in a Paul trap. In this context, the causal nonlinearity can be interpreted as a Coulomb field sourced by the position-space probability distribution of the ion, which acts to repel it. If the ion is prepared in a superposition of two distinct positions in space, then this field will interact differently with both branches of the superposition causing a relative energy shift that can be measured using a Ramsey experiment. We performed such an experiment, using a superposition of the ground and first excited state of the ion's

vibrational motion, as defined by the harmonic pseudopotential that binds it in place. A characteristic feature of the nonlinear interaction is that the Ramsey phase accumulated by the ion during the experiment will depend sensitively on the relative population present in the two branches of the superposition. We leveraged this feature by performing pairs of Ramsey experiments using superpositions with two distinct relative population weights, thus allowing us to rule out most systematics. Using this technique, we were able to set a fractional bound on the order of 10^{-12} for any potential electromagnetic nonlinear perturbations of the Schrödinger equation. This represents about a seven-order-of-magnitude improvement of the previously best-estimated bounds on this theory [52].

In addition to setting a more stringent bound on the theory, this experiment serves as an easy-to-understand example of how causal nonlinear quantum mechanics affects quantum systems and the limitations and strategies that might be employed to probe for these effects. The sensitivity of our experiment can be improved by using a heavier ion with a higher trap frequency (so that it is more tightly localized in space), by reducing the ion's heating rate or by increasing the number of repetitions of the experiment. In all cases, the sensitivity of the experiment scales modestly $x^{1/2}$ with these parameters so, for realistic values, one might only hope to achieve an improvement of several orders of magnitude. On the other hand, it might be possible to use more sophisticated measurement protocols along with superpositions of more complicated states, like strings of ions or squeezed states to achieve more substantial gains.

Test of local Lorentz invariance

Lorentz symmetry is a fundamental assumption of relativity, dictating that the laws of physics remain unchanged when moving from one inertial reference frame to another. Nonetheless, some modern theories predict that this symmetry might be broken at high enough energy. Currently, the extraordinary spectroscopic sensitivity that can be achieved using atomic systems is sufficient to probe for such effects at theoretically relevant scales, despite the low energy scales of these systems. Previously, the most stringent bounds on the hypothetical Lorentz symmetry violations of the electron were set by an experiment using trapped ^{40}Ca$^+$ ions [80]. This result was achieved despite the presence of large magnetic field fluctuations in the system by taking advantage of the correlated effect of this noise on two co-trapped ions.

In Chapter 6, we present the results of an experiment [68] that builds on this previous work by performing a similar test of Lorentz symmetry using two entangled ^{40}Ca$^+$ ions, prepared in a decoherence free state. We empirically verify the expected gain of a factor of two in spectroscopic sensitivity obtained by using a pair of entangled, rather than correlated but unentangled, ions, predicted by theory. This enhancement is directly attributable to the entanglement of the ions, thus providing an experimental example of how entanglement might be leveraged as a resource to improve precision measurements. By additionally collecting more measurement statistics, we improved the best bounds on Lorentz symmetry violations of the electron by a factor of two to four, to a value of about 5×10^{-19}.

In principle, it is possible to extend this technique to larger systems of ions. For example, in comparison with Equation 6.18, a decoherence free state of the form $(|D_{1/2}D_{-1/2}D_{-1/2}D_{1/2}\rangle + |D_{5/2}D_{-5/2}D_{-5/2}D_{5/2}\rangle)$ might be prepared, which is insensitive to both the magnetic field and its gradient, while remaining sensitive to signatures of Lorentz violations. On the other hand, scaling up spectroscopy with classically correlated ions is nontrivial. For example, the decoherence free subspace will generally contain multiple states with different sensitivities to LLI violations. Thus, it is likely the benefit of using entangled states of ^{40}Ca$^+$ ions might increase with system size, at least theoretically. However, there are practical challenges to scaling up the preparation of high-fidelity entangled states to larger system sizes. And, on the other hand, $F_{7/2}$ state of Yb$^+$ is an order of magnitude more sensitive to hypothetical Lorentz violations than the $D_{5/2}$ states of ^{40}Ca$^+$ [29, 90], making this a much more attractive testbed. More recent experiments using magnetic field insensitive clocks states [87] and sophisticated dynamical decoupling techniques [26] have since improved the bounds on Lorentz violations by several orders of magnitude by using single trapped Yb ions.

Bibliography

[1]   Daniel S. Abrams and Seth Lloyd. "Nonlinear Quantum Mechanics Implies Polynomial-Time Solution for *NP*-Complete and *# P* Problems". In: *Phys. Rev. Lett.* 81.18 (Nov. 1998), pp. 3992–3995. DOI: 10.1103/PhysRevLett.81.3992.

[2]   Nitzan Akerman et al. "Universal gate-set for trapped-ion qubits using a narrow linewidth diode laser". In: *New J. Phys.* 17.11 (Nov. 2015), p. 113060. DOI: 10.1088/1367-2630/17/11/113060.

[3]   Agasthya Ayachit and Marian Kazimierz Kazimierczuk. "Transfer functions of a transformer at different values of coupling coefficient". In: *IET Circuits Devices Syst.* 10.4 (July 2016), pp. 337–348. DOI: 10.1049/iet-cds.2015.0147.

[4]   C. J. Ballance et al. "Hybrid quantum logic and a test of Bell's inequality using two different atomic isotopes". In: *Nature* 528 (Dec. 2015), pp. 384–386. DOI: 10.1038/nature16184.

[5]   J. S. Bell. "On the Einstein Podolsky Rosen paradox". In: *Physics Physique Fizika* 1.3 (Nov. 1964), pp. 195–200. DOI: 10.1103/PhysicsPhysiqueFizika.1.195.

[6]   Jan Benhelm. "Precision spectroscopy and quantum information processing with trapped calcium ions". PhD thesis. University of Innsbruck, 2008.

[7]   D. J. Berkeland et al. "Minimization of ion micromotion in a Paul trap". In: *J. Appl. Phys.* 83.10 (May 1998), pp. 5025–5033. DOI: 10.1063/1.367318.

[8]   Iwo Bialynicki-Birula and Jerzy Mycielski. "Nonlinear wave mechanics". In: *Ann. Phys.* 100.1 (Sept. 1976), pp. 62–93. DOI: 10.1016/0003-4916(76)90057-9.

[9]   R. Blmel et al. "Phase transitions of stored laser-cooled ions". In: *Nature* 334 (July 1988), pp. 309–313. DOI: 10.1038/334309a0.

[10]   J. J. Bollinger et al. "Test of the linearity of quantum mechanics by rf spectroscopy of the ^{9}Be$^+$ ground state". In: *Phys. Rev. Lett.* 63.10 (Sept. 1989), pp. 1031–1034. DOI: 10.1103/PhysRevLett.63.1031.

[11]   J. J. . Bollinger et al. "Optimal frequency measurements with maximally correlated states". In: *Phys. Rev. A* 54.6 (Dec. 1996), R4649–R4652(R). DOI: 10.1103/PhysRevA.54.R4649.

[12] Sbastien Bourdeauducq et al. "ARTIQ". In: *Zenodo* (Feb. 2021). DOI: 10.5281/zenodo.6619071.

[13] Heinz-Peter Breuer and Francesco Petruccione. *The Theory of Open Quantum Systems*. Oxford, England, UK: Oxford University Press, Mar. 2007.

[14] Joseph Broz et al. "Test of Causal Nonlinear Quantum Mechanics by Ramsey Interferometry with a Trapped Ion". In: *Phys. Rev. Lett.* 130.20 (May 2023), p. 200201. DOI: 10.1103/PhysRevLett.130.200201.

[15] K. E. Cahill and R. J. Glauber. "Ordered Expansions in Boson Amplitude Operators". In: *Phys. Rev.* 177.5 (Jan. 1969), pp. 1857–1881. DOI: 10.1103/PhysRev.177.1857.

[16] Howard Carmichael. *An Open Systems Approach to Quantum Optics*. Berlin, Germany: Springer, 1993.

[17] J. Chiaverini et al. "Surface-electrode architecture for ion-trap quantum information processing". In: *Quantum Inf. Comput.* 5.6 (Sept. 2005), pp. 419–439. DOI: 10.5555/2011670.2011671.

[18] T. E. Chupp and R. J. Hoare. "Coherence in freely precessing ^{21}Ne and a test of linearity of quantum mechanics". In: *Phys. Rev. Lett.* 64.19 (May 1990), pp. 2261–2264. DOI: 10.1103/PhysRevLett.64.2261.

[19] Michael Chwalla. "Precision spectroscopy with ^{40}Ca$^+$ ions in a Paul trap". PhD thesis. University of Innsbruck, 2009.

[20] J. I. Cirac and P. Zoller. "Quantum Computations with Cold Trapped Ions". In: *Phys. Rev. Lett.* 74.20 (May 1995), pp. 4091–4094. DOI: 10.1103/PhysRevLett.74.4091.

[21] B. Cogitore, J. P. Keradec, and J. Barbaroux. "The two-winding transformer: an experimental method to obtain a wide frequency range equivalent circuit". In: *IEEE Trans. Instrum. Meas.* 43.2 (Apr. 1994), pp. 364–371. DOI: 10.1109/19.293449.

[22] Eugene D. Commins. *Quantum Mechanics: An Experimentalist's Approach*. Cambridge, England, UK: Cambridge University Press, Sept. 2014.

[23] H. G. Dehmelt. "Radiofrequency Spectroscopy of Stored Ions I: Storage". In: *Advances in Atomic and Molecular Physics*. Vol. 3. Cambridge, MA, USA: Academic Press, Jan. 1968, pp. 53–72. DOI: 10.1016/S0065-2199(08)60170-0.

[24] H.-D. Doebner and Gerald A. Goldin. "On a general nonlinear Schrdinger equation admitting diffusion currents". In: *Phys. Lett. A* 162.5 (Feb. 1992), pp. 397–401. DOI: 10.1016/0375-9601(92)90061-P.

[25] Jonathan P. Dowling and Gerard J. Milburn. "Quantum technology: the second quantum revolution". In: *Philos. Trans. R. Soc. London, Ser. A* 361.1809 (Aug. 2003), pp. 1655–1674. DOI: 10.1098/rsta.2003.1227.

[26] Laura S. Dreissen et al. "Improved bounds on Lorentz violation from composite pulse Ramsey spectroscopy in a trapped ion". In: *Nat. Commun.* 13.7314 (Nov. 2022), pp. 1–6. DOI: 10.1038/s41467-022-34818-0.

[27] R. W. P. Drever et al. "Laser phase and frequency stabilization using an optical resonator". In: *Appl. Phys. B* 31.2 (June 1983), pp. 97–105. DOI: 10.1007/BF00702605.

[28] Daniel H. E. Dubin. "Theory of structural phase transitions in a trapped Coulomb crystal". In: *Phys. Rev. Lett.* 71.17 (Oct. 1993), pp. 2753–2756. DOI: 10.1103/PhysRevLett.71.2753.

[29] V. A. Dzuba et al. "Strongly enhanced effects of Lorentz symmetry violation in entangled Yb+ ions". In: *Nat. Phys.* 12 (May 2016), pp. 465–468. DOI: 10.1038/nphys3610.

[30] Jrgen Eschner et al. "Laser cooling of trapped ions". In: *J. Opt. Soc. Am. B, JOSAB* 20.5 (May 2003), pp. 1003–1015. DOI: 10.1364/JOSAB.20.001003.

[31] Christopher J. Foot. *Atomic Physics (Oxford Master Series in Physics).* Oxford, England, UK: Oxford University Press, Feb. 2005.

[32] Marco Frasca. "A modern review of the two-level approximation". In: *Ann. Phys.* 306.2 (Aug. 2003), pp. 193–208. DOI: 10.1016/S0003-4916(03)00078-2.

[33] R. Ghler, A. G. Klein, and A. Zeilinger. "Neutron optical tests of nonlinear wave mechanics". In: *Phys. Rev. A* 23.4 (Apr. 1981), pp. 1611–1617. DOI: 10.1103/PhysRevA.23.1611.

[34] A. V. Gaponov and M. A. Miller. "On the potential well for charged particles in a high frequency electromagnetic field". In: *Zhur. Eksptl'. i Teoret. Fiz* Vol: 34 (Jan. 1958).

[35] Anupam Garg. *Classical Electromagnetism in a Nutshell (In a Nutshell, 13).* Princeton, NJ, USA: Princeton University Press, Apr. 2012.

[36] Christopher Gerry and Peter Knight. *Introductory Quantum Optics.* Cambridge, England, UK: Cambridge University Press, Nov. 2004.

[37] N. Gisin. "Stochastic quantum dynamics and relativity". In: *Helv. Phys. Acta* 62.4 (1989), pp. 363–371.

[38] N. Gisin. "Weinberg's non-linear quantum mechanics and supraluminal communications". In: *Phys. Lett. A* 143.1 (Jan. 1990), pp. 1–2. DOI: 10.1016/0375-9601(90)90786-N.

[39] Dylan Gorman. "Noise sensing and quantum simulation with trapped atomic ions". PhD thesis. University of California Berkeley, 2017.

[40] David J. Griffiths. *Introduction to Electrodynamics.* Cambridge University Press, 2018.

[41] David J. Griffiths and Darrell F. Schroeter. *Introduction to Quantum Mechanics.* Cambridge, England, UK: Cambridge University Press, Aug. 2018.

[42] H. Haffner et al. "Precision Measurement and Compensation of Optical Stark Shifts for an Ion-Trap Quantum Processor". In: *Phys. Rev. Lett.* 90.14 (Apr. 2003), p. 143602. DOI: 10.1103/PhysRevLett.90.143602.

[43] M. Harlander et al. "Trapped-ion probing of light-induced charging effects on dielectrics". In: *New J. Phys.* 12.9 (Sept. 2010), p. 093035. DOI: 10.1088/1367-2630/12/9/093035.

[44] S. Haze et al. "Measurement of the coherence time of the ground-state Zeeman states in 40Ca+". In: *Appl. Phys. B* 105.4 (Dec. 2011), pp. 761–765. DOI: 10.1007/s00340-011-4603-3.

[45] B. L. Higgins et al. "Entanglement-free Heisenberg-limited phase estimation". In: *Nature* 450 (Nov. 2007), pp. 393–396. DOI: 10.1038/nature06257.

[46] M. A. Hohensee et al. "Limits on Violations of Lorentz Symmetry and the Einstein Equivalence Principle using Radio-Frequency Spectroscopy of Atomic Dysprosium". In: *Phys. Rev. Lett.* 111.5 (July 2013), p. 050401. DOI: 10.1103/PhysRevLett.111.050401.

[47] Jonathon P. Home. "Quantum Science and Metrology with Mixed-Species Ion Chains". In: *Advances In Atomic, Molecular, and Optical Physics.* Vol. 62. Cambridge, MA, USA: Academic Press, Jan. 2013, pp. 231–277. DOI: 10.1016/B978-0-12-408090-4.00004-9.

[48] S. F. Huelga et al. "Improvement of Frequency Standards with Quantum Entanglement". In: *Phys. Rev. Lett.* 79.20 (Nov. 1997), pp. 3865–3868. DOI: 10.1103/PhysRevLett.79.3865.

[49] W. M. Itano et al. "Quantum projection noise: Population fluctuations in two-level systems". In: *Phys. Rev. A* 47.5 (May 1993), pp. 3554–3570. DOI: 10.1103/PhysRevA.47.3554.

[50] Wayne M. Itano. "External-Field Shifts of the 199Hg+ Optical Frequency Standard". In: *J. Res. Nat. Inst. Stand. Technol.* 105.6 (Nov. 2000), p. 829. DOI: 10.6028/jres.105.065.

[51] D. F. V. James. "Quantum dynamics of cold trapped ions with application to quantum computation". In: *Appl. Phys. B* 66.2 (Feb. 1998), pp. 181–190. DOI: 10.1007/s003400050373.

[52] David E. Kaplan and Surjeet Rajendran. "Causal framework for nonlinear quantum mechanics". In: *Phys. Rev. D* 105.5 (Mar. 2022), p. 055002. DOI: 10.1103/PhysRevD.105.055002.

[53] Anders Kastberg. "The Central-Field Approximation". In: *Structure of Multielectron Atoms.* Cham, Switzerland: Springer, Apr. 2020, pp. 67–88. DOI: 10.1007/978-3-030-36420-5_5.

[54] T. W. B. Kibble. "Relativistic models of nonlinear quantum mechanics". In: *Commun. Math. Phys.* 64.1 (Dec. 1978), pp. 73–82. DOI: 10.1007/BF01940762.

[55] D. Kienzler et al. "Quantum harmonic oscillator state synthesis by reservoir engineering". In: *Science* 347.6217 (Jan. 2015), pp. 53–56. DOI: 10.1126/science.1261033.

[56] V. Alan Kosteleck and Robertus Potting. "CPT, strings, and meson factories". In: *Phys. Rev. D* 51.7 (Apr. 1995), pp. 3923–3935. DOI: 10.1103/PhysRevD.51.3923.

[57] V. Alan Kosteleck and Neil Russell. "Data tables for Lorentz and *CPT* violation". In: *Rev. Mod. Phys.* 83.1 (Mar. 2011), pp. 11–31. DOI: 10.1103/RevModPhys.83.11.

[58] D. Leibfried et al. "Quantum dynamics of single trapped ions". In: *Rev. Mod. Phys.* 75.1 (Mar. 2003), pp. 281–324. DOI: 10.1103/RevModPhys.75.281.

[59] D. Leibfried et al. "Toward Heisenberg-Limited Spectroscopy with Multiparticle Entangled States". In: *Science* 304.5676 (June 2004), pp. 1476–1478. DOI: 10.1126/science.1097576.

[60] H. X. Li et al. "Determination of the geometric parameters κz and κr of a linear Paul trap". In: *Chin. J. Phys.* 60 (Aug. 2019), pp. 61–67. DOI: 10.1016/j.cjph.2019.03.017.

[61] D. A. Lidar, I. L. Chuang, and K. B. Whaley. "Decoherence-Free Subspaces for Quantum Computation". In: *Phys. Rev. Lett.* 81.12 (Sept. 1998), pp. 2594–2597. DOI: 10.1103/PhysRevLett.81.2594.

[62] Daniel A. Lidar and K. Birgitta Whaley. "Decoherence-Free Subspaces and Subsystems". In: *Irreversible Quantum Dynamics.* Berlin, Germany: Springer, June 2003, pp. 83–120. DOI: 10.1007/3-540-44874-8_5.

[63] G. Lindblad. "On the generators of quantum dynamical semigroups". In: *Commun. Math. Phys.* 48.2 (Jan. 1976), pp. 119–130.

[64] D. M. Lucas et al. "Isotope-selective photoionization for calcium ion trapping". In: *Phys. Rev. A* 69.1 (Jan. 2004), p. 012711. DOI: 10.1103/PhysRevA.69.012711.

[65] P. K. Majumder et al. "Test of the linearity of quantum mechanics in optically pumped ^{201}Hg". In: *Phys. Rev. Lett.* 65.24 (Dec. 1990), pp. 2931–2934. DOI: 10.1103/PhysRevLett.65.2931.

[66] Brian R. Martin and Graham Shaw. *Nuclear and Particle Physics: An Introduction, 3rd Edition.* Hoboken, NJ, USA: Wiley, Apr. 2019.

[67] I. Marzoli et al. "Laser cooling of trapped three-level ions: Designing two-level systems for sideband cooling". In: *Phys. Rev. A* 49.4 (Apr. 1994), pp. 2771–2779. DOI: 10.1103/PhysRevA.49.2771.

[68] Eli Megidish et al. "Improved Test of Local Lorentz Invariance from a Deterministic Preparation of Entangled States". In: *Phys. Rev. Lett.* 122.12 (Mar. 2019), p. 123605. DOI: 10.1103/PhysRevLett.122.123605.

[69] V. Meyer et al. "Experimental Demonstration of Entanglement-Enhanced Rotation Angle Estimation Using Trapped Ions". In: *Phys. Rev. Lett.* 86.26 (June 2001), pp. 5870–5873. DOI: 10.1103/PhysRevLett.86.5870.

[70] D. L. Moehring et al. "Entanglement of single-atom quantum bits at a distance". In: *Nature* 449 (Sept. 2007), pp. 68–71. DOI: 10.1038/nature06118.

[71] *Molecular Beams*. Oxford, England, UK: Oxford University Press, Apr. 1990.

[72] Klaus Mølmer and Anders Sørensen. "Multiparticle Entanglement of Hot Trapped Ions". In: *Phys. Rev. Lett.* 82.9 (Mar. 1999), pp. 1835–1838. DOI: 10.1103/PhysRevLett.82.1835.

[73] Martin W. van Mourik et al. "rf-induced heating dynamics of noncrystallized trapped ions". In: *Phys. Rev. A* 105.3 (Mar. 2022), p. 033101. DOI: 10.1103/PhysRevA.105.033101.

[74] Tomohisa Nagata et al. "Beating the Standard Quantum Limit with Four-Entangled Photons". In: *Science* 316.5825 (May 2007), pp. 726–729. DOI: 10.1126/science.1138007.

[75] Michael A. Nielsen and Isaac L. Chuang. *Quantum Computation and Quantum Information: 10th Anniversary Edition*. Cambridge, England, UK: Cambridge University Press, Jan. 2011.

[76] *On Unitary Representations of the Inhomogeneous Lorentz Group on JSTOR*. [Online; accessed 27. Jul. 2023]. Jan. 1939.

[77] Wolfgang Paul. "Electromagnetic traps for charged and neutral particles". In: *Rev. Mod. Phys.* 62.3 (July 1990), pp. 531–540. DOI: 10.1103/RevModPhys.62.531.

[78] Joseph Polchinski. "Weinberg's nonlinear quantum mechanics and the Einstein-Podolsky-Rosen paradox". In: *Phys. Rev. Lett.* 66.4 (Jan. 1991), pp. 397–400. DOI: 10.1103/PhysRevLett.66.397.

[79] Maxim Pospelov and Yanwen Shang. "Lorentz violation in Horava-Lifshitz-type theories". In: *Phys. Rev. D* 85.10 (May 2012), p. 105001. DOI: 10.1103/PhysRevD.85.105001.

[80] T. Pruttivarasin et al. "Michelson–Morley analogue for electrons using trapped ions to test Lorentz symmetry". In: *Nature* 517 (Jan. 2015), pp. 592–595. DOI: 10.1038/nature14091.

[81] Thaned Pruttivarasin. "Spectroscopy, fundamental symmetry tests and quantum simulation with trapped ions". PhD thesis. University of California Berkeley, 2014.

[82] Michael Ramm. "Quantum Correlations and Energy Transport in Trapped Ions". PhD thesis. University of California Berkeley, 2014.

[83] C. F. Roos et al. "'Designer atoms' for quantum metrology". In: *Nature* 443 (Sept. 2006), pp. 316–319. DOI: 10.1038/nature05101.

[84] C. F. Roos et al. "Nonlinear coupling of continuous variables at the single quantum level". In: *Phys. Rev. A* 77.4 (Apr. 2008), p. 040302. DOI: 10.1103/PhysRevA.77.040302.

[85] C. F. Roos et al. "Precision Spectroscopy with Entangled States: Measurement of Electric Quadrupole Moments". In: *AIP Conf. Proc.* 869.1 (Nov. 2006), pp. 111–118. DOI: 10.1063/1.2400640.

[86] C. A. Sackett et al. "Experimental entanglement of four particles". In: *Nature* 404 (Mar. 2000), pp. 256–259. DOI: 10.1038/35005011.

[87] Christian Sanner et al. "Optical clock comparison for Lorentz symmetry testing". In: *Nature* 567 (Mar. 2019), pp. 204–208. DOI: 10.1038/s41586-019-0972-2.

[88] F. Schmidt-Kaler et al. "The coherence of qubits based on single Ca+". In: *J. Phys. B: At. Mol. Opt. Phys.* 36.3 (Jan. 2003), p. 623. DOI: 10.1088/0953-4075/36/3/319.

[89] S. Schneider and G. J. Milburn. "Decoherence and fidelity in ion traps with fluctuating trap parameters". In: *Phys. Rev. A* 59.5 (May 1999), pp. 3766–3774. DOI: 10.1103/PhysRevA.59.3766.

[90] R. Shaniv et al. "New Methods for Testing Lorentz Invariance with Atomic Systems". In: *Phys. Rev. Lett.* 120.10 (Mar. 2018), p. 103202. DOI: 10.1103/PhysRevLett.120.103202.

[91] C. G. Shull et al. "Search for a Nonlinear Variant of the Schr\"odinger Equation by Neutron Interferometry". In: *Phys. Rev. Lett.* 44.12 (Mar. 1980), pp. 765–768. DOI: 10.1103/PhysRevLett.44.765.

[92] Igor I. Sobelman. *Atomic Spectra and Radiative Transitions*. Berlin, Germany: Springer, 1992.

[93] Anders Sørensen and Klaus Mølmer. "Entanglement and quantum computation with ions in thermal motion". In: *Phys. Rev. A* 62.2 (July 2000), p. 022311. DOI: 10.1103/PhysRevA.62.022311.

[94] T. R. Tan et al. "Multi-element logic gates for trapped-ion qubits". In: *Nature* 528 (Dec. 2015), pp. 380–383. DOI: 10.1038/nature16186.

[95] J. Trautmann et al. "$^1S_0-^3P_2$ magnetic quadrupole transition in neutral strontium". In: *Phys. Rev. Res.* 5.1 (Mar. 2023), p. 013219. DOI: 10.1103/PhysRevResearch.5.013219.

[96] Ronald L. Walsworth et al. "Test of the linearity of quantum mechanics in an atomic system with a hydrogen maser". In: *Phys. Rev. Lett.* 64.22 (May 1990), pp. 2599–2602. DOI: 10.1103/PhysRevLett.64.2599.

[97] Steven Weinberg. "Precision Tests of Quantum Mechanics". In: *Phys. Rev. Lett.* 62.5 (Jan. 1989), pp. 485–488. DOI: 10.1103/PhysRevLett.62.485.

[98] Steven Weinberg. "Testing quantum mechanics". In: *Ann. Phys.* 194.2 (Sept. 1989), pp. 336–386. DOI: 10.1016/0003-4916(89)90276-5.

[99] V. Weisskopf and E. Wigner. "Berechnung der natrlichen Linienbreite auf Grund der Diracschen Lichttheorie". In: *Z. Phys.* 63.1 (Jan. 1930), pp. 54–73. DOI: 10.1007/BF01336768.

[100] N. Yu et al. "Stark shift of a single barium ion and potential application to zero-point confinement in a rf trap". In: *Phys. Rev. A* 50.3 (Sept. 1994), pp. 2738–2741. DOI: 10.1103/PhysRevA.50.2738.

Appendix A

Normal mode structure

In this appendix, we provide a general derivation of the normal mode structure for an N-ion change where each ion is allowed to have a different mass and/or degree of ionization.
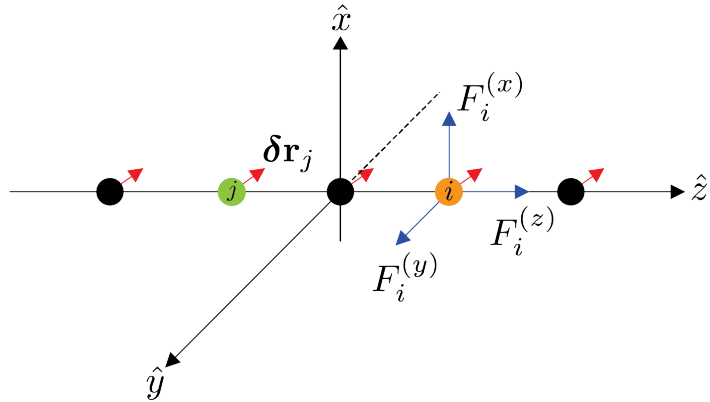
Figure A.1: A linear ion chain. When the ions are perturbed by a small amount $\boldsymbol{\delta}\mathbf{r}_j$ away from their equilibrium positions, the ith ion will experience a force $\mathbf{F}_i(\{\mathbf{r}_j\}_j)$

Linear equilibrium positions

As illustrated in Figure A.1, we consider N ions confined in the three-dimensional harmonic potential:

$$\Phi = \frac{1}{2} \sum_{i=1}^{N} m_i [(\omega_i^{(x)})^2 + (\omega_i^{(y)})^2 + (\omega_i^{(z)})^2] \tag{A.1}$$

and interacting via mutual Coulomb repulsion such that the force $\mathbf{F}_i$ on ion i at location $\mathbf{r}_i = (x_i,\ y_i,\ z_i)$ is given by:

$$
\mathbf{F}_i(\{\mathbf{r}_j\}_{j=1}^N) =
$$
$$
-m_i(\omega_i^{(x)})^2 x_i \hat{\mathbf{x}} - m_i(\omega_i^{(y)})^2 y_i \hat{\mathbf{y}} - m_i(\omega_i^{(z)})^2 z_i \hat{\mathbf{z}}
$$
$$
+ \sum_{\substack{i,\, j,\\ i \neq j}} \frac{q_i q_j [(x_i - x_j)\hat{\mathbf{x}} + (y_i - y_j)\hat{\mathbf{y}} + (z_i - z_j)\hat{\mathbf{z}}]}{k[(x_i - x_j)^2 + (y_i - y_j)^2 + (z_i - z_j)^2]} \tag{A.2}
$$

where $k = 4\pi\varepsilon_0$ and q_i is the charge of the ith ion[1]. The first term on the RHS is the force due to the trapping potential. The second term is the inter-ion Coulomb repulsion.

If the kinetic energy of the ions is small, then, since $\omega^{(z)}$ is necessarily less than $\omega^{(x,y)}$, the ions will crystallize into a linear chain oriented along the $\hat{\mathbf{z}}$-direction. The equilibrium positions $\mathbf{r}_i^0$ of the ions in this configuration are found by setting the force on each ion equal to zero:

$$
\mathbf{F}_i(\{\mathbf{r}_j^0\}_{j=1}^N) = 0 =
$$
$$
-m_i(\omega_i^{(x)})^2 x_i^0 \hat{\mathbf{x}} - m_i(\omega_i^{(y)})^2 y_i^0 \hat{\mathbf{y}} - m_i(\omega_i^{(z)})^2 z_i^0 \hat{\mathbf{z}}
$$
$$
+ \sum_{\substack{i,\, j,\\ i \neq j}}^N \frac{Q_i Q_j [(x_i^0 - x_j^0)\hat{\mathbf{x}} + (y_i^0 - y_j^0)\hat{\mathbf{y}} + (z_i^0 - z_j^0)\hat{\mathbf{z}}]}{4\pi\varepsilon_0 [(x_i^0 - x_j^0)^2 + (y_i^0 - y_j^0)^2 + (z_i^0 - z_j^0)^2]} \tag{A.3}
$$

But, for a linear chain, symmetry dictates that $x_i^0 = y_i^0 = 0$, so this expression reduces to:

$$
F_i^{(z)}(\{\mathbf{r}_j = \mathbf{r}_j^0\}_{j=1}^N) = -m_i(\omega_i^{(z)})^2 z_i^0 + \sum_{j=1}^{i-1} \frac{q_i q_j}{k(z_i^0 - z_j^0)^2} - \sum_{j=i+1}^{N} \frac{q_i q_j}{k(z_i^0 - z_j^0)^2} = 0 \tag{A.4}
$$

which can be solved to find the linear equilibrium positions. It is worth pointing out that Equation A.4 does not depend on the ionic masses. This is because, in the axial direction, the ions only interact with each other through their charge. Therefore, if two linear ion crystals have identical charge configurations, their equilibrium positions will also be the same.

Normal modes

Now, if the system experiences a small perturbation away from its equilibrium configuration: $\mathbf{r}_i^0 \rightarrow \mathbf{r}_i^0 + \boldsymbol{\delta}\mathbf{r}_i$, the first-order, linear response is:

---

[1]We don't specify the degree of ionization or the sign of the charges, but we do require that all ions have the same charge sign.

$$\mathbf{F}_i = \sum_{j=1}^{N} \left[\frac{\partial \mathbf{F}_i}{\partial \mathbf{r}_j}\right]_{\mathbf{r}_i^0} \boldsymbol{\delta r}_j \tag{A.5}$$

where the bold script denotes an additional three-dimensional index over Cartesian coordinate space so that:

$$\frac{\partial \mathbf{F}_i}{\partial \mathbf{r}_j}\boldsymbol{\delta r}_j = \begin{bmatrix} \frac{\partial F_i^{(x)}}{\partial x_j} & \frac{\partial F_i^{(x)}}{\partial y_j} & \frac{\partial F_i^{(x)}}{\partial z_j} \\ \frac{\partial F_i^{(y)}}{\partial x_j} & \frac{\partial F_i^{(y)}}{\partial y_j} & \frac{\partial F_i^{(y)}}{\partial z_j} \\ \frac{\partial F_i^{(z)}}{\partial x_j} & \frac{\partial F_i^{(z)}}{\partial y_j} & \frac{\partial F_i^{(z)}}{\partial z_j} \end{bmatrix} \begin{bmatrix} \delta x_i \\ \delta y_i \\ \delta z_i \end{bmatrix} \tag{A.6}$$

Thus, the force on the ith ion along the α-direction ($\alpha \in \{x, y, z\}$) due to the displacement of the jth ion is:

$$\delta F_{ij}^{(\alpha)} = \frac{\partial F_i^{(\alpha)}}{\partial \mathbf{r}_j}\bigg|_{\mathbf{r}_i^0} \cdot \boldsymbol{\delta r}_j = \frac{\partial F_i^{(\alpha)}}{\partial x_j}\bigg|_{\mathbf{r}_i^0} \delta x_j + \frac{\partial F_i^{(\alpha)}}{\partial y_j}\bigg|_{\mathbf{r}_i^0} \delta y_j + \frac{\partial F_i^{(\alpha)}}{\partial z_j}\bigg|_{\mathbf{r}_i^0} \delta z_j \tag{A.7}$$

But it is easily checked that, for the force in Equation A.2:

$$\frac{\partial F_i^{(\alpha)}}{\partial \beta_j}\bigg|_{\mathbf{r}_i^0} = 0 \quad \text{unless} \quad \alpha = \beta \tag{A.8}$$

That is to say, the motion decouples along the different spatial axes. So we can write Newton's equation to first-order:

$$m_i \ddot{\delta \alpha}_i = \sum_{j=1}^{N} \left[\frac{\partial F_i^{(\alpha)}}{\partial \alpha_j}\right]_{\mathbf{r}_i^0} \delta \alpha_j$$

$$= -\sum_{j=1}^{N} \mathcal{K}_{ij}^{(\alpha)} \delta \alpha_j \tag{A.9}$$

Where the explicit form of $\mathcal{K}_{ij}^{(\alpha)}$ can be computed directly from Equation A.2:

$$\mathcal{K}_{ij}^{(\alpha)} = \begin{cases} m_i (\omega_i^{(\alpha)})^2 - c_\alpha \sum_{\substack{j=1, \\ j \neq i}}^{N} \frac{q_i q_j}{k|z_i^0 - z_j^0|^3}, & i = j \\ c_\alpha \frac{q_i q_j}{k|z_i^0 - z_j^0|^3}, & i \neq j \end{cases} \tag{A.10}$$

with $c_{x,y} = 1$, $c_z = -2$.

Equation A.9 describes a coupled, linear spring-mass system. Following the standard procedure for solving such problems, we make the ansatz:

$$\delta\alpha_i = \beta_i^{(\alpha)}\exp(i\nu t) \tag{A.11}$$

In other words, we assume that all ions move along a particular spatial axis α at the same frequency but with different, though dependent, relative amplitudes $\beta_i^{(\alpha)}$. The quantity $\beta_i^{(\alpha)}$ is sometimes referred to as the *mode participation* since it describes how much the ith is involved in the motion of the mode $\boldsymbol{\beta}^{(\alpha)}$. If we introduce the mass-weighting:

$$\tilde{\beta}_i^{(\alpha)} = \sqrt{m_i}\beta_i^{(\alpha)} \tag{A.12}$$

$$\tilde{\mathcal{K}}_{ij}^{(\alpha)} = \frac{\mathcal{K}_{ij}^{(\alpha)}}{\sqrt{m_i m_j}} \tag{A.13}$$

Then the N independent solutions[2] for $(\nu,\ \boldsymbol{\beta}^{(\alpha)})$ can be found by solving the eigenvalue equation:

$$[\tilde{\boldsymbol{\mathcal{K}}}^{(\alpha)} - \nu^2 \mathbb{1}]\tilde{\boldsymbol{\beta}}^{(\alpha)} = 0 \tag{A.14}$$

For each coordinate axis α, there will be N independent solutions $\{(\nu_l,\ \boldsymbol{\beta}_l^{(\alpha)})\}_{l=1}^{N}$ known as the *normal modes* of the system. These are illustrated for both a homogeneous and heterogeneous ion chain in Figure A.2. Code for computing these modes can be found in IonSim.jl at `https://github.com/HaeffnerLab/IonSim.jl`.

---

[2]One for each kinetic degree of freedom along a particular spatial axis so that there are $3N$ in total.
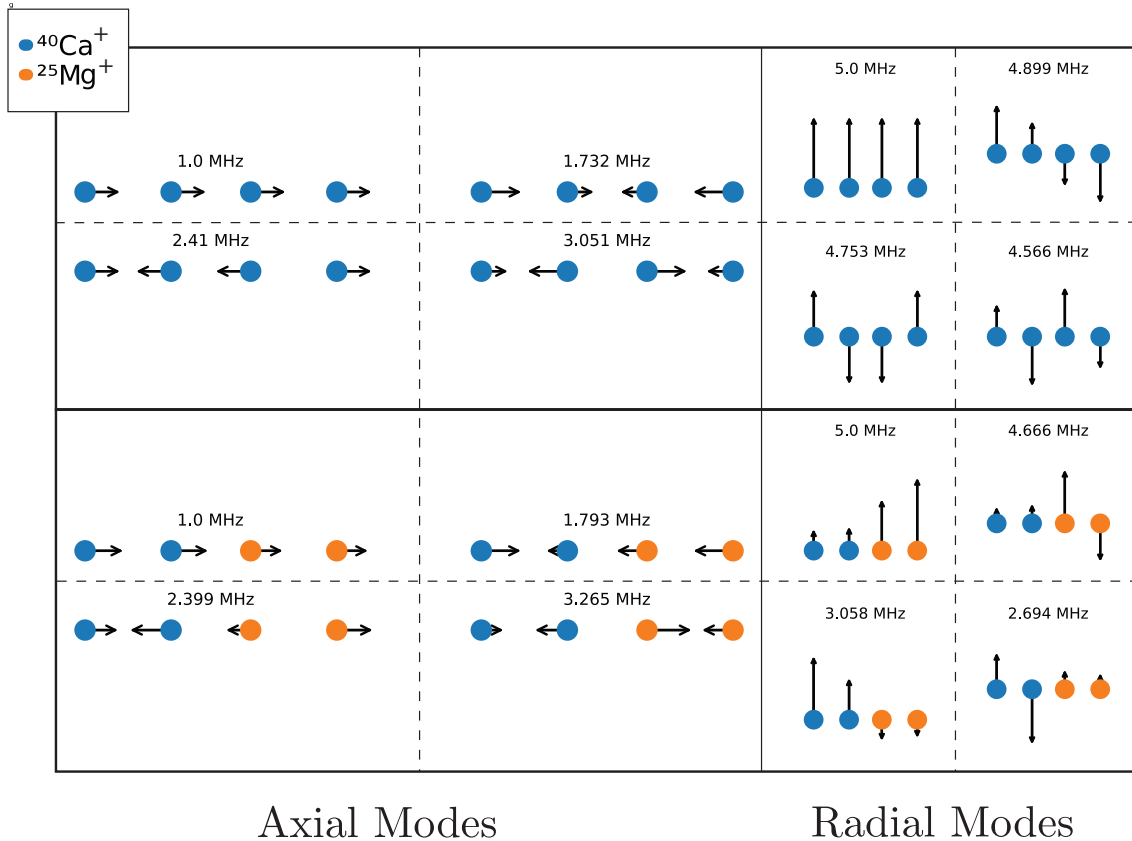
Figure A.2: Normal mode structure for a 4-ion linear Coulomb crystal. An illustration of the normal mode structure for a 4-ion linear Coulomb crystal found by solving Equation A.14 with characteristic trap frequencies of 5 MHz and 1 MHz for the radial and axial direction, respectively. This is done both for a homogeneous system (upper row) and a heterogeneous (bottom row) system. In the homogeneous case, these characteristic frequencies refer to the eigenfrequency for the unique center-of-mass modes of vibration. In the heterogeneous case, they refer to the lowest (highest) eigenfrequencies of vibration in the axial (radial) direction. The lengths of the arrows indicate the relative participation of the ion in the mode (i.e. for ion i and direction α they correspond to $\beta_i^{(a)}$ in Equation A.11).

Appendix B

Zeeman shift algorithm

All code written in Julia.

Fine structure Zeeman shift

```julia
using WignerSymbols # WignerSymbols v2.0.0
using LinearAlgebra

h = 6.626070039125929e-34  # [m² kg s⁻¹] (Planck constant)
μB = 9.27400994e-24        # [J T⁻¹] (Bohr magneton)
"""
    finestructure_zeemanshift(
        B; l, s, j, mj, fine_splitting, gl=1, gs=2, returnstate=false
    )

Given a magnetic field `B`, this calculates the Zeeman shift for the fine structure
state defined by |l, s, j, mj⟩.

`finesplitting` should be a list of the frequency splitting of the fine structure multiplets.
Only the relative frequencies matter and this list should be given in order of increasing j.

`gl`, `gs` are the orbital and spin g-factors, repsectively.

If `!returnstate` returns the eigenergy corresponding to the state that asymptotically approaches
|l, s, j, mj⟩ in the limit of zero field.

If `returnstate` returns a tuple with the eigenergy as before, but also the corresponding eigenstate
which will generally not be equal to |l, s, j, mj⟩ when the field is nonzero.
"""
function finestructure_zeemanshift(
        B; l, s, j, mj, finesplitting, gl=1, gs=2, returnstate=false
    )
    # We are going to iterate over all (j, m_j) so we give the user's input a special label
    J = j
```

```
30          mJ = mj
31          # jvalues = all possible values of j according to rules of angular momentum in QM
32          jvalues = collect(abs(l-s):l+s)
33          @assert J in jvalues  # check that user input is an allowed angular momentum value
34          # check that the fine_splitting has the appropriate length
35          @assert length(jvalues) == length(finesplitting)
36
37          # construct the fine structure hamiltonian in the coupled |l s; j m  basis
38          # (this will be diagonal)
39          coupled_basis_order = Dict()
40          basisvector = 1  # keeps track of the ordering of the basis
41          finestructure = Real[]
42          for (ji, j) in enumerate(jvalues)
43              for mj in -j:j
44                  push!(finestructure, finesplitting[ji])
45                  coupled_basis_order[(j=j, mj=mj)] = basisvector
46                  basisvector += 1  # keep track of the ordering of the basis
47              end
48          end
49          Hfs = diagm(0 => finestructure)
50
51          # construct Zeeman hamiltonian in the uncoupled |l m ; s m  basis
52          # (this will be diagonal)
53          uncoupled_basis_order = Dict()
54          basisvector = 1  # keep track of the ordering of the basis
55          zeeman = Real[]
56          for ml in -l:l
57              for ms in -s:s
58                  push!(zeeman, ( B / h) * B * (gl * ml + gs * ms))
59                  uncoupled_basis_order[(ml=ml, ms=ms)] = basisvector
60                  basisvector += 1  # keep track of the ordering of the basis
61              end
62          end
63          Hz = diagm(0 => zeeman)
64
65          # compute basis transformation, T, from |l s; j m  -> |l m ; s m  using
66          # Clebsch-Gordan coefficients
67          T = zeros(Real, size(Hz))
68          for j in jvalues
69              for mj in -j:j
70                  for ml in -l:l
71                      for ms in -s:s
72                          uncoup_indx = uncoupled_basis_order[(ml=ml, ms=ms)]
73                          coup_indx = coupled_basis_order[(j=j, mj=mj)]
74                          if ml + ms != mj
75                              T[uncoup_indx, coup_indx] = 0
76                          end
77                          cgcoefficient = clebschgordan(l, ml, s, ms, j, mj)
78                          if cgcoefficient != 0
79                              T[uncoup_indx, coup_indx] = cgcoefficient
```

```
80                          end
81                      end
82                  end
83              end
84          end
85          # Now we can use T, to change the basis of Hz from |l m; s m  -> |l s; j m .
86          # Then, we can add this to Hfs (already in coupled basis) and diagonalize
87          # the whole thing to find the eigenergies and eigenstates.
88          H = Hfs +  inv(T) * Hz * T
89          perturbedenergies, perturbedstates = eigen(H)
90          # index of the state that asymptotically approaches |l s; j m  in the limit of B=0
91          JmJindex = coupled_basis_order[(j=J, mj=mJ)]
92          # if !returnstate (default) just return an eigenergy
93          if !returnstate
94              return perturbedenergies[JmJindex]
95          end
96          # if returnstates return a tuple, first element eigenenergy
97          # and second element corresponding eigenstate
98          return perturbedenergies[JmJindex], perturbedstates[:, JmJindex]
99      end
100
```

Hyperfine structure Zeeman shift

```
1   """
2       hyperfinestructure_zeemanshift(
3           B; l, s, j, i, f, mf, hyperfinesplitting; gl=1, gs=2, gi=0,
4           returnstate=false,
5       )
6
7   Given a magnetic field `B`, this calculates the Zeeman shift for the hyperfine structure
8   state defined by |l, s, j, i, f, mf .
9
10  `hyperfinesplitting` should be a list of the frequency splitting of the hyperfine structure
11  multiplets. Only the relative frequencies matter and this list should be given in order of
12  increasing f.
13
14  `gl`, `gs`, `gi` are the orbital, spin and nuclear g-factors, repsectively.
15
16  If `!returnstate` returns the eigenergy corresponding to the state that asymptotically approaches
17  |l, s, j, i, f, mf in the limit of zero field.
18
19  If `returnstate` returns a tuple with the eigenergy as before, but also the corresponding eigenstate
20  which will generally not be equal to |l, s, j, i, f, mf  when the field is nonzero.
21  """
22  function hyperfinestructure_zeemanshift(
23          B; l, s, j, i, f, mf, hyperfinesplitting, gl=1, gs=2, gi=0,
```

```
24          returnstate=false,
25      )
26      # We are going to iterate over all (f, mf) so we give the user's input a special label
27      F = f
28      mF = mf
29      # jvalues = all possible values of f according to rules of angular momentum addition in QM
30      fvalues = collect(abs(j-i):j+i)
31      @assert F in fvalues  # check that user input is an allowed angular momentum value
32      # check that the hyperfinesplitting has the appropriate length
33      @assert length(fvalues) == length(hyperfinesplitting)
34
35      # construct hyperfine hamiltonian in coupled |j i; f m_f  basis (this will be diagonal)
36      coupled_basis_order = Dict()
37      basisvector = 1  # keeps track of the ordering of the basis
38      hyperfinestructure = Real[]
39      for (fi, f) in enumerate(fvalues)
40          for mf in -f:f
41              push!(hyperfinestructure, hyperfinesplitting[fi])
42              coupled_basis_order[(f=f, mf=mf)] = basisvector
43              basisvector += 1  # keep track of the ordering of the basis
44          end
45      end
46      Hhfs = diagm(0 => hyperfinestructure)
47
48      # construct Zeeman hamiltonian in uncoupled |j mj; i mi  basis (this will be diagonal)
49      uncoupled_basis_order = Dict()
50      basisvector = 1  # keep track of the ordering of the basis
51      zeeman = Real[]
52      for mj in -j:j
53          for mi in -i:i
54              g = landegj(l, j, s)  # note this function internally assumes gl=1, gs=2
55              push!(zeeman, (B / h) * B * (g * mj + gi * mi))
56              uncoupled_basis_order[(mj=mj, mi=mi)] = basisvector
57              basisvector += 1  # keep track of the ordering of the basis
58          end
59      end
60      Hz = diagm(0 => zeeman)
61
62      # compute basis transformation T from |j i; f mf  -> |j mj; i mi  using Clebsch-Gordan coeffs
63      T = zeros(Real, size(Hz))
64      for f in fvalues
65          for mf in -f:f
66              for mj in -j:j
67                  for mi in -i:i
68                      uncoup_indx = uncoupled_basis_order[(mj=mj, mi=mi)]
69                      coup_indx = coupled_basis_order[(f=f, mf=mf)]
70                      if mj + mi != mf
71                          T[uncoup_indx, coup_indx] = 0
72                      end
73                      cgcoefficient = clebschgordan(j, mj, i, mi, f, mf)
```

```julia
74                        if cgcoefficient != 0
75                            T[uncoup_indx, coup_indx] = cgcoefficient
76                        end
77                    end
78                end
79            end
80        end
81        # Now we can use T, to change the basis of Hz from |j mj; i mi -> |j i; f mf .
82        # Then, we can add this to Hhfs (already in coupled basis) and diagonalize
83        # the whole thing to find the eigenergies and eigenstates.
84        H = Hhfs +  inv(T) * Hz * T
85        perturbedenergies, perturbedstates = eigen(H)
86        # index of the state that asymptotically approaches |j i; f mf  in the limit of B=0
87        FmFindex = coupled_basis_order[(f=F, mf=mF)]
88        # if !returnstate (default) just return an eigenergy
89        if !returnstate
90            return perturbedenergies[FmFindex]
91        end
92        # if returnstates return a tuple, first element eigenenergy
93        # and second element corresponding eigenstate
94        return perturbedenergies[FmFindex], perturbedstates[:, FmFindex]
95    end
96
97    # Compute the lande g-factor for the fine structure level
98    function landegj(l::Real, j::Real, s::Real=1//2, gs::Real=2, gl::Real=1)
99        Lexp = (gl - 1) * ((j*(j+1) + l*(l+1) - s*(s+1)) / (2*j*(j+1)))
100       Sexp = (gs - 1) * ((j*(j+1) - l*(l+1) + s*(s+1)) / (2*j*(j+1)))
101       return 1 + Lexp + Sexp
102   end
```
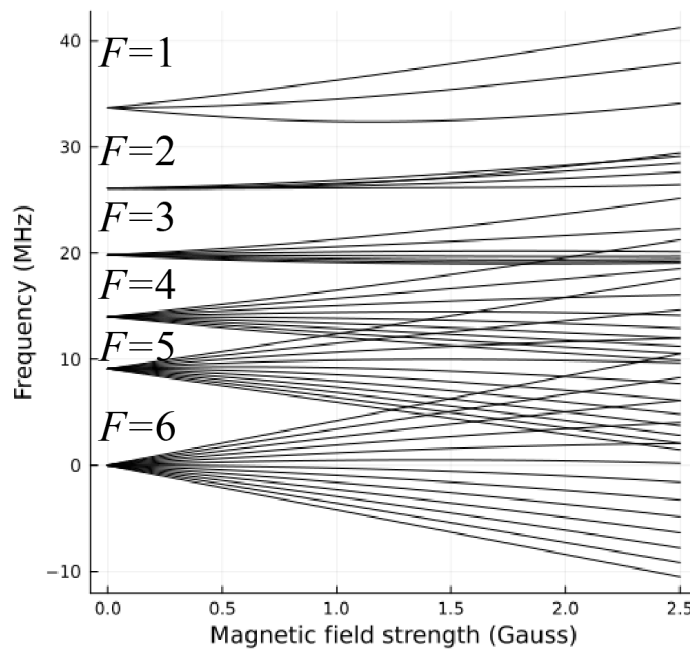
```julia
1   using Plots
2   B = range(0, 2.5, 100)
3   p = plot(
4       xlabel="Magnetic field strength (Gauss)", ylabel="Frequency (MHz)",
5       title="Zeeman shift of the 3²D(5/2) hyperfine levels of ³Ca ",
6       size=(500, 500), legend=false
7   )
8   l = 2; j = 5/2; i = 7/2
9   hyperfinesplitting = [33.7, 26.1, 19.8, 14, 9.1, 0] * 1e6
10  for f in 1:6
11      for mf in -f:f
12          hps = hyperfinestructure_zeemanshift.(
13              B * 1e-4, l=l, s=1/2, j=j, i=i, f=f, mf=mf, hyperfinesplitting=hyperfinesplitting,
14          )
15          plot!(B,  hps ./ 1e6, color="black")
16      end
17  end
```

```
18    display(p)
```

Zeeman shift of the $3^2\mathrm{D}_{5/2}$ hyperfine levels of $^{43}\mathrm{Ca}^+$

Figure B.1: Zeeman shift of the $3^2 D_{5/2}$ hyperfine levels of $^{43}\mathrm{Ca}^+$.

Appendix C

Electric multipole transition matrix elements

Following [95], we imagine an electric field with the following spatial component:

$$\mathbf{E}(\mathbf{r}) = E_0 \exp(i\mathbf{k} \cdot \mathbf{r}) + \text{c.c.} \tag{C.1}$$

interacting with the electric 2^K-pole of a single transition in a single-electron atom. The corresponding semiclassical interaction Hamiltonian:

$$\hat{H}^{EK} = \sum_{q=-K}^{K} [\mathbf{Y}_{Kq}(\hat{\mathbf{k}}) \cdot \hat{\boldsymbol{\epsilon}}] \hat{H}_q^{EK} \tag{C.2}$$

where $\hat{\mathbf{k}} = \mathbf{k}/|\mathbf{k}|$ can be parameterized in terms of the angles θ, ρ relative to the quantization axis (see Figure 2.11) and $\mathbf{Y}_{Kq}^E(\hat{\mathbf{k}})$ is defined in terms of the spherical harmonic vectors:

$$\mathbf{Y}_{Kq}(\hat{\mathbf{k}}) = \sqrt{\frac{K+1}{2K+1}} \mathbf{Y}_{K,K-1,q}(\hat{\mathbf{k}}) + \sqrt{\frac{K}{2K+1}} \mathbf{Y}_{K,K+1,q}(\hat{\mathbf{k}}) \tag{C.3}$$

$$\mathbf{Y}_{Klq}(\hat{\mathbf{k}}) = (-1)^{K-q} \sqrt{2K+1} \sum_{p=-1}^{1} \begin{pmatrix} K & 1 & l \\ -1 & p & q-p \end{pmatrix} Y_l^{q-p}(\hat{\mathbf{k}}) \hat{\mathbf{e}}_p \tag{C.4}$$

with Y_l^m the normal spherical harmonics and $\hat{\mathbf{e}}_p$, the spherical basis unit vectors:

$$\hat{\mathbf{e}}_0 = \hat{\mathbf{z}}, \qquad \hat{\mathbf{e}}_{\pm 1} = \frac{\mp(\hat{\mathbf{x}} \pm i\hat{\mathbf{y}})}{\sqrt{2}} \tag{C.5}$$

describing the orientation of the valence electron relative to the nucleus (so, e.g. $\hat{\mathbf{e}}_0$ is parallel to the quantization axis set by a static magnetic field).

The qth component $\hat{H}_q^{EK}$ of $\hat{H}^{EK}$ is given by:

$$\hat{H}_q^{EK} = 8\pi E_0 (ik)^{K-1} \sqrt{\frac{(2K+1)(K+1)}{4\pi K}} \frac{1}{(2K+1)!!} \hat{Q}_{K,q} \tag{C.6}$$

with $\hat{Q}_{K,q}$ is the Kth multipolar moment of the atom in the spherical basis:

$$\hat{Q}_{K,q} = \hat{r}^K C_q^K \tag{C.7}$$

where e is the fundamental unit of charge and Racah normalized spherical harmonics:

$$C_q^K = \sqrt{\frac{4\pi}{2K+1}} Y_k^q \tag{C.8}$$

The matrix element characterizing the strength of a transition between the states $|E\rangle = |n, l, j, m_j\rangle$ and $|E'\rangle = |n', l', j', m'_j\rangle$ is given by:

$$\langle E'|\hat{H}_q^{EK}|E\rangle = 8\pi e E_0 (ik)^{K-1} \sqrt{\frac{(2K+1)(K+1)}{4\pi K}} \frac{1}{(2K+1)!!} \langle E'|\hat{Q}_{K,q}|E\rangle$$

$$= 8\pi e E_0 (ik)^{K-1} \sqrt{\frac{(2K+1)(K+1)}{4\pi K}} \frac{1}{(2K+1)!!} (-1)^{j'-m'_j} \begin{pmatrix} j' & K & j \\ -m'_j & q & m' \end{pmatrix} \langle E'||\hat{Q}_K||E\rangle \tag{C.9}$$

where the last line follows from the Wigner-Eckart theorem and the term in big parantheses is the Wigner 3-j symbol. The term $\langle E'||\hat{Q}_K||E\rangle$ is a reduced matrix element, which can be related to the Einstein A coefficient for the transition:

$$A_K = \frac{c\alpha(2K+2)(2K+1)k^{2K+1}}{K[(2K+1)!!]^2} \frac{|\langle E'||\hat{Q}_K||E\rangle|^2}{2j'+1} \tag{C.10}$$

where c is the speed of light in vacuum, α is the fine structure constant and it is important that the primed coordinates denote the higher energy state (such that j' in the above equation corresponds to the total angular momentum quantum number for the higher energy state). Code for computing these matrix elements in terms of the multipole order, laser geometry, Einstein A coefficient and strength is provided below.

```julia
using WignerSymbols
using BigCombinatorics: DoubleFactorial
using LinearAlgebra:dot
import SphericalHarmonics.sphericalharmonic as sphericalharmonic

# Cartesian unit vectors
x = [1, 0, 0]
y = [0, 1, 0]
z = [0, 0, 1]
```

```julia
10
11     # Spherical basis unit vectors
12     ep = -(x̂ + 1im * ŷ) / √2
13     em = (x̂ - 1im * ŷ) / √2
14     e0 = ẑ
15
16     # Y_Klq( , ) as defined in Equation A6 of https://doi.org/10.1103/PhysRevResearch.5.013219
17     # Though there is a typo and the spherical harmonic in this equation should be Y_l^(q-p)
18     function Y_Klq( ,  , K, l, q)
19         Y = [0, 0, 0]
20         e = [em, e0, ep]
21         for (i, p) in enumerate([-1, 0, 1])
22             if abs(q - p) > l
23                 continue
24             else
25                 Y += wigner3j(K, 1, l, -q, p, q-p) * sphericalharmonic( ,  , l, q-p) * e[i]
26             end
27         end
28         return (-1)^(K - q) * sqrt(2K+1) * Y
29     end
30
31     # Y_Kq¹( , ) as defined in Equation A11 of https://doi.org/10.1103/PhysRevResearch.5.013219
32     function Y_KqE( ,  ; K, q)
33         √((K+1)/(2K+1)) * Y_Klq( ,  , K, K-1, q) + √(K/(2K+1)) * Y_Klq( ,  , K, K+1, q)
34     end
35
36     # Q_Kq^E from Equation A20 in https://doi.org/10.1103/PhysRevResearch.5.013219
37     # (modulo the reduced matrix element)
38     function Q_KqE(K, q; Jf, Mf, Ji, Mi)
39         (-1 + 0im)^(Jf - Mf) * wigner3j(Jf, K, Ji, -Mf, q, Mi)
40     end
41
42     function matrixelement(;
43             order,  # order of the multipole (1 for dipole, 2 for quadrupole, etc.)
44             Ji, Mi, Jf, Mf,  # i (initial) and f (final)  total angular momentum quantum numbers J̄² , J̄z
45             Li=nothing, Lf=nothing,  # intial/final orbital angular momentum L²  (only used for enforcing parity)
46             E=1, lambda=2 , khat, epsilon,  # Electric field strength of laser, wavelength, direction and polarization
47             A=1,  # Einstein A coefficient
48             only_geometry_dependent=false
49         )
50         # enforce parity rules
51         if !isnothing(Lf) && isnothing(Li)
52             isodd(abs(Lf - Li)) && iseven(order) && return 0.
53             iseven(abs(Lf - Li)) && isodd(order) && return 0.
54         end
55         k = 2 /lambda
56         e = 1.60217663e-19  # charge magnitude of electron
57         alpha = 0.0072973525693  # fine structure constant
58         c = 299_792_458  # speed of light
59         K = order  # 1 for dipole, 2 for quadrupole, etc.
```

```
60        theta = acos(khat[3])   # z-component
61        phi = atan(khat[2], khat[1])   # y-component, x-component
62        Jlarger = Jf > Ji ? Jf : Ji
63        rme_num = sqrt(K * DoubleFactorial(2K + 1)^2 * (2Jlarger + 1) * A)
64        rme_denom = sqrt(alpha * c * (2K + 2) * (2K + 1) * k^(2K + 1))
65        reduced_matrixelement = rme_num / rme_denom
66        linestrength = 0
67        for q in -K:K
68            h = (1im * k)^(K-1) * e * E * Q_KqE(K, q; Jf=Jf, Mf=Mf, Ji=Ji, Mi=Mi) * reduced_matrixelement
69            if only_geometry_dependent   # this corresponds to the g functions from Christian Roos's thesis
70                if q == Mf - Mi
71                    linestrength += dot(Y_KqE(theta, phi; K=K, q=q), epsilon)
72                    break
73                end
74            else
75                linestrength += dot(Y_KqE(theta, phi; K=K, q=q), epsilon) * h
76            end
77        end
78        bK = 8 * √((2K+1) * (K+1) / (4 *K))  * (1 / DoubleFactorial(2K+1))
79        linestrength *= bK
80        return linestrength
81    end
```

For example:

```
1    import PyPlot
2    const plt = PyPlot
3    using LaTeXStrings
4
5    Ji = 3/2
6    Jf = 3/2
7    Mi = -1/2
8    Mf = 3/2
9    order = 3
10   N = 100
11   theta = collect(range(0,  /2, N))
12   rho = collect(range(0,  /2, N))
13   Z = zeros(N, N)
14   for i in 1:N, j in 1:N
15       khat = sin(theta[i]) * x + cos(theta[i]) * z
16       epsilon = sin(rho[j]) * y + cos(rho[j]) * (sin(theta[i]) * z - cos(theta[i]) * x)
17       Z[i, j] = abs(
18               matrixelement(
19                   order=order, Jf=Jf, Mf=Mf, Ji=Ji, Mi=Mi, khat=khat, epsilon=epsilon,
20                   only_geometry_dependent=true
21               )
22           )
23   end
24   cc = plt.contourf(rad2deg.(rho), rad2deg.(theta), Z, levels=10, cmap="Greys_r")
```

```
25    clb=plt.colorbar(label="a.b.u.")
26    clb.ax.tick_params(labelsize=12)
27    plt.contour(rad2deg.(rho), rad2deg.(theta), Z, levels=10, linewidths=0.5, colors="k")
28    plt.ylabel(L"$\theta( )$", fontsize=20)
29    plt.xlabel(L"$\rho( )$", fontsize=20)
30    plt.grid("on", color="black", linewidth=0.2, linestyle="dashed")
31    plt.title(L"$|\Delta m|=$" *  "$(abs(Int(Mf - Mi)))", fontsize=20)
32    plt.show()
```
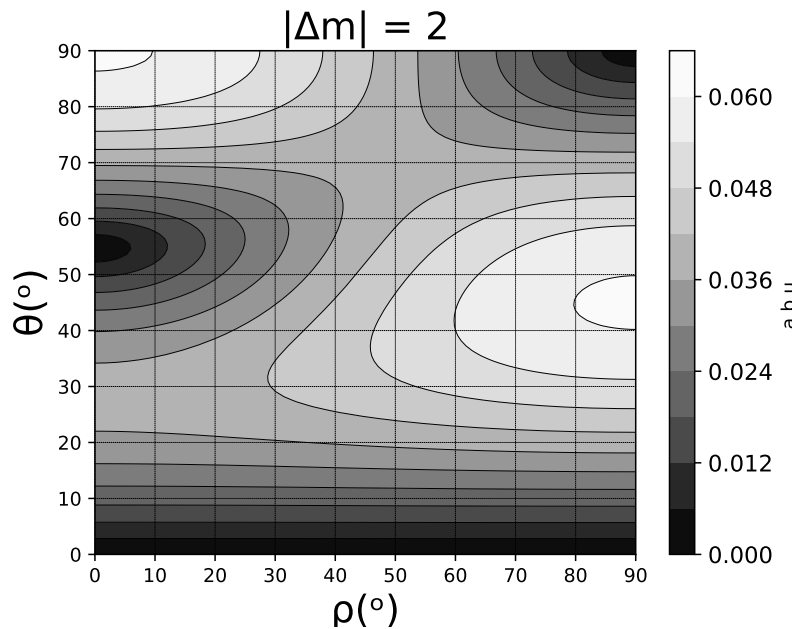

Figure C.1: Example calculation of the geometric portion of an electric multipole transition matrix element. Here we plot the geometric dependence of an electric octupole between a $j = 3/2$ and $j = 3/2$ state (e.g. $D_{3/2} \leftrightarrow P_{3/2}$, though this is dominated by the dipole component).

Appendix D

Experimental control software

An example of a user-defined pulse sequence is given in Section D. This code performs a Ramsey experiment. The class attribute PulseSequence.accessed_params determines the parameters to be readout from parametervault and loaded into the FPGA. Any parameter listed here will also be displayed in the experimental control window (see Figure D.1).

The class attribute PulseSequence.scan_params is a dictionary where the key refers to the name of the experiment to be performed and the values are a tuple with the form ([a string corresponding to the window of the plotter in which to plot the results], ([parametervault parameter to be scanned], default starting value of parameter], [default ending value of the parameter to be scanned], [number of scan points], [parameter units])). If a scannable parameter is defined here, it shows up as a scan widget in the experimental control window (see Figure D.1). The scan to be run in a specific experiment can then be chosen with the scan_selection spinbox. One can also choose to have non-uniform scan steps or a random ordering by interacting with the scan widget. Multi-dimensional scans are also supported by defining a nested dictionary for PulseSequence.scan_params.

The function run_initially contains any code, which can be run before the main scan. This code is executed asynchronously by Artiq during the "prepare" stage and while queued in the scheduler. This is generally where subsequences (which will be defined in a bit) are imported using the add_subsequence() method. This is also where subsequence() functions are set using the set_subsequence() method[1]. Functions which are set as subsequences() are run only at the beginning of every scan point and not for every shot of the experiment. For example, in the Ramsey experiment if one chooses to scan the wait time, then every choice of wait_time corresponds to a data point, but the experiment is repeated for a number of shots for each data point[2] in order to build up statistics. Any functions set as subsequences will only be run once for each choice of wait_time.

Finally, the function Ramsey() defines the actual pulse sequence that defines the main action of the experiment. It is important that the name of this function match one of the

---

[1]Note that there is a confusing double-use of the term subsequence here.

[2]set by the parametervault parameter StateReadout.repeat_each_measurement or by the PulseSequence class attribute self.N

dictionary keys for PulseSequence.scan_params.

An example subsequence, RabiExcitation, used by the Ramsey PulseSequence is shown in Section D. Subsequences contain most of the low-level Artiq code for performing tasks like setting DDS frequencies and turning on and off TTLs. Parametervault parameters can be loaded into subsequences as shown in the example code, but listing a parameter here will not cause it to show up in the experimental control window. It is important that a subsequence instance contains a method named subsequence(). This is the code that will actually be executed when the subsequence is run. Subsequences can also be combined together. For example, the StatePreparation subsequence in the example is actually a composite subsequence consisting of Doppler cooling, optical pumping and sideband cooling.

A desktop icon on the main experimental control computer is available for starting up the Artiq control software and GUI. This runs the script contained in ∼/launch_scripts/artiq_-startup.sh. The default plotter is a cheap knock-off of the RealSimpleGrapher ported to Python3 and called the RealComplicatedGrapher can be run with another desktop icon, which runs the script ∼/launch_scripts/rcg_startup.sh.

file/folder location	description
∼/artiq/artiq/dashboard	The code for all of the additional features added to the Artiq GUI is contained here.
∼/artiq/artq/frontend/artiq_dashboard.py	Code must be modified here to actually incorporate any new GUI features (defined in the dashboard directory) to the main Artiq GUI.
∼/artiq/artiq/applets/plot_pmt.py	The code for the PMT plot applet.
∼/artiq/artiq/applets/rcg/	A folder containing all of the code for the main grapher.
∼/artiq/artiq/applets/ rcg/RealComplicated-GrapherConfig.py	The basic configuration for the grapher can be set here (e.g. adding tabs or plots).
∼/artiq/artiq/applets/rcg/fitting/ fit_functions	New fit functions defined here will be automatically exposed to the user.
∼/artiq/artiq/master/worker_impl.py	A small modification to this file has been made so that the data from experiments is automatically saved in the /home/lattice/data directory in the appropriate format.
∼/artiq/artiq/.pulse_sequence/ pulse_sequence.py	The PulseSequence class is defined in this file.
∼/artiq-master/HardwareConfiguration.py	This is the configuration file used for specifying the details about the Artiq hardware. At a lower level, this information can instead be modified directly in the device_db.py file in the same directory.
∼/artiq-work/	For Artiq to know about a pulse sequence or subsequence it must be contained in this directory.
∼/launch_scripts	The code run when clicking on any one of the launch icons on the lattice control computer is defined here (e.g. for launching the Artiq GUI, LabRAD server, RealComplicatedGrapher, etc.)

Table D.1: Location of important Artiq control files and directories.

Ramsey pulse sequence example code

```python
from pulse_sequence import PulseSequence
from subsequences.rabi_excitation import RabiExcitation
from subsequences.state_preparation import StatePreparation
from artiq.experiment import *

class Ramsey(PulseSequence):
    PulseSequence.accessed_params = {
        "Ramsey.wait_time",
        "Ramsey.phase",
        "Ramsey.selection_sideband",
        "Ramsey.order",
        "Ramsey.channel_729",
        "Ramsey.detuning",
        "Ramsey.echo",
        "Rotation729L1.pi_time",
        "Rotation729L1.line_selection",
        "Rotation729L1.amplitude",
        "Rotation729L1.att",
        "Rotation729L2.pi_time",
        "Rotation729L2.line_selection",
        "Rotation729L2.amplitude",
        "Rotation729L2.att",
        "Rotation729G.pi_time",
        "Rotation729G.line_selection",
        "Rotation729G.amplitude",
        "Rotation729G.att",
        "RabiFlopping.detuning",
    }

    PulseSequence.scan_params = dict(
        Ramsey=[
            ("Ramsey", ("Ramsey.wait_time", 0*ms, 5*ms, 100, "ms")),
            ("Ramsey", ("Ramsey.phase", 0., 360., 20, "deg")),
            ("Ramsey", ("Rotation729G.amplitude", 0., 1., 10, "")),
        ])

    def run_initially(self):
        self.stateprep = self.add_subsequence(StatePreparation)
        self.rabi = self.add_subsequence(RabiExcitation)
        self.rabi.channel_729 = self.p.Ramsey.channel_729
        self.set_subsequence["Ramsey"] = self.set_subsequence_ramsey
        if self.p.Ramsey.channel_729 == "729L1":
            self.pi_time = self.p.Rotation729L1.pi_time
            self.line_selection = self.p.Rotation729L1.line_selection
            self.amplitude = self.p.Rotation729L1.amplitude
            self.att = self.p.Rotation729L1.att
        elif self.p.Ramsey.channel_729 == "729L2":
```

```
48                self.pi_time = self.p.Rotation729L2.pi_time
49                self.line_selection = self.p.Rotation729L2.line_selection
50                self.amplitude = self.p.Rotation729L2.amplitude
51                self.att = self.p.Rotation729L2.att
52            elif self.p.Ramsey.channel_729 == "729G":
53                self.pi_time = self.p.Rotation729G.pi_time
54                self.line_selection = self.p.Rotation729G.line_selection
55                self.amplitude = self.p.Rotation729G.amplitude
56                self.att = self.p.Rotation729G.att
57
58        @kernel
59        def set_subsequence_ramsey(self):
60            self.amplitude = self.get_variable_parameter("Rotation729G_amplitude")
61            self.rabi.duration = self.pi_time
62            self.rabi.amp_729 = self.amplitude
63            self.rabi.att_729 = self.att
64            self.rabi.freq_729 = self.calc_frequency(
65                        self.line_selection,
66                        detuning=self.Ramsey_detuning,
67                        sideband=self.Ramsey_selection_sideband,
68                        order=self.Ramsey_order,
69                        dds=self.Ramsey_channel_729
70                    )
71            self.wait_time = self.get_variable_parameter("Ramsey_wait_time")
72
73        @kernel
74        def Ramsey(self):
75            self.stateprep.run(self)
76            self.phase_ref_time = now_mu()
77            self.dds_729.set(
78                    self.carrier_frequency,
79                    amplitude=self.initial_carrier_amplitude,
80                    phase_mode=PHASE_MODE_TRACKING,
81                    ref_time_mu=self.phase_ref_time
82                )
83            self.dds_729_SP.set(
84                    self.sp_freq_729,
85                    amplitude=self.Excitation_729_single_pass_amplitude,
86                    phase_mode=PHASE_MODE_TRACKING,
87                    phase=0.,
88                    ref_time_mu=self.phase_ref_time
89                )
90            delay(5*us)
91            if not self.Ramsey_echo:
92                self.dds_729_SP.sw.on()
93                delay(self.NLQM_carrier_duration)
94                self.dds_729_SP.sw.off()
95            else:
96                self.rabi.duration = self.pi_time / 2
97                self.rabi.run(self)
```

```
98              delay(self.wait_time / 2)
99              self.rabi.duration = self.pi_time
100             self.rabi.run(self)
101             delay(self.wait_time / 2)
102             self.rabi.duration = self.pi_time / 2
103             if self.selected_scan_name == "Ramsey_phase":
104                 self.rabi.phase_729 = self.get_variable_parameter("Ramsey_phase")
105             self.rabi.run(self)
```

Rabi excitation subsequence example code

```python
1   from artiq.experiment import *
2   import numpy as np
3   from artiq.coredevice.ad9910 import PHASE_MODE_TRACKING, PHASE_MODE_CONTINUOUS
4
5   class RabiExcitation:
6       freq_729="Excitation_729.rabi_excitation_frequency"
7       amp_729="Excitation_729.rabi_excitation_amplitude"
8       att_729="Excitation_729.rabi_excitation_att"
9       phase_729="Excitation_729.rabi_excitation_phase"
10      channel_729="Excitation_729.channel_729"
11      duration="Excitation_729.rabi_excitation_duration"
12      line_selection="Excitation_729.line_selection"
13      sp_amp_729="Excitation_729.single_pass_amplitude"
14      sp_att_729="Excitation_729.single_pass_att"
15      use_bichro=False
16      phase_mode=PHASE_MODE_TRACKING
17      dp_phase_mode=PHASE_MODE_CONTINUOUS
18      phase_ref_time=np.int64(-1)
19      ramp_has_been_programmed= False  # always initialize to False;
20                                       # gets set to True inside setup_ramping
21
22      @kernel
23      def setup_ramping(self):
24          # This function programs the appropriate ramp into the DDS memory.
25          # If a PulseSequence wants to use ramping, call setup_ramping() inside
26          # its set_subsequence function.
27          # To disable ramping for a PulseSequence, the easiest way to do this is
28          # comment or remove the call to setup_ramping() in the set_subsequence function.
29          r = RabiExcitation
30          self.get_729_dds(r.channel_729)
31          self.prepare_pulse_with_amplitude_ramp(
32              pulse_duration=r.duration,
33              ramp_duration=25.0*us,
34              dds1_amp=r.amp_729)
35          r.ramp_has_been_programmed = True
```

```python
36
37    def subsequence(self):
38        r = RabiExcitation
39        self.get_729_dds(r.channel_729)
40        if r.ramp_has_been_programmed:
41            self.dds_729.set(r.freq_729,
42                             amplitude=0.,
43                             ref_time_mu=r.phase_ref_time)
44        else:
45            self.dds_729.set(r.freq_729,
46                             amplitude=r.amp_729,
47                             phase_mode=r.dp_phase_mode,
48                             ref_time_mu=r.phase_ref_time,
49                             )
50        self.dds_729.set_att(r.att_729)
51        sp_freq_729 = 80 * MHz + self.get_offset_frequency(r.channel_729)
52        if r.use_bichro:
53            self.single_pass = self.dds_729_SP_bichro
54        else:
55            self.single_pass = self.dds_729_SP
56        self.single_pass.set(sp_freq_729, amplitude=r.sp_amp_729, phase_mode=r.phase_mode,
57                        phase=r.phase_729 / 360., ref_time_mu=r.phase_ref_time)
58        self.single_pass.set_att(r.sp_att_729)
59        delay(5*us)
60        if r.ramp_has_been_programmed:
61            self.dds_729_SP.sw.on()
62            self.execute_pulse_with_amplitude_ramp(
63                dds1_att=r.att_729,
64                dds1_freq=r.freq_729)
65            self.dds_729_SP.sw.off()
66        else:
67            with parallel:
68                self.dds_729.sw.on()
69                self.single_pass.sw.on()
70            delay(r.duration)
71            with parallel:
72                self.dds_729.sw.off()
73                self.single_pass.sw.off()
```
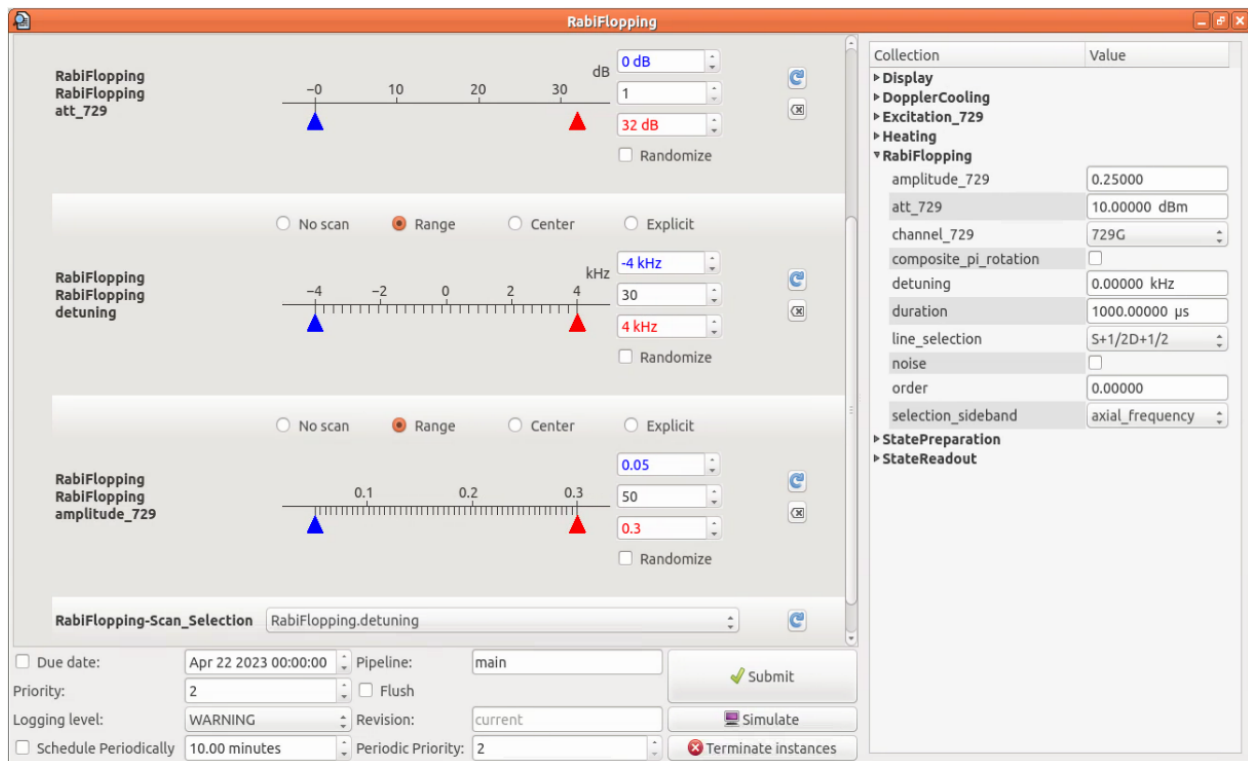
Figure D.1: Example of an Artiq generated experimental control window.